

Raman Spectroelectrochemical Investigations of Immobilized Redox Proteins

vorgelegt von
Diplom-Physikerin
Jana Grochol
aus Hořovice

Von der Fakultät II - Mathematik und Naturwissenschaften
der Technischen Universität Berlin
zur Erlangung des akademischen Grades
Doktor der Naturwissenschaften
- Dr. rer. nat -
genehmigte Dissertation

Promotionsausschuss:

Vorsitzender: Prof. Dr. Thomas Friedrich
Berichter: Prof. Dr. Daniel H. Murgida
Berichter: Prof. Dr. Peter Hildebrandt

Tag der wissenschaftlichen Aussprache: 29. März 2007

Berlin 2007
D 83

Abstract

Redox proteins adsorbed on electrodes have gained increasing attention of researchers in both fundamental and applied science. Surface-enhanced resonance Raman (SERR) spectroelectrochemistry is a particularly suitable technique for studying heterogeneous electron transfer reactions as it selectively probes the redox sites of the adsorbed proteins. SERR spectroscopy combines the advantages of the surface and resonance enhancement by exciting a heme protein immobilized on rough silver electrodes in the Soret absorption band region. Protein immobilization methods involve coating the electrodes with biocompatible films in order to prevent protein denaturation. This work focuses on the elucidation of heterogeneous electron transfer mechanism and dynamics of the soluble cytochrome *c* (Cyt *c*) and the membrane-bound cytochrome *c* oxidase (CcO) attached to electrodes modified with different functional groups.

First, Cyt *c* coordinatively attached to self-assembled monolayers of pyridine-terminated alkanethiols on electrodes was employed as a model system to study basic aspects of heterogeneous electron transfer. Electron transfer at short spacer lengths was monitored by time-resolved SERR spectroscopy. The electron transfer rate constant increased with increasing driving force indicating a change of mechanism from a nonadiabatic, tunneling controlled reaction at long distances to the electrode, to an increasingly solvent/protein friction controlled mechanism at shorter spacers.

Second, polyelectrolyte-Cyt *c* multilayers were investigated, which are of interest in the fabrication of biosensors. An anionic polyelectrolyte, the poly(aniline sulfonic acid) (PASA), was used to intercalate the cationic redox protein. The PASA-Cyt *c* multilayer assemblies were, however, not stable on rough Ag electrodes coated with a mixed carboxyl/hydroxyl-terminated film resulting in a one PASA-Cyt *c* layer system. As indicated by SERR measurements, Cyt *c* within the PASA layer retains its native properties. Redox potentials and standard rate constants of the immobilized Cyt *c* determined by SERR spectroelectrochemistry display an excellent agreement with the values obtained by cyclic voltammetry. Stationary and time-resolved SERR experiments reveal reversible spectral changes of PASA that provide evidence for electron exchange between Cyt *c* and PASA pointing to a tight coupling of the two species in the multilayer assemblies.

Finally, a novel immobilization technique was employed to attach CcO to an electrode and subsequently reconstitute the lipid environment. The immobilization procedure is based on the affinity of a metal-chelating surface

modification to a histidine-tag, engineered to different sides of the enzyme, and hence is applicable to a large variety of (membrane) proteins. Upon avoiding the very facile photoreduction, SERR spectra of the immobilized CcO reveal preservation of the native structures of the heme *a* and heme *a*₃ sites. The electron transfer reaction was independent of enzyme orientation and the applied driving force suggesting that it involves multi-step electron tunneling or hopping over a distance of ca. 50 Å. Moreover, electrochemical reduction was restricted to heme *a* pointing to a perturbation of the native network of cooperativities between electron transfer and proton translocation in the immobilized enzyme.

Zusammenfassung

Das Interesse an auf Elektroden immobilisierten Redoxproteinen ist in den letzten Jahren stark gestiegen. Die oberflächenverstärkte Resonanz-Raman-(SERR) Spektroelektrochemie eignet sich hervorragend zum Studium des heterogenen Elektronentransfers, da sie selektiv das Schwingungsspektrum der Redoxzentren der immobilisierten Spezies abfragt. SERR Spektroskopie kombiniert die Vorteile der Oberflächen- und Resonanz-Verstärkung, indem Hämproteine auf rauen Silberelektroden adsorbiert und in der Soret-Absorptionsbande angeregt werden. Eine biokompatible Beschichtung der rauen Elektroden verhindert die Denaturierung des Proteins. Die vorliegende Arbeit analysiert die Mechanismen und die Dynamik des heterogenen Elektronentransfers des löslichen Cytochrom *c* (Cyt *c*) und der membrangebundenen Cytochrom *c* Oxidase (CcO).

Zuerst wurde Cyt *c* an Pyridin-terminierte selbstorganisierte Monoschichten koordinativ gebunden und als Modellsystem untersucht. Elektronentransfer auf dünnen Monoschichten wurde mit zeitaufgelöster SERR Spektroskopie verfolgt. Der Anstieg der Elektronentransferrate mit zunehmender treibender Kraft wies auf eine Änderung des Mechanismus vom nonadiabatischen in großer Entfernung von der Elektrode zum verstärkt von Lösung/Protein-Dämpfung kontrollierten Prozess bei kurzen Abständen hin.

Weiterhin wurden Polyelektrolyt-Cyt *c* Multilagen, die potenziell als Biosensoren angewendet werden können, untersucht. Ein anionischer Polyelektrolyt wurde alternierend mit dem kationischen Protein auf eine beschichtete Elektrode adsorbiert. Die Multilagen waren allerdings an Silberelektroden nicht stabil, so dass nur eine PASA-Cyt *c* Lage mit SERR Spektroelektrochemie und Zyklovoltammetrie erforscht werden konnte. Beide Methoden ergaben eine hervorragende Übereinstimmung der Redoxpotenziale und formalen Geschwindigkeitskonstanten. SERR Spektren wiesen darauf hin, dass Cyt *c* innerhalb des PASA-Systems im nativen Zustand vorliegt. Stationäre und zeitaufgelöste SERR Messungen zeigten reversible spektrale Änderungen des Polyelektrolyten, welche auf einen Elektronentransfer zwischen PASA und Cyt *c* hindeuten.

Schließlich wurde eine neuartige Immobilisierungsstrategie eingesetzt, bei der man die membrangebundene CcO an die Elektrode adsorbiert und anschließend eine Lipid-Umgebung wiederherstellt. Die Immobilisierung basiert auf der Affinität einer chelatbildenden Elektrodenbeschichtung zum Histidin-Tag, der an zwei gegenüberliegenden C-Termini des Enzyms angebracht wurde. Daher kann diese Methode auf viele (Membran)Proteine ausgeweitet

werden. Die schnell auftretende Photoreduktion im immobilisierten Zustand konnte erst mit einem neuen experimentellen Aufbau verhindert werden. SERR Spektren zeigten eine native Struktur der Häm *a* und Häm *a*₃ Kofaktoren. Die Elektronentransfer Dynamik war unabhängig von der Orientierung des Enzyms und der treibenden Kraft, was auf einen Hopping-Mechanismus über 50 Å hinweist. Die auf Häm *a* begrenzte elektrochemische Reduktion läßt eine Störung der nativen Kooperativität zwischen Elektronentransfer und Protonentranslokation vermuten, die möglicherweise durch das elektrische Feld induziert wird.

Contents

Abstract	iii
Zusammenfassung	v
Contents	ix
List of abbreviations	xiii
I Introduction	1
II Theoretical background	7
1 Raman spectroscopy	9
1.1 Classical description of the Raman effect	9
1.2 Resonance Raman spectroscopy	11
1.3 Surface-enhanced Raman spectroscopy	14
2 Investigated proteins	17
2.1 Cytochrome <i>c</i>	17
2.2 Cytochrome <i>c</i> oxidase	18
2.3 RR spectroscopy of heme proteins	20
2.3.1 Cytochrome <i>c</i>	23
2.3.2 Cytochrome <i>c</i> oxidase	24
2.4 SERR spectroscopy of heme proteins	26
3 Electrochemical interfaces	27
3.1 Electrode-solution interface	27
3.2 Self-assembled monolayers	28
3.3 Interfacial potential distribution	30

4	Electron transfer theory	33
4.1	General considerations	33
4.2	Homogeneous electron transfer	34
4.2.1	Classical Marcus theory	34
4.2.2	Quantum mechanical treatment	36
4.3	Heterogeneous electron transfer	37
4.4	Effect of friction on electron transfer	39
III	Experimental methods and data treatment	43
5	Electrochemistry	45
5.1	Electrochemical cells	45
5.1.1	Ring electrode system	45
5.1.2	Disk electrode system	47
5.2	Cyclic voltammetry	48
6	Electrode preparation	49
6.1	Preparation of the SER-active surface	49
6.2	Immobilization strategies	49
6.2.1	Coordinative binding of Cyt <i>c</i>	50
6.2.2	Cyt <i>c</i> immobilized within a polyelectrolyte layer	50
6.2.3	His-tag immobilization of CcO	52
7	RR and SERR spectroscopy	55
7.1	Experimental setup	55
7.2	Stationary and TR-SERR spectroscopy	57
8	Spectra treatment	59
8.1	CCD image correction	59
8.2	Background subtraction	63
8.3	Component analysis	66
IV	Results and discussion	67
9	Direct wiring of cytochrome <i>c</i>	69
9.1	Introduction	69
9.2	Distance and temperature dependence	73
9.3	Overpotential dependence	74
9.4	Discussion	81
9.5	Summary	86

10 Cytochrome <i>c</i>-polyelectrolyte	87
10.1 Introduction	87
10.2 Electrostatically adsorbed Cyt <i>c</i>	88
10.2.1 Redox equilibrium	88
10.2.2 Electron transfer dynamics	92
10.3 Multilayer assemblies	96
10.3.1 PASA-Cyt <i>c</i> multilayers	96
10.3.2 Apo containing multilayers	101
10.4 PASA potential-dependent changes	108
10.5 Electron transfer dynamics	111
10.6 Summary	115
11 Cytochrome <i>c</i> oxidase	117
11.1 Introduction	117
11.2 Formation of the Ni-NTA SAM monitored by SEIRA	118
11.3 Photoreduction	120
11.4 Different modes of CcO immobilization	125
11.5 Redox equilibrium and reduction dynamics	125
11.5.1 Anaerobic conditions	126
11.5.2 Aerobic conditions	130
11.5.3 CN inhibited CcO	131
11.6 Discussion	135
11.6.1 Long distance electron transfer	135
11.6.2 Selective reduction of heme <i>a</i>	136
11.7 Summary	138
V Conclusions and Outlook	141
Bibliography	149
Addendum	175
Aufstellung der wissenschaftlichen Veröffentlichungen	175
Selbständigkeitserklärung	177
Acknowledgement	179
Lebenslauf	181

List of abbreviations

5cHS	five-coordinated high spin
6cHS	six-coordinated high spin
6cLS	six-coordinate low spin
a.u.	arbitrary units
Apo	apocytochrome <i>c</i>
CCD	charge-coupled device
CE	counter electrode
CcO	cytochrome <i>c</i> oxidase
CV	cyclic voltammogram
Cyt <i>c</i>	cytochrome <i>c</i>
DDM	<i>n</i> -dodecyl- β -D-maltoside
DOS	density of states
i.e.	id est (that is)
HS	high spin
LS	low spin
MU	11-mercaptoundecanol
MUA	11-mercaptoundecanoic acid
NA	numerical aperture
NHE	normal hydrogen electrode
NTA	nitrilo-triacetic acid
PASA	poly(aniline sulfonic acid)
QCM	quartz crystal microbalance
RE	reference electrode
RR	resonance Raman
SAM	self-assembled monolayer
SEIRA	surface-enhanced infrared absorption
SER	surface-enhanced Raman
SERR	surface-enhanced resonance Raman
SNR	signal-to-noise ratio
SVD	singular value decomposition
UV-Vis	ultraviolet-visible
WE	working electrode

Part I

Introduction

Overview

Inter- and intraprotein electron transfer reactions play an essential role in photosynthesis, respiration and metabolic pathways. In these reactions, electrons with a relatively low reduction potential arise from the oxidation of a substrate and are transferred through an electron transfer chain via a series of well-controlled steps. The electrochemical energy is partially stored as a transmembrane proton gradient. Electron transfer chains basically involve two types of proteins; relatively small soluble electron carriers shuttle electrons between large membrane-bound complexes. Even though integral membrane proteins are of key importance in the physiology of living cells, they still remain experimentally challenging due to their complex structure and rather low stability when isolated.

Biological electron transfer reactions occur between two reactants fixed in position and may span distances greater than 10 Å. Interprotein electron transfer might require specific binding of proteins, protein rearrangement, chemical modifications. Nature seems to have optimized distance, reaction free energy and reorganization energy in electron transfer proteins in order to promote physiologically relevant electron transfer and to prevent competing unwanted processes.¹ Rather than in a single step, long-range electron transfer often proceeds over a series of intermediates to achieve efficient overall rates. Indeed, all characterized transmembrane redox proteins, that are responsible for a successful electron transfer across the 35 Å span of biological membranes, contain at least three cofactors. Therefore, transmembrane electron transfer reactions can be fast even at low driving forces.

A major factor that controls biological electron transfer reactions is the reorganization energy, many investigations have thus aimed to its determination for different proteins. However, direct experiments to obtain the reorganization energy values and to estimate the protein contribution are far from trivial. Varying the other two crucial parameters that control the reaction, i.e. the distance and the driving force, proves difficult for reactions in solution.

This limitation is overcome in heterogeneous electron transfer reactions

that involve a protein and an electrode. The driving force is defined by the potential applied to the electrode and the distance can be varied in a large range thanks to recent development of methods to control and manipulate surface chemistry.² Electrodes coated with the so-called self-assembled monolayers provide a biocompatible electrochemical interface to which redox proteins can be adsorbed upon preservation of the native structure. Indeed, physiologically relevant reactions of redox proteins take place at or in membranes, where they experience large electric field strengths induced by the potential drop through the lipid bilayer.³ Modified electrodes represent therefore a suitable model system since they can mimic the membrane/solution interface.

Investigations of heterogeneous electron transfer processes may contribute to a better understanding of biological redox reactions. Thanks to incessant technological development, the performance of electrochemical methods has been largely improved in the recent years and bioelectrochemistry has attracted important research efforts in both fundamental⁴ and applied science.⁵ Nowadays, single-protein voltammetry has become the new target of electrochemists^{6,7} and electron transfer at nanoelectrodes has been reported recently.⁸ However, electrochemical methods do not provide structural information about the redox species and about possible processes at the interface that do not involve transfer of charge. Surface-enhanced vibrational spectroscopic methods have been shown to represent a powerful alternative as they enable to monitor structural changes of immobilized redox proteins.^{9,10,11}

Surface-enhanced resonance Raman (SERR) spectroscopy of redox proteins has also profited from the advent of self-assembled monolayers (SAM). The exaltation following the first successful application of resonance Raman spectroscopy combined with the surface enhancement effect to a redox protein in 1980¹² was later stopped by the observation of adsorption-induced denaturation of the immobilized proteins. Today, SERR spectroscopy of redox proteins attached to silver electrodes modified with biocompatible coatings represents a well established experimental technique. Upon proper choice of excitation wavelength, SERR spectroscopy selectively probes the redox site only of the adsorbed protein. The so-called SERR spectroelectrochemistry can be performed in the stationary and, combined with the potential-jump technique, in the time-resolved mode. Thereby it allows to monitor equilibria and dynamics of potential-dependent interfacial processes.

Objectives

The aim of the present work is to contribute in several ways to SERR spectroelectrochemical investigations of interfacial processes of redox proteins immobilized on electrodes. The addressed topics concern electron transfer mechanism, application of modified electrodes in biosensing and utilization of novel immobilization strategies. Experiments were performed on two very different proteins – the soluble electron carrier cytochrome *c* (Cyt *c*) and the membrane-bound proton-pump cytochrome *c* oxidase (CcO); immobilization of these heme proteins included three different strategies.

The thesis is divided as follows. Part II introduces relevant theoretical concepts, Part III describes the experimental background, Part IV is dedicated to the results and discussions and Part V offers a general conclusion. Each investigated system is thoroughly introduced in the corresponding chapter of Part IV. Here, only a short overview is be given.

First, basic aspects of heterogeneous electron transfer were examined for Cyt *c* coordinatively attached to self-assembled monolayers of pyridine-terminated alkanethiols on electrodes. Electron transfer at thin films was monitored by time-resolved SERR spectroelectrochemistry allowing for a detailed discussion of its mechanism. Second a polyelectrolyte-Cyt *c* layer system was investigated by stationary and time-resolved SERR spectroelectrochemistry raising questions about possible implication of the polyelectrolyte in long-range electron transfer. Finally, a novel immobilization technique was employed to attach CcO to electrodes and subsequently embed it in a lipid environment. This part required designing new experimental equipment.

Part II

Theoretical background

Chapter 1

Raman spectroscopy

Vibrational spectroscopy methods, to which Raman spectroscopy belongs together with the complementary infrared (IR) technique, are important probes of molecular structure and dynamics. They are being employed to measure molecular vibrational frequencies ($10^{-13} - 10^{-14}$ Hz), which fall in the infrared region of the electromagnetic spectrum. Infrared spectroscopy is a direct method for measuring transitions between vibrational levels induced by absorption of light in the infrared region. Raman spectroscopy consists in studying inelastic scattering of the incident light on vibrational motions of molecules or elements of a crystal lattice. Though the Raman effect was theoretically predicted in 1923 by Smekal,¹³ it was experimentally discovered only five years later by Raman¹⁴ after whom the effect was named and who was awarded the Nobel Prize in Physics in 1930.

1.1 Classical description of the Raman effect

If incident light of frequency ν_0 passes through a sample, a small fraction of the radiation is scattered in all directions. Most of the scattered light emerges without change in frequency; this is elastic or Rayleigh scattering. However, a small part of the incident photons lose or gain energy in inelastic collisions with the molecules. A net transfer of quantized energy ($\Delta E = h\nu_k$) takes place and some scattered light emerges at modified frequencies ($\nu_0 \pm \nu_k$). The changes of frequency correspond to transitions between vibrational levels of the molecule.

A Raman spectrum consists of two groups of bands situated symmetrically around the significantly more intense Rayleigh scattering band. The region of lower frequencies ($\nu_0 - \nu_k$) correspond to the so-called Stokes scattering while that at higher frequencies ($\nu_0 + \nu_k$) is referred to as anti-Stokes scatter-

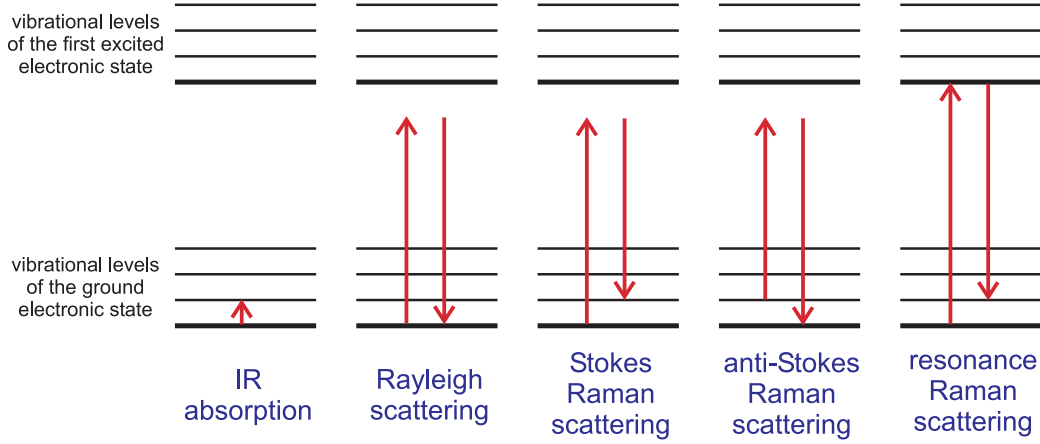


Figure 1.1: Schematic representation of transitions associated with IR absorption and Raman scattering.

ing. As illustrated in Figure 1.1 anti-Stokes scattering induces a transition of the molecules from an excited vibrational state to the ground state and has therefore a lower intensity than the Stokes scattering due to the Boltzmann distribution of states. The frequency difference between a particular Raman band and the incident radiation corresponds to the frequency of a given vibration. It is termed Raman or wavenumber shift ($\Delta\nu = |\nu_k|$) and expressed in wavenumbers (cm^{-1}).

A simple theoretical model of Raman scattering is based on a classical description of the interaction of the laser beam with the molecule. The fluctuating electric field \mathbf{E} of the laser (with a frequency ν_0) induces in the molecule an electric dipole moment \mathbf{P} . The magnitude and direction of \mathbf{P} depend both on the perturbing electric field \mathbf{E} and on the deformability of the electron cloud which can be described by the polarizability tensor α of a molecule

$$\mathbf{P} = \alpha \mathbf{E}. \quad (1.1)$$

The polarizability tensor is represented by a polarizability ellipsoid and has nine elements ($\alpha_{\rho\sigma}$, $\rho, \sigma \in x, y, z$). The intensity of a particular Raman band, that originates in a transition from state $|i\rangle$ to state $|f\rangle$, is proportional to $|\alpha_{if}|^2$, the square of the vibrational transition moment

$$[\alpha]_{if} = \langle f | \alpha | i \rangle. \quad (1.2)$$

Expanding α in a Taylor series for small deviations from the normal coordinate Q_k results in the following nonvanishing terms

$$\alpha_0 \langle f | i \rangle \sim \alpha_0 \delta(f, i) \quad (1.3)$$

which corresponds to the dominant Rayleigh scattering with $f = i$, $\Delta\nu = 0$; and

$$\left(\frac{\partial\alpha}{\partial Q_k}\right)_0 \langle f|Q_k|i\rangle \sim \left(\frac{\partial\alpha}{\partial Q_k}\right)_0 \delta(f, i \pm 1) \quad (1.4)$$

which gives the weaker Raman scattering with $f = i \pm 1$ and $\Delta\nu = \pm\nu_k$ if $\left(\frac{\partial\alpha}{\partial Q_k}\right)_0 \neq 0$. Therefore only those vibrations, which induce a change in molecular polarizability, are Raman active. It can be shown in a similar way, that infrared absorption requires a change in the dipole moment of a molecule. As a consequence of the different selection rules, Raman and IR spectra provide complementary information about the vibrational states of a molecule.

The polarization of the scattered light may bring some additional information about the molecule. The depolarization ratio of a Raman band is defined as

$$\rho = \frac{I_{\perp}}{I_{\parallel}}, \quad (1.5)$$

where I_{\perp} and I_{\parallel} denote the intensities of the scattered light with polarizations perpendicular and parallel to the plane of polarization of the incident radiation, respectively. The line is classified as depolarized if $\rho = 0.75$ and as polarized if $\rho < 0.75$. Only totally symmetrical vibrations give rise to polarized bands. The polarization can be anomalous ($\rho > 0.75$) in special cases involving the resonance Raman effect.

The classical description of the Raman effect predicts well the selection rules and the positions of Raman lines but fails to explain the intensity difference between the Stokes and anti-Stokes bands. Quantum description of the molecular system is required to evaluate the Raman scattering intensity correctly and, above all, to account for the resonance Raman effect.

1.2 Resonance Raman spectroscopy

The quantum mechanical description of the Raman effect is derived from the second-order perturbation theory and was developed by Albrecht.^{15,16,17} The intensity of Raman scattering was found to be described by a ν_4 law. Transition of a molecule from an initial vibrational state $|i\rangle$ of energy E_i to a final vibrational state $|f\rangle$ may give rise to a Raman band of frequency ν_{if} and intensity

$$I_{if} \sim (\nu_0 \pm \nu_{if})^4 I_0 \exp\left(-\frac{E_i}{k_B T}\right) \sum_{\rho, \sigma=x,y,z} |[\alpha_{\rho\sigma}]_{if}|^2. \quad (1.6)$$

Here, I_0 is the intensity of the exciting radiation and $[\alpha_{\rho\sigma}]_{if}$ denotes the matrix elements of the polarizability transition moment.

The intensity of Raman scattering depends thus strongly on the excitation frequency. However, when the frequency of the incident radiation is close to (preresonance) or equal to (resonance) the frequency of an allowed electronic transition of a molecule (see Figure 1.1), the intensities of certain Raman bands are greatly enhanced above their off-resonance values. Only those bands, which are induced by vibrational transitions that couple with the allowed electronic transition, intensify because the polarizability is enhanced via the electronic transition. Information about electronic transitions in a molecule can be gained from UV-Vis (ultraviolet-visible) spectroscopy.

The matrix elements of the polarizability transition moment are given by the modified Kramers-Heisenberg dispersion equation

$$[\alpha_{\rho\sigma}]_{if} = \frac{1}{h} \sum_{r \neq i, f} \left(\frac{\langle f | \hat{\mathbf{D}}_\rho | r \rangle \langle r | \hat{\mathbf{D}}_\sigma | i \rangle}{\nu_r - \nu_i - \nu_0} + \frac{\langle f | \hat{\mathbf{D}}_\sigma | r \rangle \langle r | \hat{\mathbf{D}}_\rho | i \rangle}{\nu_r - \nu_f + \nu_0} \right), \quad (1.7)$$

where $|r\rangle$ represents a virtual intermediate state, h is the Planck's constant, $h\nu_i$, $h\nu_f$ and $h\nu_r$ denote the energies of the initial, final and intermediate state, respectively. $\hat{\mathbf{D}}$ is the dipole moment operator, $\langle f | \hat{\mathbf{D}}_\rho | r \rangle$ and $\langle r | \hat{\mathbf{D}}_\sigma | i \rangle$ describe the dipole transition moments along the ρ and σ direction. The summation runs over intermediate excited states $|r\rangle$, each state being weighted by its energetic nearness to the resonance with the incident light.

The denominators in eq (1.7) are large far from resonance ($\nu_r - \nu_i \gg \nu_0$); the number of intermediate states contributing to the polarizability is large and the magnitude of $[\alpha_{\rho\sigma}]_{if}$ is independent of ν_0 . The situation changes under conditions of resonance with a particular electronic state $|e\rangle$ ($\nu_r - \nu_i = \nu_e \approx \nu_0$) and eq (1.7) is no longer valid. A correction term has to be introduced to the denominators of eq (1.7), i.e. the damping factor Γ_r which reflects the finite natural lifetime of the intermediate state

$$[\alpha_{\rho\sigma}]_{if} = \frac{1}{h} \sum_{r=e} \left(\frac{\langle f | \hat{\mathbf{D}}_\rho | r \rangle \langle r | \hat{\mathbf{D}}_\sigma | i \rangle}{\nu_r - \nu_i - \nu_0 + i\Gamma_r} + \frac{\langle f | \hat{\mathbf{D}}_\sigma | r \rangle \langle r | \hat{\mathbf{D}}_\rho | i \rangle}{\nu_r - \nu_f + \nu_0 + i\Gamma_r} \right). \quad (1.8)$$

The excited state prevails now in the summation. The first term in eq (1.8) becomes dominant (resonant term) and the scattered intensity is expected to increase drastically when the excitation frequency is tuned to the frequency of the electronic transition ν_{ie} . According to the Born-Oppenheimer approximation, electronic and vibrational wave functions can be separated since nuclei move much slower than electrons

$$|i\rangle = |g\rangle|m_i\rangle \quad |f\rangle = |g\rangle|m_f\rangle \quad |e\rangle = |e\rangle|n\rangle, \quad (1.9)$$

in which $|g\rangle$ and $|e\rangle$ stand for ground and excited electronic state; $|m_i\rangle$, $|m_f\rangle$ and $|n\rangle$ denote the vibrational wave functions of the initial, final and intermediate state, respectively. Neglecting the second (nonresonant) term, eq (1.8) becomes

$$[\alpha_{\rho\sigma}]_{if} = \frac{1}{h} \sum_n \frac{\langle m_f | \mu_\rho | n \rangle \langle n | \mu_\sigma | m_i \rangle}{\nu_n - \nu_i - \nu_0 + i\Gamma_n}, \quad (1.10)$$

in which $\mu_\rho = \langle g | \hat{\mathbf{D}}_\rho | e \rangle$ and $\mu_\sigma = \langle e | \hat{\mathbf{D}}_\sigma | g \rangle$ are the pure electronic transition dipole moments at a given nuclear configuration along the ρ and σ directions and the summation runs over vibrational levels n of the electronically excited state. The electronic transition moments depend only weakly on the normal coordinate Q_k and can be expanded in a Taylor series

$$\mu = \mu_0 + \sum_k \left(\frac{\partial \mu}{\partial Q_k} \right)_0 Q_k + \dots \quad (1.11)$$

Substituting eq (1.11) in eq (1.10) results in an expression for $[\alpha_{\rho\sigma}]_{if}$ with many terms, of which the first three terms, called A-, B- and C-term are the dominant mechanisms in resonance Raman scattering

$$[\alpha_{\rho\sigma}]_{if} = A + B + C + \dots \quad (1.12)$$

with

$$A = \frac{1}{h} \mu_{0\rho} \mu_{0\sigma} \sum_n \frac{\langle m_f | n \rangle \langle n | m_i \rangle}{\nu_n - \nu_i - \nu_0 + i\Gamma_n} \quad (1.13)$$

$$B = \frac{1}{h} \left[\mu_{0\rho} \left(\frac{\partial \mu_\sigma}{\partial Q_k} \right)_0 \sum_n \frac{\langle m_f | n \rangle \langle n | Q_k | m_i \rangle}{\nu_n - \nu_i - \nu_0 + i\Gamma_n} + \left(\frac{\partial \mu_\rho}{\partial Q_k} \right)_0 \mu_{0\sigma} \sum_n \frac{\langle m_f | Q_k | n \rangle \langle n | m_i \rangle}{\nu_n - \nu_i - \nu_0 + i\Gamma_n} \right] \quad (1.14)$$

$$C = \frac{1}{h} \left(\frac{\partial \mu_\sigma}{\partial Q_k} \right)_0 \left(\frac{\partial \mu_\rho}{\partial Q_k} \right)_0 \sum_n \frac{\langle m_f | Q_k | n \rangle \langle n | Q_k | m_i \rangle}{\nu_n - \nu_i - \nu_0 + i\Gamma_n}. \quad (1.15)$$

A-term scattering arises from the Franck-Condon overlap integrals $\langle m_f | n \rangle$ and $\langle n | m_i \rangle$ if $\mu_0 \neq 0$. Consequently, the A-term is most pronounced for strongly allowed electronic transitions that cause a shift of the potential energy surface along the corresponding coordinate as for example electric dipole allowed $\sigma\text{-}\sigma^*$, $\pi\text{-}\pi^*$ and charge transfer transitions. The nonorthogonality of the vibrational wave functions in the ground and excited state is

much stronger for totally symmetric than for non-totally symmetric modes yielding significantly higher resonance Raman intensities for the former. The B-term in eq (1.12) arises from the Herzberg-Teller vibronic coupling between different excited states induced by a vibrational excitation. The B-term scattering is most pronounced when the incident frequency is tuned to a weakly allowed electronic transition that is vibronically mixed with a nearby strong one. It is also a prime cause of resonance Raman activity of non-totally symmetric modes. The C-term gives rise to first overtones and combination modes.

1.3 Surface-enhanced Raman spectroscopy

Classical Raman scattering is not a very sensitive spectroscopic technique due to its low quantum yield and required sample concentrations in the order of mM. The resonance Raman effect lowers the concentration demands down to the μM range. In 1974, Fleischmann *et al.* observed intense Raman scattering from pyridine adsorbed on a roughened silver electrode.¹⁸ In 1977, other groups recognized independently that the large intensities observed could not be explained simply by the increase of sample concentration at the roughened surface and suggested that an enhancement of the scattered intensity occurred in the adsorbed state.^{19,20} The intensity of the surface-enhanced Raman (SER) scattering was found to be typically 10^6 -fold over the normal Raman scattering. The discovery of the surface enhancement effect triggered a vivid experimental and theoretical research work.²¹

Since its discovery, SER effect has been observed for a large number of molecules adsorbed on the surface of several metals (silver, gold and copper have been most widely used) in a variety of morphologies and physical environments. The largest enhancements occur for surfaces which are rough on the nanoscale (10-100 nm). The roughness can be obtained by electrochemical roughening, evaporation or sputtering of metal films in vacuum, preparation of colloids, formation of nanoparticle arrays.²²

SER spectroscopy differs in a number of ways from classical Raman scattering. Band frequency shifts can be observed in SER spectra, the relative band intensities change and vary with excitation wavelength and potential in electrochemical systems. New bands tend to appear in the spectra, which are forbidden or weak in the bulk sample or may result from a chemical modification of the adsorbed molecule. Excitation profiles differ from the ν^4 dependence of the nonresonant scattering and depend upon electrode potential in electrochemical experiments. SER bands tend to be completely depolarized. Fluorescence quenching was observed for dye molecules. The

enhancement may be remarkably long ranged.²²

Many theories have emerged to account for the experimental observations. They may be classified into two groups: theories involving effects of the surface on the electromagnetic field (electromagnetic theories) and those involving a chemical interaction between the molecule and the surface resulting in a modification of the molecular electronic structure.

Within the electromagnetic theories is the localized particle plasmon model supported by the largest experimental evidence. A surface plasmon is a collective excitation of the electron gas in a conductor confined to the near surface region. The electromagnetic field of the light at the surface can be greatly enhanced under conditions of surface plasmon excitation. The electromagnetic SER enhancement mechanism consists in an amplification of both the incident laser field and the scattered Raman field through their interaction with the surface. Electromagnetic enhancement factors have been calculated for multiple model systems including isolated and interacting spheres and ellipsoids, rough surfaces treated as collections of hemispherical bumps or fractal surfaces.²³

The simplest treatment of the electromagnetic enhancement involves the electrostatic approximation. The field induced at the surface of a spherical particle is related to the applied laser field E_0

$$E_{induced} = \frac{\epsilon(\omega) - \epsilon_s}{\epsilon(\omega) + 2\epsilon_s} E_0, \quad (1.16)$$

in which $\epsilon(\omega)$ denotes the complex permittivity of the metal and ϵ_s is the dielectric constant of the surrounding medium. Expression (1.16) enters into resonance if $\text{Re}(\epsilon) = -2\epsilon_s$ and $E_{induced}$ is greatly enhanced. This simple model, which can be qualitatively applied to a variety of surface morphologies, accounts for most of the experimental observations. The prevalence of coinage and alkali metals in experimental studies can be ascribed to the fact, that the resonance condition for these metals is fulfilled in the visible spectral region. The shape of metal particles also plays an important role in the surface enhancement. The surface plasmon oscillations can be effectively tuned by changing the morphology of the particles to match the excitation wavelength.²⁴

Chemical enhancement operates independently of the electromagnetic mechanism. It requires a close interaction of the adsorbed molecule with the metal surface resulting in the mixing of electronic states and inducing changes in the polarizability of the molecule-metal system. Three types of interaction have been described.²⁵ First, chemisorption of the molecule onto the surface and the resulting overlap of molecule and metal orbitals may lead to surface-induced resonance Raman enhancement. Second, surface-induced

hyperpolarizability can be induced by the donation of electron density via a donor-acceptor complex. Finally, an increase in polarizability may be triggered by an excited state charge transfer interaction. Unlike electromagnetic enhancement mechanism, the chemical enhancement mostly involves a modification of the investigated molecule and is limited to the scatterers directly adsorbed on the metal surface.

Chapter 2

Investigated proteins

The present work focuses on the investigation of spectroelectrochemical properties of redox proteins. The two examined metalloproteins, namely cytochrome *c* and cytochrome *c* oxidase, constitute essential components of the electron transport chain in aerobic respiration.

2.1 Cytochrome *c*

Cytochrome *c* (Cyt *c*) is a soluble monoheme protein with a relatively small size of about 12.5 kDa, loosely associated with the inner membrane of the mitochondrion. Cyt *c* transfers electrons from cytochrome *c* reductase to cytochrome *c* oxidase. Furthermore, Cyt *c* plays an important role in programmed cell death. Release of Cyt *c* from mitochondria followed by partial unfolding of the protein was found to constitute a key step in apoptosis.²⁶

As a remarkably stable protein involved in fundamental biological processes, Cyt *c* has become the subject of intensive research efforts during the last three decades. Especially horse heart Cyt *c* has been the target of abundant investigations by various experimental techniques including X-ray crystallography, NMR, EPR, electrochemistry or vibrational spectroscopy. An important library of experimental data is readily available for comparison making horse heart Cyt *c* an ideal model protein with very well described structural and dynamic properties.^{27,28}

Crystal structure of oxidized horse heart Cyt *c* was solved at a resolution of 1.94 Å (Figure 2.1*).²⁹ The protein consists of 104 amino acid residues in a single polypeptide chain folded into a compact, nearly spherical conformation (ca. 35 Å in diameter). The heme moiety is covalently attached to the

*All protein figures in this work were prepared with the help of the Visual Molecular Dynamics (VMD) program.³⁰

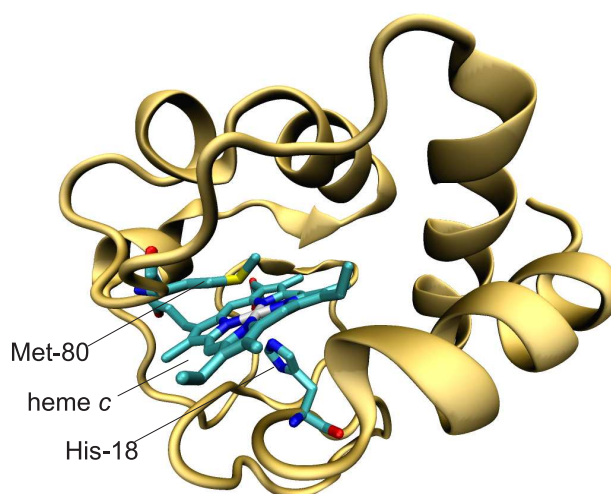


Figure 2.1: Structure of oxidized horse heart Cyt *c* (Protein Data Bank ID code 1HRC).²⁹ The native ligands of the heme iron are indicated.

polypeptide chain via two thioether linkages of the two vinyl side chains of the heme with two cysteine residues (Cys-14 and Cys-17). The heme iron is axially coordinated to two protein ligands, a methionine (Met-80) and a histidine (His-18), so that the low-spin state is inherent to both the ferric and ferrous forms. Crystallographic studies indicate minimal structural differences between the oxidized and reduced heme.^{31,32} The heme has a solvent exposed edge which is surrounded by seven lysine residues that are important in binding to the physiological partners.^{33,34} Overall dipole moments of 308 and 325 Debye were calculated for the oxidized and reduced protein, respectively.³⁵ Cyt *c* carries a +8 charge at neutral pH,³⁶ making it a good candidate for electrostatic binding interactions.

The formal redox potential for the horse heart ferri/ferrocyanochrome *c* redox couple in solution is 0.26 V vs. NHE at pH 7,³⁷ and was found to vary with temperature, pressure, electrolyte composition and ionic strength.³⁸

2.2 Cytochrome *c* oxidase

Cytochrome *c* oxidases (CcO) are the terminal membrane enzymes of the respiratory chain in mitochondria and aerobic bacteria. Their biological functions are to catalyze respiratory reduction of O₂ to water and to generate a transmembrane electrochemical potential, which is used for driving ATP synthesis. Cytochrome *c* oxidases are members of the superfamily of heme/copper terminal oxidases as indicated by the presence of histidine li-

gands to two heme groups and to a copper atom (Cu_B).^{39,40} In bacteria, the heme groups can be hemes *a*, *b* or *o*, whereas only heme *a* is found in mitochondrial enzymes.

The aa_3 -type oxidases include four redox centers: Cu_A in subunit II and heme *a*, heme a_3 and Cu_B in subunit I.⁴¹ Subunit I is best-conserved, subunit II is also well conserved. An additional subunit, subunit III, is present in all mitochondrial and most bacterial heme/copper oxidases and was shown to prevent suicide inactivation of the enzyme.⁴² Other subunits can be present in enzymes of different origin, their function is however rather enigmatic.⁴³ Subunits I-III are often called core subunits.⁴³ The bimetallic Cu_A is the primary electron acceptor from Cyt *c* at the periplasmic surface of the membrane. As depicted in Figure 2.2(a), electrons are transferred from Cu_A through low-spin heme *a* to the binuclear reaction center, composed of high-spin heme a_3 and Cu_B , where the catalysis of O_2 reduction takes place. Reduction of O_2 to water requires four electrons, one catalytic cycle consists thus of four one-electron transfer steps.

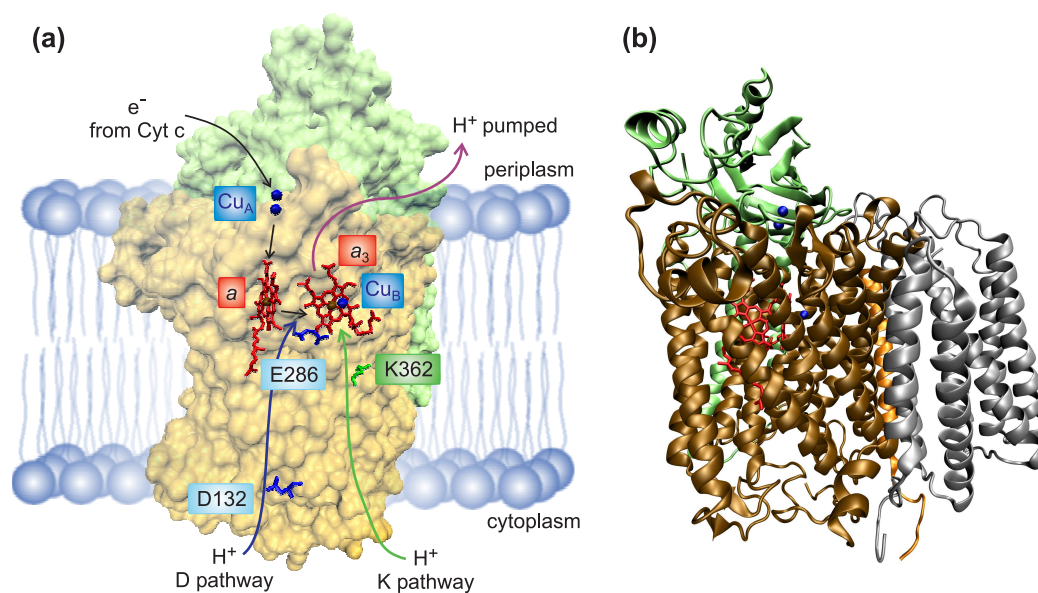


Figure 2.2: Structure and function of CcO from *Rhodobacter sphaeroides*. (a) Subunits I (light yellow) and II (light green) schematized in the membrane together with the four redox-active centers, Cu_A , heme *a*, heme a_3 and Cu_B . The electron transfer pathway is depicted in black, the three proton transfer pathways in blue, green and purple. (b) Structure of the enzyme: subunit I (brown), II (green), III (gray) and IV (orange). Heme groups are depicted in red and copper atoms in blue (Protein Data Bank ID code 1M56).⁴⁴

Electron transfer is coupled to the formation of an electrochemical gradient of protons across the membrane. Each electron transfer step is associated with uptake of a substrate proton into the heme a_3 /Cu_B binuclear center from the cytoplasmic side of the membrane to form the equivalent of water, and with translocation of a pumped proton across the membrane. Proton uptake takes place via two pathways, termed D and K according to the names of the entrance residues. The protons enter the D pathway at an aspartic acid residue (Asp-132) and proceed through a chain of conserved water molecules to a glutamic acid residue (Glu-286) in the vicinity of heme a_3 . The K pathway starts at a lysine residue (Lys-362). Pumped protons exit to the periplasmic side of the membrane by a mechanism which has not yet been identified.

The complexity of the physical and genetic structure in the mammalian CcO, which contains 13 subunits,⁴⁵ has made structural and functional analyses at a molecular level difficult. Some aerobic bacteria were found to synthesize cytochrome *c* oxidases that are simpler in structure, but have significant homology to the core subunits of the eukaryotic enzymes.⁴³ The aa_3 -type cytochrome *c* oxidases from *Paracoccus denitrificans*⁴⁶ and *Rhodobacter sphaeroides* have become the most widely used model enzymes for the mitochondrial cytochrome *c* oxidase. Specifically, *Rhodobacter sphaeroides*, as a member of the α subgroup of the purple bacteria from which mitochondria arose, synthesizes CcO which was shown to represent an excellent model system for the mammalian enzyme⁴⁷ and as such was investigated within this work.

The crystal structure at 2.3 Å of this enzyme is displayed in Figure 2.2(b). As can be inferred from the structure, both hemes are buried at equal depth in the membrane about 15 Å from the periplasmic side. The porphyrin planes of the hemes *a* and a_3 are perpendicular to the membrane surface and form an interplanar angle of ca. 105°. The heme groups are separated by the aromatic ring of phenylalanine at an edge-to-edge distance of only about 5 Å.

2.3 Resonance Raman spectroscopy of heme proteins

Heme containing redox proteins display typical UV-Vis absorption spectra with relatively broad bands like those shown in Figure 2.3 for the reduced and oxidized Cyt *c*. The absorption spectrum can be divided into two regions. The strong band in the near UV region at around 410 nm is termed Soret

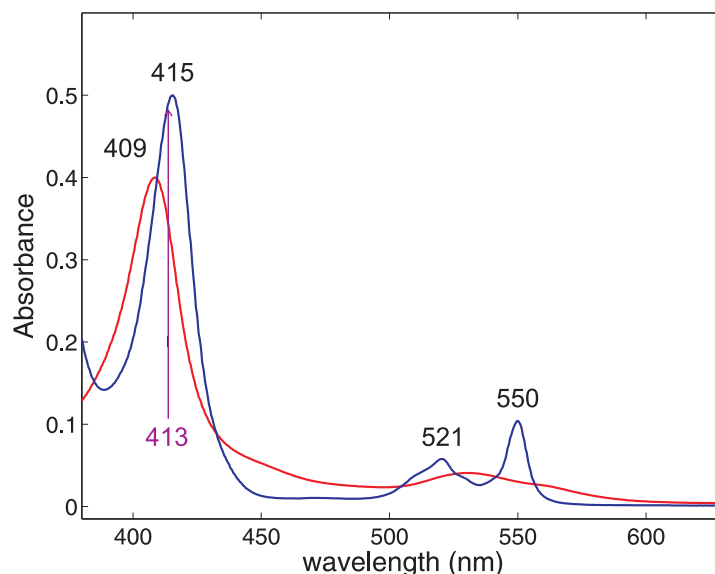


Figure 2.3: UV-Vis spectra of reduced (blue) and oxidized (red) horse heart Cyt *c* in solution. The excitation laser line at 413 nm is indicated by an arrow.

band and the weaker bands between 500 and 550 nm are called Q-bands. Both groups of bands stem from π - π^* electronic transitions of the heme group and upon proper excitation provide an opportunity to investigate resonance Raman spectra of heme proteins.

The heme group is composed of a porphyrin ring with an iron ion in the center. Various types of heme groups differ with respect to the porphyrin side chains as depicted in Figure 2.4. Idealized porphyrin model compounds with a D_{4h} symmetry were successfully employed to interpret resonance Raman spectra of different heme groups even if the effective symmetry of naturally occurring porphyrins is always lower. The electronic transition dipoles lie in the porphyrin plane and resonance enhancement is therefore expected only for the in-plane vibrational modes A_{1g} , B_{1g} , A_{2g} and B_{2g} . The totally symmetric A_{1g} modes dominate the RR spectrum upon excitation in the Soret band region via the A-term scattering mechanism as described in Section 1.2. The non-totally symmetric modes B_{1g} , A_{2g} and B_{2g} are enhanced by Herzberg-Teller vibronic coupling (B-term scattering) and are thus relatively strong upon excitation in the Q-band region. The different bands also display unique polarization properties. Only A_{1g} modes are polarized, B_{1g} and B_{2g} are depolarized and A_{2g} are anomalously polarized. Symmetry lowering of the heme groups with respect to the ideal D_{4h} symmetry can induce

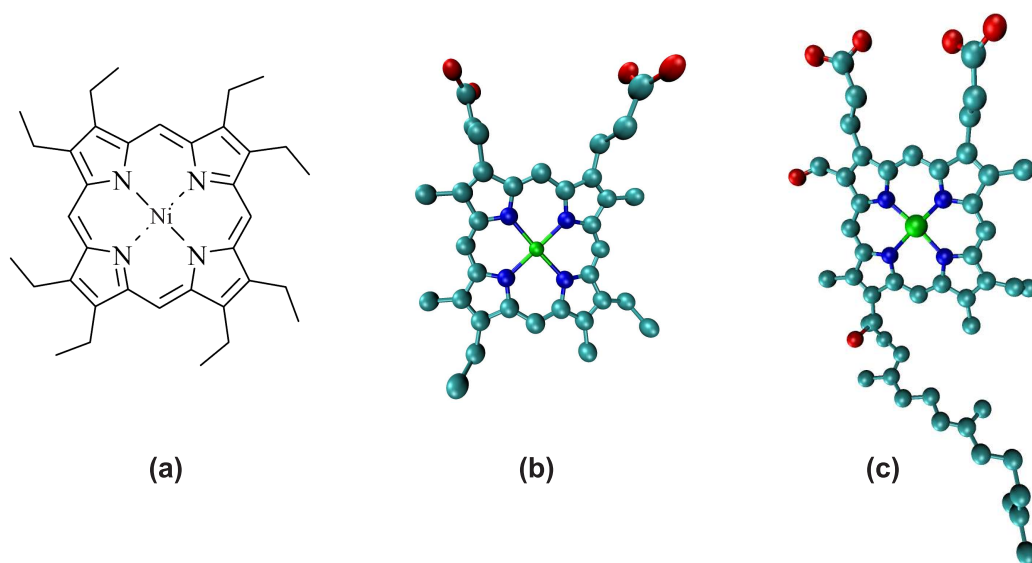


Figure 2.4: Hemes and heme model compounds: (a) nickel-octaethylporphyrin, (b) heme *c*, (c) heme *a*.

RR activity of D_{4h} -forbidden modes like the E_u or out-of-plane modes. Appearance of such bands in the RR spectrum points to a change in the heme environment or to a deformation of the porphyrin ring structure.

Excitation of heme proteins like Cyt *c* or CcO in the Soret absorption band gives rise to strong RR spectra. There are two regions of interest: the fingerprint region below 500 cm^{-1} and the marker band region between 1300 and 1700 cm^{-1} . The former one contains vibrations involving the peripheral substituents of the porphyrin and the latter one originates from modes which include C-C and C-N stretching vibrations of the porphyrin macrocycle. The spectroelectrochemical investigations within the present work are limited to the marker band region since it includes a variety of bands that allow an unambiguous determination of the oxidation, spin and coordination state of the heme. Indeed, positions of most of the marker bands depend on the core size of the macrocycle, i.e. on the pyrrole-nitrogen to core center distance. The core size of the porphyrin differs in a characteristic way for low spin (LS) and high spin (HS), six-coordinated (6c) and five-coordinated (5c), oxidized and reduced hemes.

2.3.1 Cytochrome *c*

The most prominent band in the RR spectrum of oxidized Cyt *c* at 1372 cm^{-1} (Figure 2.5) is assigned to the ν_4 mode* which corresponds to a nearly pure C-N stretching vibration. This mode shifts down by ca 10 cm^{-1} upon reduction. The large frequency change upon reduction of the central iron can be explained by an increase of the electron density in the antibonding π^* orbitals which in turn results in a weakening of the C-N bonds. As indicated in Figure 2.5, the ν_3 and ν_{10} also display important frequency downshifts upon reduction.

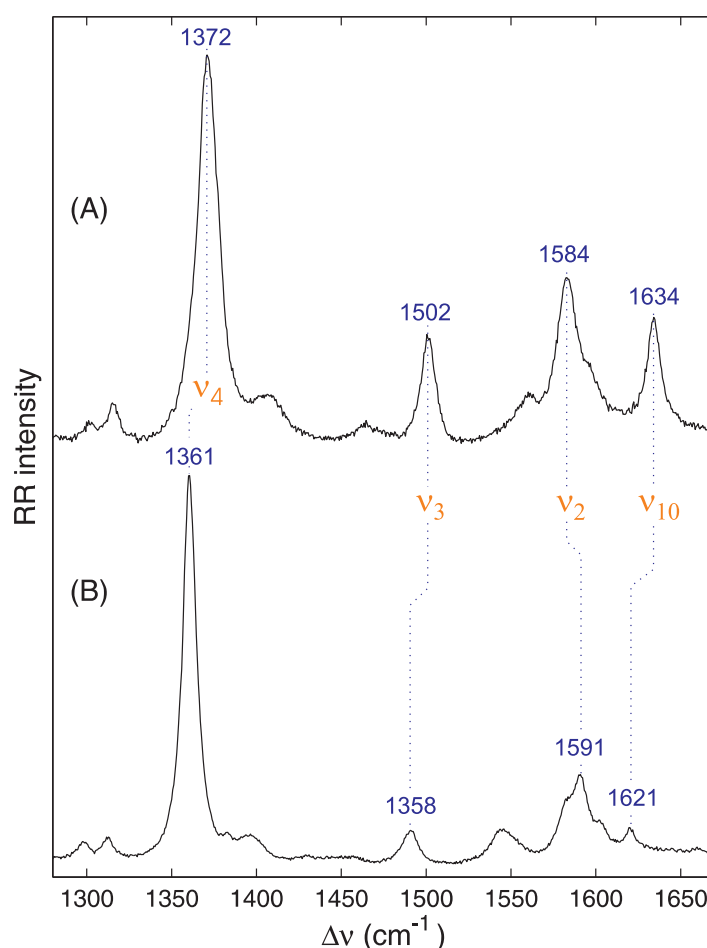


Figure 2.5: RR spectra of the native oxidized (A) and reduced (B) horse heart Cyt *c* in solution.

*Mode numbering refers to Abe et al.⁴⁸

Furthermore, the marker bands reflect the coordination and the spin state of the heme iron. The heme iron in the native Cyt *c* is coordinated to strong ligands (histidine and methionine). The ligand field splitting is much larger than the spin-pairing energy leaving only the d_{xy} , d_{xz} and d_{yz} orbitals occupied. Hence the central iron is in a LS state which is characterized by a small core size. The core size is increased if a strong ligand is replaced by a weak one or remains vacant forming a HS state with occupied d_{z^2} and $d_{x^2-y^2}$ orbitals. The heme iron remains in the plane of the porphyrin macrocycle in both 6c conformations but it is pulled towards the only axial ligand in the 5cHS species. Hence the core size increases in the following order 6cLS < 5cHS < 6cHS whereas the frequencies of the corresponding marker bands decrease accordingly.

2.3.2 Cytochrome *c* oxidase

Soret absorption bands of CcO appear at ca. 420 and 440 nm for the oxidized and reduced enzyme respectively. The resonance enhancement of the heme modes with excitation at 413 nm is thus expected to be lower than for Cyt *c*. RR spectra of fully oxidized and fully reduced CcO from *Rhodobacter sphaeroides* display a complex vibrational band pattern as shown in Figure 2.6. RR spectra of CcO from different organisms were investigated in a great detail and the band pattern was successfully disentangled.^{49,50,51} CcO contains two hemes in two different spin and ligation states – a 6cLS and a 6cHS configuration in heme *a* and heme *a*₃ respectively. Furthermore, the type-*a* hemes include a conjugated vinyl and formyl substituent which give rise to RR-active stretching vibrations between 1610 and 1680 cm⁻¹.

The most characteristic marker for the oxidation state originates from the ν_4 mode, which is found at ca. 1370 and 1358 cm⁻¹ in the RR spectra of the fully oxidized and fully reduced enzyme respectively (see Figure 2.6). These bands represent the envelopes of the closely spaced modes corresponding to the two hemes. However, heme *a* and heme *a*₃ can be distinguished on the basis of the formyl stretching modes. The weakly hydrogen-bonded formyl substituent of heme *a*₃ gives rise to an isolated band at 1671 and 1663 cm⁻¹ in the ferric and ferrous state. The substantially stronger hydrogen bonding interactions of the C=O group in heme *a* cause a distinct frequency downshift to 1646 and 1610 cm⁻¹ in the oxidized and reduced form, respectively. An additional unique marker band for the reduced heme *a* is the well-separated and relatively intense ν_{11} mode at 1517 cm⁻¹.

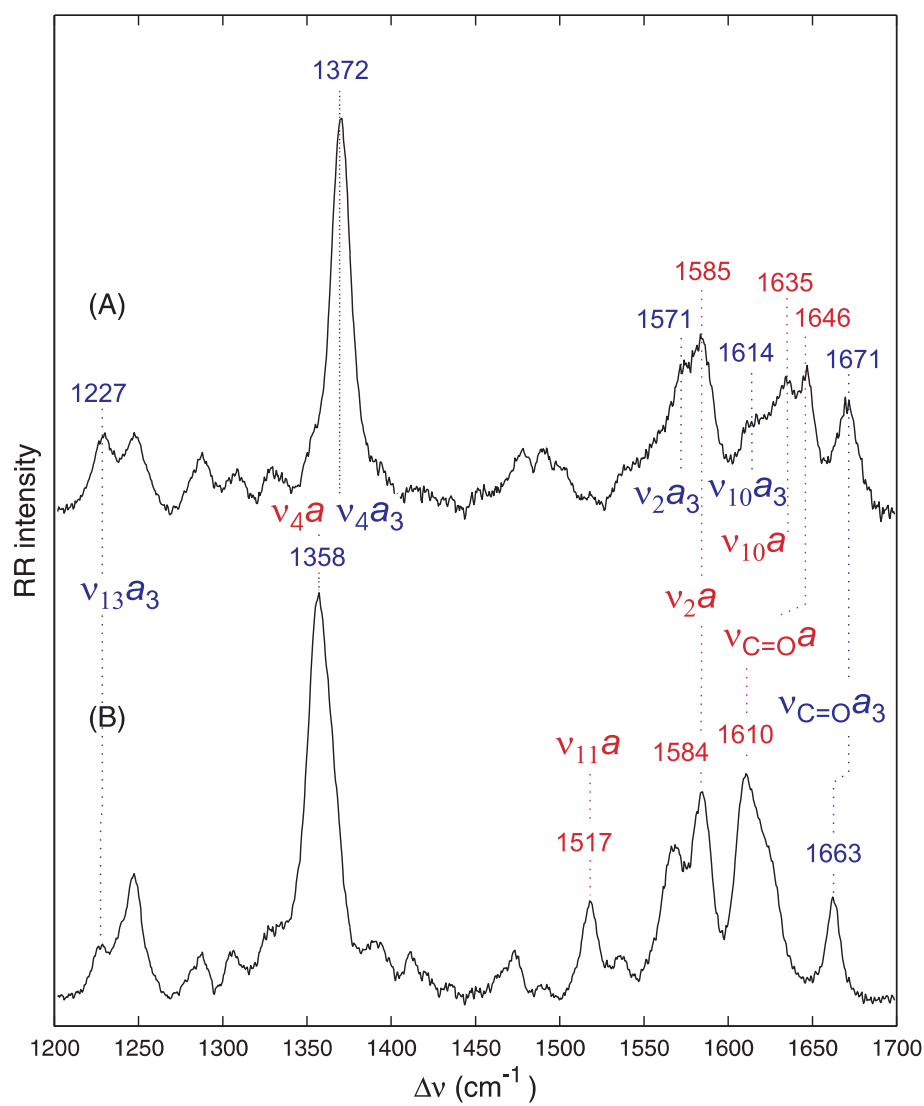


Figure 2.6: RR spectra of CcO in the oxidized (A) and reduced (B) form.

2.4 Surface-enhanced resonance Raman spectroscopy of heme proteins

The present work focuses on surface-enhanced resonance Raman (SERR) investigations of redox proteins. The combination of resonance and surface enhancement results in an up to 10^{12} -fold increase of intensity compared to classical Raman spectra. While exciting the heme proteins in the electronic transition of the porphyrin cycle, advantage is taken of the selective enhancement of the heme group modes without contributions from the protein matrix. The surface enhancement is provided by an electrochemically roughened silver electrode which offers a satisfactory surface enhancement at the excitation wavelength corresponding to the Soret absorption band. The protein is separated from the metal surface by a spacer of different length, the electromagnetic mechanism accounts thus for the SER effect. Moreover, the surface enhancement is limited to the protein attached to the metal surface. Hence the combination of SERR spectroscopy and electrochemistry allows to monitor structural changes of the redox sites as a function of potential.

Chapter 3

Electrochemical interfaces

As outlined in the Introduction, reactions at electrodes represent a suitable model system for biological processes at the membrane/solvent interface. Reactions at electrochemical interfaces take place under conditions that are significantly different from the bulk solution and therefore deserve a special attention.

In general, two processes can take place at electrode surfaces. Non-faradaic processes involve accumulation of charges at the metal/solution interface and other processes that are not associated with charge transfer across the interface. These processes will be the topic of the next sections. Faradaic processes are associated with electron transfer across the interface. Theory of electron transfer in solution and at electrodes will be detailed in the next chapter.

3.1 Electrode-solution interface

The simplest model of the interface between an electrode and an electrolyte is an electrical double layer, which consists of a sheet of positive charges at the surface of the metal and an accumulation of negative charges next to the interface in the solution or vice versa. This arrangement creates an electrical potential difference between the metal electrode and the bulk solution. Different models, schematized in Figure 3.1, attempt to describe the gradual potential changes in the electrical double layer.

In the Helmholtz model, the solvated ions arrange themselves in the so-called outer Helmholtz plane along the charged electrode surface but are kept away from it by their hydration shells. The electrical potential decays linearly between the electrode and the outer Helmholtz plane. The Gouy-Chapman model of the diffuse double layer accounts for the disordering effects

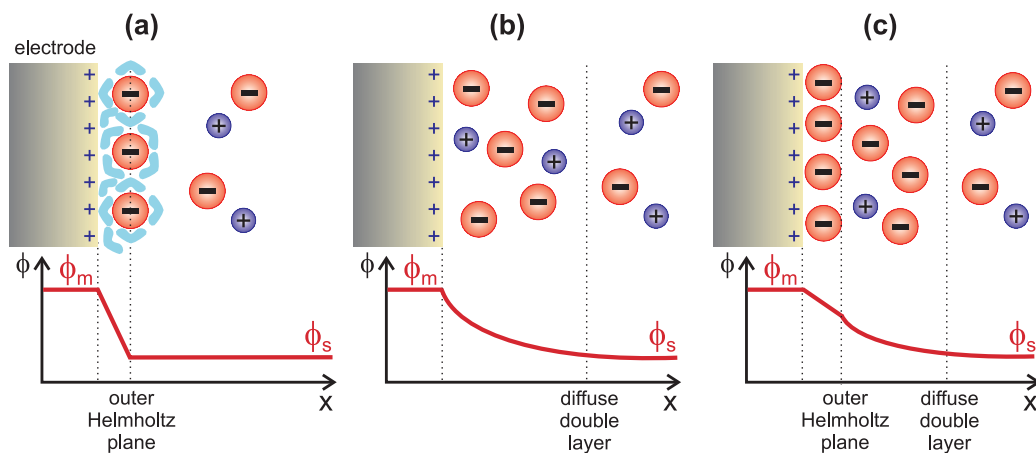


Figure 3.1: Models of the electrical double layer at the electrode-solution interface: (a) Helmholtz, (b) Gouy-Chapman and (c) Stern model.

of thermal motion. The two models are combined in the Stern model, in which ions in the immediate vicinity of the electrode are constrained into a rigid Helmholtz plane while outside that plane ions are dispersed like in the Gouy-Chapman model.⁵²

These simple models can account for electrode reactions of small compounds in direct contact with the electrode. More complex models have to be developed for protein reactions at electrode surfaces. Moreover, direct adsorption of proteins to metal electrodes frequently causes denaturation of the biomolecules.⁵³ Therefore methods have been developed to prevent direct contact of the protein with the metal.

3.2 Self-assembled monolayers

Self-assembled monolayers (SAMs) provide a flexible and simple system with which the interfacial properties of electrodes can be tailored. Of special interest is the ability of properly chosen SAMs to form biocompatible coatings on electrode surfaces and thus enable immobilization of proteins under preservation of their native structure.^{9,38} Moreover, the surface structure can be extensively varied in a systematic manner and probed with different experimental methods.

SAMs are organic assemblies formed by the adsorption of molecular constituents from solution or gas phase onto the surface of solids. The adsorbates organize spontaneously into crystalline or semicrystalline structures. The most widely used class of SAMs results from the adsorption of alkanethiols on metal electrodes (Au, Ag, Cu, Pd, Pt). At the opposite side of the thiol

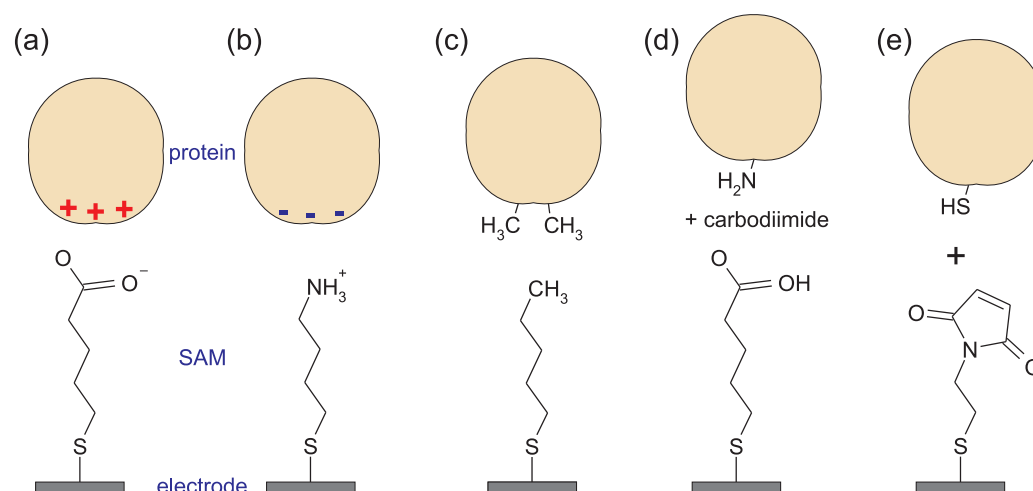


Figure 3.2: SAM-functionalized electrodes for different modes of protein immobilization: (a), (b) electrostatic adsorption; (c) hydrophobic attachment; (d), (e) covalent linkage.

group, alkanethiols can have a terminal chemical functionality which specifically binds a chosen substrate. The high affinity of thiols for the surface of noble and coinage metals makes it possible to generate well-defined organic surfaces with highly alterable chemical functionalities displayed at the exposed interface. Alkanethiols were shown to bind to Au and Ag surfaces in the form of chemisorbed thiolates.² In electrochemical investigations of proteins, SAMs are usually stable in the potential range of interest presenting very negative potentials of reductive desorption (typically < -0.6 V vs. NHE).^{54,55}

For protein immobilization, the functionality of the terminal group has to be adjusted to the desired mode of binding and to protein properties. Electrostatic interaction can be achieved by employing SAMs with charged terminal functional groups. Electrostatic immobilization is well suited for proteins with a defined dipole moment that can be adsorbed in a largely uniform orientation. The positively charged Cyt *c* was shown to adsorb to carboxylate-terminated SAMs upon preservation of the native structure.⁵⁶ The cationic binding domain is defined by positively charged lysine residues surrounding the heme crevice.³³ Proteins with anionic binding domains like cytochrome *b*₅₆₂ can be attached to positively charged SAMs composed of aminoalkanethiols.⁵⁷ Hydrophobic interfaces formed by methyl-terminated alkanethiols were employed to adsorb azurin⁵⁸ or Cyt *c*.⁵⁹ Covalent attachment can be obtained by forming peptide bonds between amino or carboxyl side chains of the protein's amino acids and corresponding terminal func-

tional groups of the SAM.⁶⁰ More specific covalent binding can be achieved by reacting maleimide terminal functionalities with thiols of cysteines, that either occur naturally in a limited amount or can be engineered in a well-defined manner by site-directed mutagenesis.⁶¹ The described modes of protein attachment are schematized in Figure 3.2, some additional ways of immobilization are extensively treated in the experimental part of this work.

3.3 Interfacial potential distribution

SAMs provide not only a biocompatible interface for immobilization of proteins, they offer also the possibility to control the electric field strength at the protein binding site.^{9,10} Indeed, if ions are unable to penetrate into the molecular film, the interfacial potential profile is expected to be characterized by a linear potential distribution through the film and a nonlinear potential decay in the solution phase as schematized in Figure 3.3. The interfacial potential distribution across the electrode/SAM/protein/solution interface can be then described by a simple electrostatic model.^{62,63,64}

As depicted in Figure 3.3, the model system consists of a metal electrode at $x = 0$ covered by a dielectric film of thickness d_f and dielectric constant ϵ_f . The redox center (RC) is situated at $x = d_f + d_{rc}$ surrounded by the protein matrix with a dielectric constant ϵ_p . The redox protein is in contact with an electrolyte solution that has a dielectric constant ϵ_p . Assuming that the only charges in the system are associated with the SAM terminal functional groups and with the redox centers, the electrostatic potential decays linearly from ϕ_m to ϕ_f and from ϕ_f to ϕ_{rc} . In the solution phase, the potential distribution is governed by the Gouy-Chapman model and decays to the electrostatic potential of the bulk solution (ϕ_s).

The potential profile through the interface can be expressed simply in terms of charge densities on the electrode surface (σ_m), at the SAM/protein interface (σ_f), at the redox site (σ_{rc}), in the bulk solution (σ_s) and electric field strengths throughout the system

$$E = \begin{cases} 0 & x < 0 \\ (\phi_m - \phi_f)/d_f & 0 < x < d_f \\ (\phi_f - \phi_{rc})/d_{rc} & d_f < x < d_{rc} \\ \kappa \left(\frac{2k_B T}{ze} \right) \sinh \left(ze \frac{\phi_x - \phi_s}{2k_B T} \right) & x > (d_f + d_{rc}) \\ 0 & x \rightarrow \infty \end{cases} \quad (3.1)$$

in which κ stands for the inverse Debye length, ϕ_x represents the potential in the electrolyte solution at position x , k_B is the Boltzmann constant, T

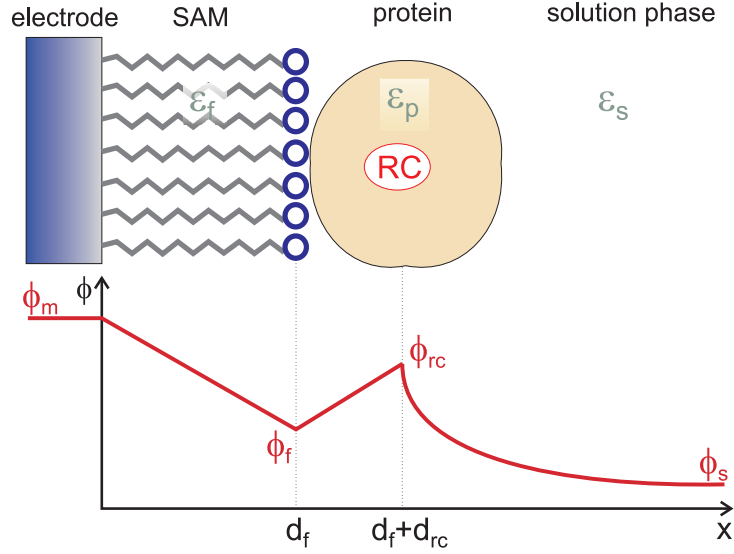


Figure 3.3: Schematic representation of the interfacial potential distribution at the electrode/SAM/protein/solution interface. RC denotes the redox center of the adsorbed protein.

the absolute temperature, z the charge of the electrolyte ions and e the elementary charge.

The potential distribution influences the electron transfer reaction of the immobilized protein. Indeed the potential experienced by the redox center of the adsorbed protein (E_{exp}) is related to the electrode potential (E) by

$$E_{exp} = E - E_{rc}, \quad (3.2)$$

where E_{rc} denotes the potential drop at the redox center defined as

$$E_{rc} = \phi_{rc} - \phi_s. \quad (3.3)$$

Application of Gauss's law, which relates electric fields and charge densities, to the model system in Figure 3.3 results in an expression for the potential drop at the redox center

$$E_{rc} = \frac{\sigma_f \epsilon_p d_f + \epsilon_0 \epsilon_p \epsilon_f (E - E_{pzc}) + \sigma_{rc} (d_f \epsilon_p + d_{rc} \epsilon_f)}{\epsilon_0 [\epsilon_f \epsilon_p + \epsilon_s \kappa (d_f \epsilon_p + d_{rc} \epsilon_f)]}, \quad (3.4)$$

where E_{pzc} denotes the potential of zero charge of the electrode. The relation for the electric field strength in the SAM (at distances $0 < x < d_f$) can be written as

$$E_f = \frac{\epsilon_0 \epsilon_s \kappa E_{rc} - \sigma_f - \sigma_{rc}}{\epsilon_0 \epsilon_f}. \quad (3.5)$$

The latter expression can be used to calculate the electric field strength at the protein binding site. Predictions for carboxylate-terminated SAMs on Ag electrodes indicate local electric field strengths at the protein binding site in the order of 10^9 Vm^{-1} ,⁶⁴ which is comparable to the values expected in the vicinity of charged phospholipid head groups of biological membranes.³

Local electric field strengths can be also determined experimentally by inserting an appropriate reporter group into the SAM. Due to the vibrational Stark effect, vibrational frequencies of molecules like CO, NO or CN shift in response to the applied electric field.^{65,66} Specifically, nitrile groups were employed to characterize the diffuse double layer structure at electrochemical interfaces on a subnanometer distance scale showing good agreement with the values obtained by electrostatic theory.^{67,68,69}

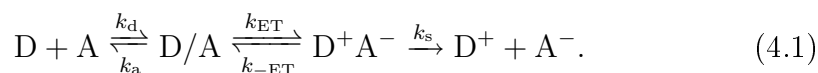
Chapter 4

Electron transfer theory

Electron transfer reactions play a central role in numerous essential biological processes as respiration or photosynthesis. Understanding electron transfer mechanism is of great importance in the development and operation of biosensors and biocatalytical devices. Simple electron transfer reactions count for the most rudimentary class of reactions in chemistry since they do not involve any breaking of bonds. The most famous and a relatively simple theory of electron transfer was introduced and developed by Marcus,⁷⁰ who was awarded the Nobel Prize in Chemistry in 1992. Numerous reviews provide comprehensive explanations of electron transfer theory.^{71,72,73}

4.1 General considerations

An electron transfer reaction between a donor D and an acceptor A in solution can be divided into three steps. First, D and A diffuse together to form a close-contact encounter complex D/A. In a second step, this complex reorganizes to a transition state in which electron transfer occurs and finally the product ions D⁺ and A⁻ diffuse apart. The overall reaction can be written as



In a steady-state approximation, the rate constant for this reaction is given by

$$\frac{1}{k_{\text{obs}}} = \frac{1}{k_a} + \frac{1}{K_A k_{ET}} \left(1 + \frac{k_{-ET}}{k_s} \right), \quad (4.2)$$

where $K_A = \frac{k_a}{k_d}$. Two extreme cases can be distinguished

$$\text{if } k_s \gg k_{-ET} \quad \text{and} \quad k_d \gg k_{ET} \quad k_{\text{obs}} = K_A k_{ET}, \quad (4.3)$$

$$\text{if } k_d \ll k_{ET} \quad k_{\text{obs}} = k_a. \quad (4.4)$$

In the second case, the observed rate constant does not contain any information about electron transfer, the rate of product formation is controlled by the formation of the D/A complex.

The difference in Gibbs energy between the initial and final state of reaction (4.1) may be approximated as

$$\Delta G^0 = e(E_D^0 - E_A^0) + w^P - w^R, \quad (4.5)$$

where E_D^0 and E_A^0 represent the standard redox potentials of the D^+/D and A/A^- redox couples. w^R and w^P denote the work of bringing the reactants together and the products apart.

4.2 Homogeneous electron transfer

4.2.1 Classical Marcus theory

The first generally accepted theory of electron transfer was developed by Marcus to address outer-sphere electron transfer reactions in solution and was based on a transition-state theory approach.⁷⁰

The potential energy of the reactants is a function of thousands of nuclear coordinates (vibrational coordinates of the reactants and orientational coordinates of the surrounding solvent molecules) and defines a many-dimensional potential-energy surface. In analogy to the reaction coordinate in the transition-state theory, a one-dimensional energy profile is introduced to describe electron transfer reactions. Whereas the potential energy profiles along the reaction coordinate are rather complicated, the profile of the Gibbs energy can be satisfactorily approximated by a parabola (see Figure 4.1). The curvature of the reactant and product energy profiles is assumed to be the same.

For electron transfer to occur, the reactants have to reach – brought by thermal fluctuations – the intersection region shown in Figure 4.1. According to the classical transition-state theory, the electron transfer rate constant is given by

$$k_{\text{ET}} = \kappa_{el} \nu_n \exp \left(\frac{-\Delta G^\ddagger}{k_B T} \right), \quad (4.6)$$

in which κ_{el} denotes the electronic transmission coefficient, ν_n stands for the vibrational frequency with which the activated complex approaches the transition state (typically $\nu_n \sim 10^{13} \text{ s}^{-1}$) and ΔG^\ddagger is the Gibbs energy of activation. As can be inferred from Figure 4.1, ΔG^\ddagger is related to the standard reaction Gibbs energy ΔG^0 and to the reorganization energy λ

$$\Delta G^\ddagger = \frac{(\lambda + \Delta G^0)^2}{4\lambda}. \quad (4.7)$$

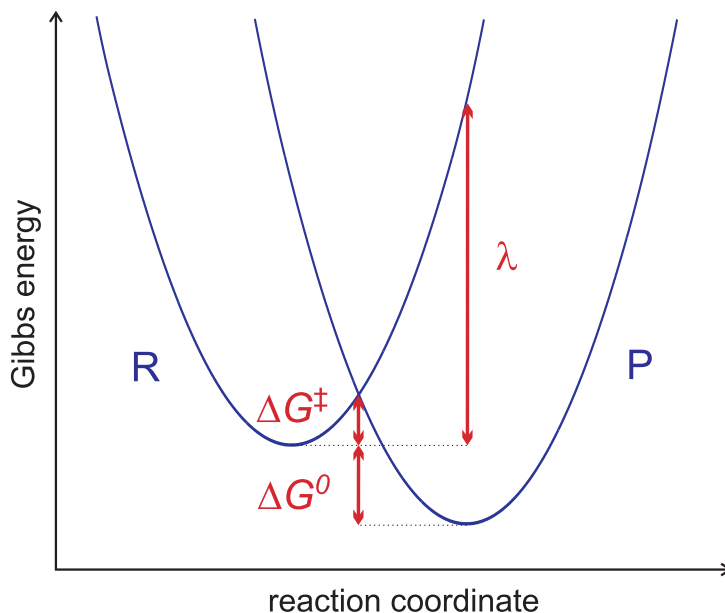


Figure 4.1: Profiles of the Gibbs energy surfaces for the reactant (R) and product (P) state.

λ is defined as the change in Gibbs energy of the reactant state if it moved along its energy profile to the product equilibrium state, i.e. without transfer of electron. Reorganization energy is usually divided into two contributions

$$\lambda = \lambda_i + \lambda_o. \quad (4.8)$$

The inner term λ_i arises from structural differences between the reactant and product states. The outer term λ_o reflects changes in orientation and polarization of solvent molecules.

Inserting eq (4.7) into eq (4.6) results in the classical Marcus equation

$$k_{\text{ET}} = \kappa_{el} \nu_n \exp \left[\frac{(\lambda + \Delta G^0)^2}{4\lambda k_B T} \right], \quad (4.9)$$

which predicts a maximum of the electron transfer rate for $-\Delta G^0 = \lambda$. As ΔG^0 becomes more negative, i.e. for a highly exergonic reaction, the electron transfer rate will decrease corresponding to the so-called Marcus inverted region. Experimental evidence was brought for this originally rather surprising theoretical prediction.^{74,75}

Two types of electron transfer reactions can be distinguished according to the magnitude of the electronic transmission coefficient. The reaction is termed as adiabatic if $\kappa_{el} = 1$, i.e. the probability that electron transfer at

the transition state occurs is equal to unity. If, on the other hand, $\kappa_{el} \ll 1$, the electron transfer reaction proceeds in the nonadiabatic regime. Hence, even when the electron reaches the intersection region of the R and P energy profiles, it only occasionally crosses over to the P surface.

4.2.2 Quantum mechanical treatment

Classical Marcus theory usually gives satisfactory results for adiabatic reactions. A quantum mechanical approach that accounts for electron and nuclear tunneling is required for nonadiabatic reactions. Indeed, in the quantum model, electron transfer is possible below the intersection point of the R and P energy profiles. Quantum mechanical formulations of electron transfer theory were developed by Jortner^{76,77,78}, Levich and Dogonadze⁷⁹.

The electronic coupling energy corresponds to the overlap of the electronic wave functions of the equilibrium reactant and product states, ψ_R^0 and ψ_P^0 , respectively

$$H_{DA} = \langle \psi_R^0 | \hat{H}_{el} | \psi_P^0 \rangle, \quad (4.10)$$

in which \hat{H}_{el} denotes the electronic Hamiltonian for the system in the Born-Oppenheimer approximation. The electronic coupling parameter reflects the exponential decay of electronic wave functions with distance

$$|H_{DA}(r)|^2 = |H_0|^2 \exp(-\beta(r - r_0)), \quad (4.11)$$

where $|H_0|^2$ represents the maximum electronic coupling at the van der Waals distance (r_0), r is the distance between the donor and acceptor and β an exponential decay coefficient, termed also tunneling parameter.

The probability of electron transition from an initial energy level in the reactant state to an energy level in the product state is described by the Fermi golden rule which is derived from time-dependent quantum mechanical perturbation theory. It follows for the first-order rate constant for a nonadiabatic electron transfer reaction for reactants fixed in position

$$k_{ET} = \frac{2\pi}{\hbar} |H_{DA}|^2 FCWD, \quad (4.12)$$

where \hbar is the Planck's constant. $FCWD$ denotes the Franck-Condon weighted density of states which corresponds to the integrated overlap of reactant and product nuclear wave functions of equal energy, weighted by Boltzmann factors

$$FCWD = \sum_{i,j} \langle \chi_{Pi}^0 | \chi_{Rj}^0 \rangle^2 P(\epsilon_{Rj}) \delta(\epsilon_{Pi} - \epsilon_{Rj}). \quad (4.13)$$

Here, χ_{Pi}^0 and χ_{Rj}^0 stand for the vibrational wave functions of the equilibrium product state at level i and of the equilibrium reactant state at level j , respectively. ϵ_{Pi} and ϵ_{Rj} are the vibrational energies of level i in the product state and of level j in the reactant state. $P(\epsilon_{Rj})$ denotes the probability of finding the reactant state in the level j with energy ϵ_{Rj} and δ is a Dirac delta function. The sum in eq (4.13) is taken over all internal and solvent vibrational modes, a full quantum formulation of eq (4.13) is thus rather complicated.

Different assumptions were introduced to express the Franck-Condon factors. Solvent vibrations usually occur at low frequencies and may be treated classically. Within this approximation, the semiclassical Marcus equation can be written as

$$k_{\text{ET}} = \frac{2\pi}{\hbar} |H_{\text{DA}}|^2 \frac{1}{\sqrt{4\pi\lambda_o k_{\text{B}}T}} \times \sum_{i,j} \langle \chi_{Pi}^0 | \chi_{Rj}^0 \rangle^2 P(\epsilon_{Rj}) \exp \left[-\frac{(\Delta G^0 + \epsilon_{Pi} - \epsilon_{Rj} + \lambda_o)^2}{4\lambda_o k_{\text{B}}T} \right] \quad (4.14)$$

in which λ_o denotes the solvent reorganization energy and the summation runs now only over the internal vibrational modes. Other treatments introduce a characteristic frequency which replaces the relevant high-frequency vibrations on the reactant state.⁷⁷

In the high-temperature limit, eq (4.14) reduces to

$$k_{\text{ET}} = \frac{2\pi}{\hbar} |H_{\text{DA}}|^2 \frac{1}{\sqrt{4\pi\lambda k_{\text{B}}T}} \exp \left[-\frac{(\lambda + \Delta G^0)^2}{4\lambda k_{\text{B}}T} \right], \quad (4.15)$$

where $\lambda = \lambda_o + \lambda_i$. Eq (4.15) is equivalent to eq (4.9) with

$$\kappa_{el}\nu_n = \frac{2\pi}{\hbar} |H_{\text{DA}}|^2 \frac{1}{\sqrt{4\pi\lambda k_{\text{B}}T}}. \quad (4.16)$$

4.3 Heterogeneous electron transfer

The same theoretical framework was applied to electrochemical electron transfer reactions after considering the relevant differences of the two systems.⁸⁰ The overall reaction can be in principle described by eq (4.1), the first and last step might be represented by the diffusion of the reactant to and from the electrode or by a conformational change of the reactant to and from a state that is favorable for electron transfer.

Unlike reactions in solution, the electron is transferred from a localized to a delocalized state (or vice versa) in a reaction at a metal electrode interface.

The driving force for the electron transfer reaction in solution is given by the difference in Gibbs energy of the donor and acceptor states which is replaced by the activation overpotential in the electrochemical process

$$\eta = E - E^0. \quad (4.17)$$

E denotes the actual electrode potential and E^0 represents the formal potential of the redox couple under study which is defined by the Nernst equation

$$E = E^0 - \frac{k_B T}{ne} \ln \frac{c_{\text{red}}}{c_{\text{ox}}}. \quad (4.18)$$

Here c_{red} and c_{ox} stand for the equilibrium concentrations of the reduced and oxidized electroactive species, respectively, and n represents the number of electrons transferred in the reaction.

The theoretical background of electrochemical electron transfer reactions is nevertheless not as well established as that of homogeneous reactions and still in progress. Insofar, the investigations have focused mostly on nonadiabatic heterogeneous electron transfer.⁸¹ In analogy to eq (4.15), a transition rate for one electronic level of energy ϵ in the metal can be expressed as

$$W(\epsilon, \eta) = \frac{2\pi}{\hbar} |H_{\text{DA}}(\epsilon)|^2 \frac{1}{\sqrt{4\pi\lambda k_B T}} \exp \left[-\frac{(\lambda + \Delta G^0(\epsilon, \eta))^2}{4\lambda k_B T} \right]. \quad (4.19)$$

Eq (4.19) has to be integrated over all occupied electronic levels in the electrode to yield an expression for the heterogeneous electron transfer rate

$$k_{\text{ET}} = \frac{2\pi}{\hbar} \frac{1}{\sqrt{4\pi\lambda k_B T}} \int d\epsilon f(\epsilon) \rho(\epsilon) |H_{\text{DA}}(\epsilon)|^2 \times \exp \left[-\frac{(\lambda + \Delta G^0(\epsilon, \eta))^2}{4\lambda k_B T} \right] \quad (4.20)$$

with

$$\Delta G^0(\epsilon, \eta) = \epsilon - \epsilon_f - e\eta \quad \text{for oxidation} \quad (4.21)$$

$$\Delta G^0(\epsilon, \eta) = -(\epsilon - \epsilon_f) + e\eta \quad \text{for reduction.} \quad (4.22)$$

Here, $\rho(\epsilon)$ is the density of states (DOS) of the metal electrode and

$$\rho(\epsilon) |H_{\text{DA}}(\epsilon)|^2 = |V(\epsilon)|^2 \quad (4.23)$$

corresponds to the metal-DOS weighted and k -space integrated electronic coupling strength. The Fermi-Dirac distribution function $f(\epsilon)$ defines the probability that an electronic level of energy ϵ is occupied by an electron

$$f(\epsilon) = \frac{1}{1 + \exp \left(\frac{\epsilon - \epsilon_f}{k_B T} \right)}, \quad (4.24)$$

in which ϵ_f denotes the Fermi energy.

A relatively simple expression for the electron transfer rate can be obtained by integrating eq (4.20) under several assumptions.^{82,83,84} First, the Fermi-Dirac distribution is replaced by a step function, DOS is considered to be independent of energy and finally the contributions from high and low energy levels ($\epsilon \gg \epsilon_f$ and $\epsilon \approx 0$, respectively) are neglected. The rate constant for oxidation can be then written as

$$k_{\text{ox}} = A \frac{\sqrt{\pi \lambda k_B T}}{e} \left(1 + \operatorname{erf} \frac{e\eta - \lambda}{2\sqrt{\lambda k_B T}} \right) \quad (4.25)$$

and the rate for reduction as

$$k_{\text{red}} = A \frac{\sqrt{\pi \lambda k_B T}}{e} \left(1 - \operatorname{erf} \frac{e\eta + \lambda}{2\sqrt{\lambda k_B T}} \right), \quad (4.26)$$

where the error function is defined as

$$\operatorname{erf}(x) = \frac{2}{\sqrt{\pi}} \int_0^x \exp(-t^2) dt. \quad (4.27)$$

A denotes a constant related to the electronic coupling term $|H_{\text{DA}}|^2$ and thus proportional to the exponential of the distance between the weakly coupled electron donor and acceptor.⁸³

4.4 Effect of friction on electron transfer

Early electron transfer theories do not explicitly consider the many degrees of freedom corresponding to the atoms of the molecules, that are not directly involved in electron transfer, including the solvent. Indeed, in biological and chemical electron transfer, a nuclear reaction coordinate is coupled to other nuclear and/or solvent related coordinates resulting in a transfer of energy which would classically be interpreted as dissipation or friction. If electron transfer occurs at a comparable time scale as the reorientation of solvent molecules, the observed electron transfer rate will be determined by solvent dynamics.

Several theoretical approaches were used to include friction into expressions for homogeneous electron transfer rate. The effect of solvent dynamics was considered by Zusman⁸⁵ who used the stochastic approach to describe electron transfer reactions in different solvents. For a transition between two states, Zusman formulated master equations for partial populations of the corresponding states and solved them for different limiting cases.^{86,87} Garg

et al. used path integral methods to account for the dependence of the reaction rate on friction and came to essentially identical master equations as Zusman.⁸⁸

In most cases, a modified form of eq (4.15) still applies

$$k_{\text{ET}} = \frac{2\pi}{\hbar} |H_{\text{DA}}|^2 \frac{1}{\sqrt{4\pi\lambda k_{\text{B}}T}} \left(\frac{1}{1+g} \right) \exp \left[-\frac{(\lambda + \Delta G^0)^2}{4\lambda k_{\text{B}}T} \right], \quad (4.28)$$

The adiabacity factor g is defined as

$$g = k_{\text{NA}} F \tau_L, \quad (4.29)$$

where k_{NA} denotes the nonadiabatic electron transfer rate, F is a function of the ratios $\frac{\lambda_i}{\lambda_o}$ and $\frac{\Delta G^\ddagger}{k_{\text{B}}T}$ and τ_L represents the longitudinal relaxation time of the solvent.

For the rate of electron transfer at an electrode, Zusman derived the following expression⁸⁹

$$k_{\text{fric}} = \frac{1}{\pi \tau_S} \sqrt{\frac{\lambda}{\pi k_{\text{B}}T}} \sin \left(\pi \sqrt{\frac{\Delta G^\ddagger}{\lambda}} \right) \exp \left(-\frac{\Delta G^\ddagger}{k_{\text{B}}T} \right) \quad (4.30)$$

$$\times \ln \left[1 + \pi \tau_S k_{\text{NA}} \sqrt{\frac{\pi k_{\text{B}}T}{\lambda}} \frac{\exp \left(\frac{\Delta G^\ddagger}{k_{\text{B}}T} \right)}{\sin \left(\pi \sqrt{\frac{\Delta G^\ddagger}{\lambda}} \right)} \right], \quad (4.31)$$

where τ_S denotes a characteristic polarization relaxation time of the solvent. An expression for the rate constant in the limit of weak electronic interaction, k_{NA} , was derived in the previous section (eq (4.25) and (4.26) for oxidation and reduction, respectively).

In the limit where

$$k_{\text{NA}} \ll \frac{1}{\pi \tau_S} \sqrt{\frac{\lambda}{\pi k_{\text{B}}T}} \sin \left(\pi \sqrt{\frac{\Delta G^\ddagger}{\lambda}} \right) \exp \left(-\frac{\Delta G^\ddagger}{k_{\text{B}}T} \right) \quad (4.32)$$

the electron transfer rate is limited by electron tunneling and eq (4.30) reduces to $k_{\text{fric}} = k_{\text{NA}}$. If, on the other hand,

$$k_{\text{NA}} \gg \frac{1}{\pi \tau_S} \sqrt{\frac{\lambda}{\pi k_{\text{B}}T}} \sin \left(\pi \sqrt{\frac{\Delta G^\ddagger}{\lambda}} \right) \exp \left(-\frac{\Delta G^\ddagger}{k_{\text{B}}T} \right) \quad (4.33)$$

the electron transfer rate is inversely proportional to the polarization relaxation time of the medium

$$k_{\text{fric}} = \frac{1}{\pi\tau_S} \sqrt{\frac{\lambda}{\pi k_B T}} \sin\left(\pi \sqrt{\frac{\Delta G^\ddagger}{\lambda}}\right) \exp\left(-\frac{\Delta G^\ddagger}{k_B T}\right) \times \ln \left[\pi\tau_S k_{\text{NA}} \sqrt{\frac{\pi k_B T}{\lambda}} \frac{\exp\left(\frac{\Delta G^\ddagger}{k_B T}\right)}{\sin\left(\pi \sqrt{\frac{\Delta G^\ddagger}{\lambda}}\right)} \right]. \quad (4.34)$$

Eq (4.34) simplifies somewhat at zero overpotential if the reorganization energy can be approximated as classical

$$k_{\text{fric}}^0 = \frac{1}{\pi\tau_S} \sqrt{\frac{\lambda}{\pi k_B T}} \exp\left(-\frac{\lambda}{4k_B T}\right) \ln \left[B \frac{\tau_S}{\lambda} \right], \quad (4.35)$$

in which B is a constant that contains the electronic coupling parameter.

Part III

Experimental methods and data treatment

Chapter 5

Electrochemistry

5.1 Electrochemical cells

Spectroelectrochemical measurements were performed on specifically modified Ag electrodes as will be described in the next chapter. The coated electrode was inserted in a three-electrode electrochemical cell where it functioned as the working electrode (WE). The cell was further equipped with a platinum (Pt) counter electrode (CE) and a Ag/AgCl/saturated KCl reference electrode (RE) (Dri-Ref, World Precision Instruments). The Pt CE consists of a roughly 5 cm long wire with a diameter of 0.5 mm. Dri-Ref RE has a diameter of 2 mm and is 13 cm long. Electrode potentials were controlled with a potentiostat (Potentiostat/Galvanostat Model 263 A, EG&G Princeton Applied Research). All potentials reported in this work refer to the Ag/AgCl (sat. KCl) reference electrode ($E^0 = 198$ mV vs. NHE).

Two different geometries of electrochemical cells and working electrodes (depicted in Figure 5.1) were used and will be described in the next sections.

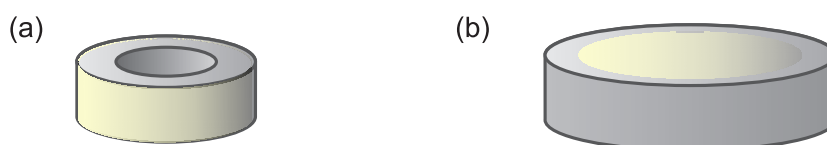


Figure 5.1: Ag working electrodes: (a) ring electrode and (b) disk electrode. The active surface of the electrode is indicated in pale yellow.

5.1.1 Ring electrode system

The Ag working electrode commonly used in our group has the form of a ring, is 2.5 mm high and 8 mm in diameter (0.6 cm² of geometric surface

exposed to the solution). The corresponding electrochemical cell is shown in Figure 5.2. This electrochemical cell, made of Delrin* with a volume of about 10 mL, was used for SERR investigations of the Cyt *c* systems. The working electrode is mounted onto a rotational shaft which is coupled to a motor and provides the electrical contact between the electrode and the potentiostat. The Ag electrode can be thus efficiently rotated during experiments to prevent laser induced sample degradation. The electrochemical cell is equipped with counter and reference electrodes as described above, optical windows for spectroscopic measurements and a gas inlet which allows to perform experiments under continuous purging with argon.

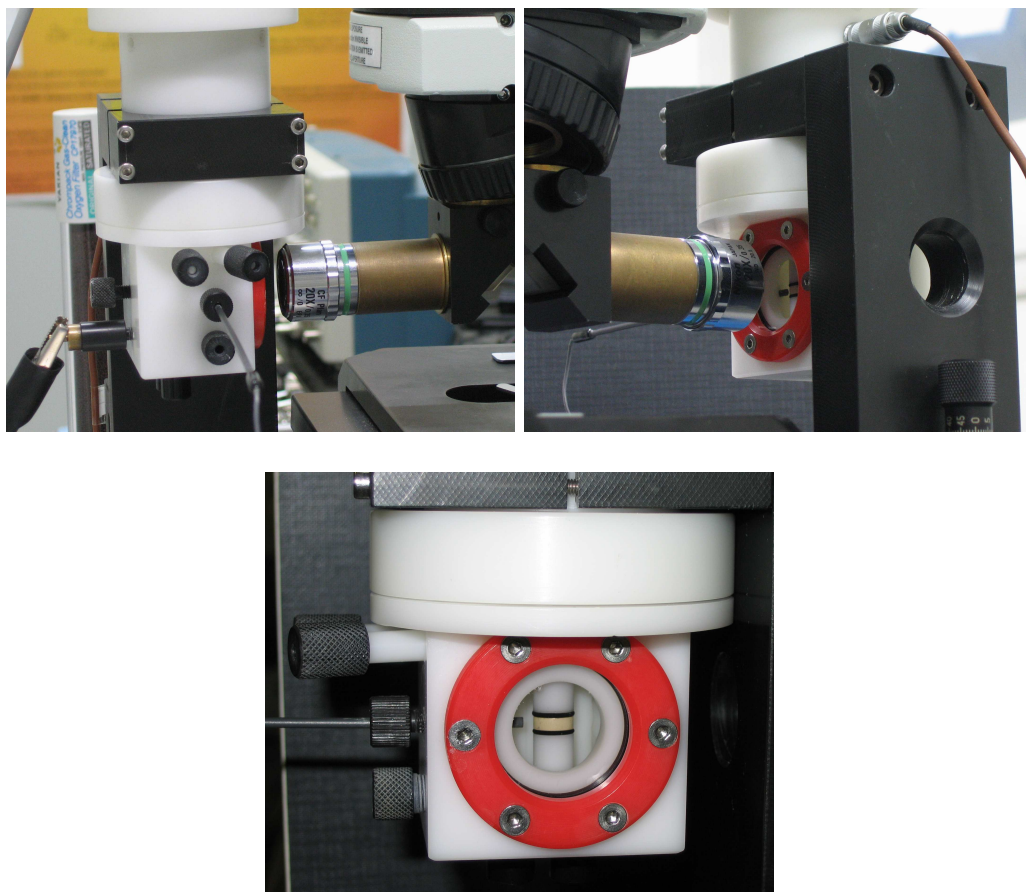


Figure 5.2: Electrochemical cell used with ring electrodes. The cell is mounted on the holder, in place for spectroscopic measurements and viewed from different sides.

*Delrin is a brand name for an acetal resin engineering plastic, polyoxymethylene.

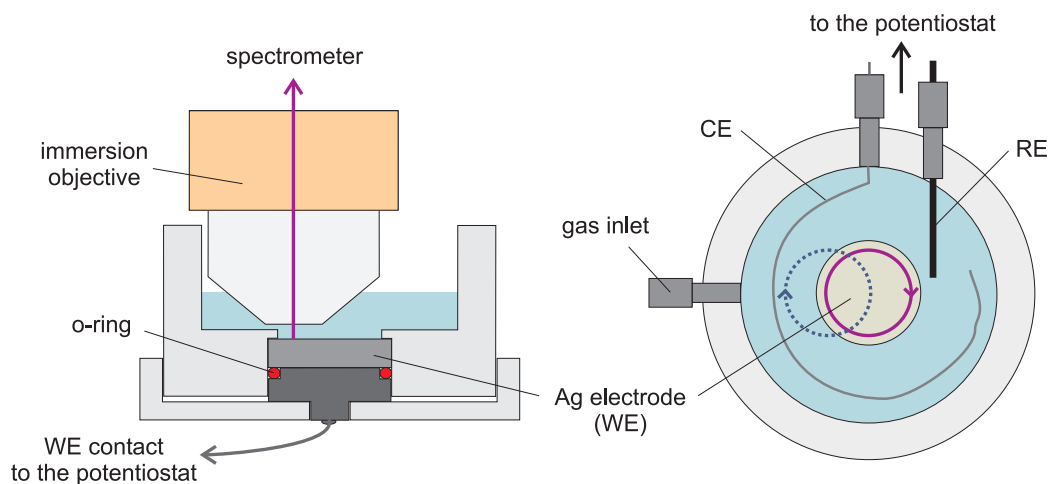


Figure 5.3: New electrochemical cell from the side (left) and from the top (right). The blue dotted line shows the cell movement and the violet line the corresponding laser spot trajectory. The outer diameter of the cell is 52 mm and the inner diameter 32 mm.

5.1.2 Disk electrode system

The ring-shaped WE is not well suited for *CcO* experiments due to the relatively poor SERR signal and multi-step preparation procedure. A new electrochemical cell (Figure 5.3) was thus designed for a flat disk Ag electrode (12.5 mm in diameter, 0.8 cm² of geometric surface exposed to the solution) which is easier to handle during preparation. The new cell contains a three-electrode system including the disk Ag WE, a Pt CE and a Ag/AgCl RE. The disk WE is tightly screwed to the bottom part of the cell assuring thereby a good contact to the potentiostat. It is also equipped with a gas inlet. The material of the cell is nylon which was chosen because of its lower affinity to molecular oxygen compared to Delrin.[†] The cell is open and thus compatible with the short working distance (1.5 mm) of an immersion microscope objective, as illustrated in Figure 5.3. Moreover, the new cell requires a much lower buffer volume (< 2 mL). For measurements under anaerobic conditions, the electrochemical cell was accommodated in an elastic plastic tent and purged with catalytically pure oxygen-free argon gas for 1 hour before measurement. Argon overpressure was maintained in the tent during the SERR experiment.

In order to avoid laser induced sample degradation and minimize photoreduction (detailed later), the electrochemical cell was mounted on an eccen-

[†]Interestingly, it was observed that whereas Cyt *c* readily adsorbs to the walls of the Delrin cell, it does not stick to the nylon cell.

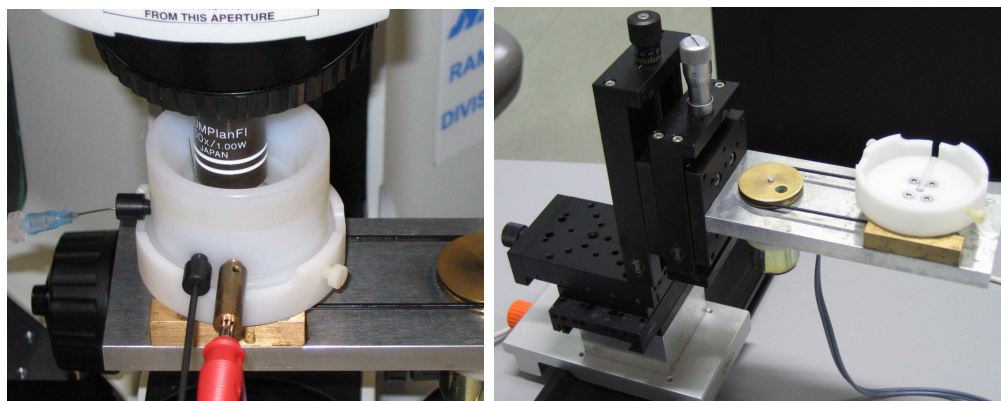


Figure 5.4: Electrochemical cell used with disk electrodes: (left) cell in position for spectroscopic measurements, (right) eccentrically rotating cell holder.

trically rotating device coupled to a motor (see photos in Figure 5.4) so that the electrode surface was continuously moved with respect to the incident laser beam (as indicated in Figure 5.3).

5.2 Cyclic voltammetry

For the Cyt *c*-polyelectrolyte system, cyclic voltammograms (CV) were acquired from the modified ring Ag electrodes before and after SERR investigations using the same electrochemical cell. The potentiostat was controlled by an Electrochemistry PowerSuite software (version 2.57, Princeton Applied Research) and a GPIB board. Cyclic voltammograms were acquired in the range from -200 mV to $+200$ mV (or from -150 mV to $+150$ mV) at different scan rates, most frequently at 0.1 Vs $^{-1}$.

CV anodic and cathodic peak parameters (potential, current, charge and FWHM) were determined with the help of the PowerSuite software by subtracting a linear baseline from the CV scans. Further treatment of the voltammograms is described in the corresponding sections.

Chapter 6

Electrode preparation

The Ag working electrodes were first subjected to an electrochemical treatment in order to produce a rough SER-active surface and were subsequently coated with different types of SAMs in order to prepare a biocompatible interface for protein adsorption. Two different types of Ag electrodes were employed as described in the previous section, i.e. ring electrodes for Cyt *c* and disk electrodes for CcO immobilization.

6.1 Preparation of the SER-active surface

The preparation procedure of the SER-active surface followed a protocol similar to that described previously.⁹⁰ After mechanical polishing with abrasive paper, the Ag electrode was thoroughly rinsed with distilled water and ethanol and inserted into an electrochemical cell containing 0.1 M KCl. Two different auxiliary three-electrode electrochemical cells were used for roughening of the ring and disk electrodes. They principally resemble those described in the previous section, are however made of plexiglass, are more elementary and do not comprise optical windows. The potential was first set to -2.0 V for 20 s for hydrogen evolution, the bubbles sticking to the electrode were carefully removed. The electrode was subsequently subjected to three Ag oxidation-reduction cycles at +0.3 and -0.3 V respectively for 60, 20 and 20 s at each potential in each cycle. Finally, the Ag rough electrode was rinsed with distilled water and ethanol and dried under a stream of nitrogen gas.

6.2 Immobilization strategies

Three different techniques were employed to immobilize the redox proteins under study, two for the soluble Cyt *c* and one for the membrane bound CcO.

6.2.1 Coordinative binding of Cyt *c*

The heme group of Cyt *c* can be directly wired to an electrode coated with a SAM consisting of a nitrogen containing terminal group like pyridine.

Bis[6-((4-pyridinylcarbonyl)oxy)hexanyl]disulfide was synthesized in the group of D. H. Waldeck.⁹¹ 1-pentanethiol (98%) was obtained from Aldrich and used without further purification. Horse heart cytochrome *c* was purchased from Sigma and purified according to published procedures.⁹²

The electrochemically roughened Ag ring electrodes were immersed in an ethanolic solution containing 1 mM -S(CH₂)₆OOC(C₅H₄N) (PyC₆) and -S(CH₂)₄CH₃ (C₅) (the mole ratio of PyC₆ to C₅ was 1:9). The electrode remained in this solution for 1 day to form mixed self-assembled monolayers. Modified electrodes were subsequently rinsed with ethanol, dried by a stream of nitrogen gas and inserted into the electrochemical cell. The cell contained a 20 mM phosphate buffer (pH 7.0) and 0.2 μ M Cyt *c*. Cyt *c* was let to adsorb for 1 hour. The electrolyte solution was continuously purged with argon gas before and during the experiments. The mode of immobilization is schematized in Figure 6.1.

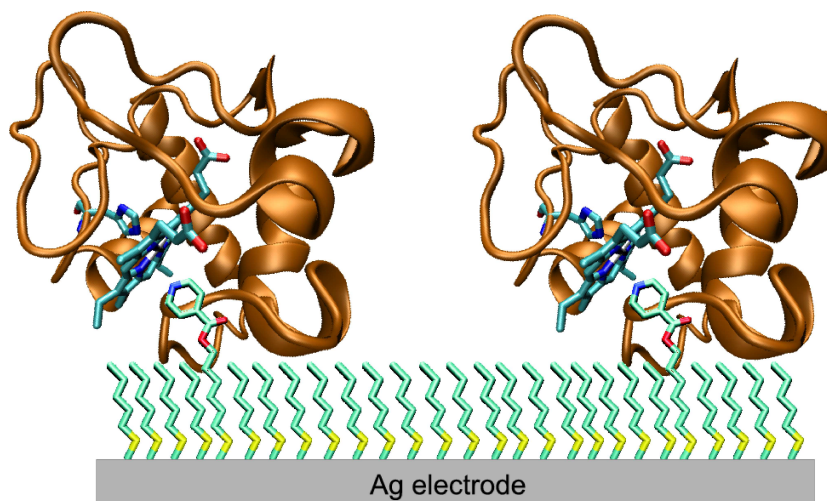


Figure 6.1: Immobilization of Cyt *c* on Ag electrodes via coordinative binding to pyridine-terminated alkanethiols self-assembled on the metal surface.

6.2.2 Cyt *c* immobilized within a polyelectrolyte layer

Buffer A stands for a 5 mM phosphate buffer (pH 7.0) and buffer B denotes a 0.5 mM phosphate buffer (pH 5.0).

The electrochemically roughened Ag ring electrode was immersed in a 1:3 mixture of 5 mM 11-mercaptoundecanoic acid (MUA) and 5 mM 11-mercaptoundecanol (MU) in ethanol for 2 days to form a stable mixed self-assembled monolayer (MUA/MU SAM). After washing with ethanol and buffer A the MUA/MU modified electrode was incubated for 2 hours in a 20 μ M Cyt *c* solution (buffer A) and washed with buffer A. The system Ag-MUA/MU-Cyt *c* is then used as a template for creating alternating multilayers of an anionic polyelectrolyte (poly(aniline sulfonic acid); PASA, Figure 6.2) and Cyt *c*. The multilayers were created using the layer-by-layer adsorption technique (Figure 6.3), that consists in alternating immersion steps in PASA solution (0.2 mg/mL in buffer B) and Cyt *c* solution (20 μ M in buffer B). For each step the electrode was dipped for 10 minutes into the corresponding solution and washed afterwards with buffer B. Some preparations were subjected to thermal treatment which was found to stabilize the multilayer assembly. For this purpose, the electrodes were incubated in buffer B at 45°C for 30 minutes.

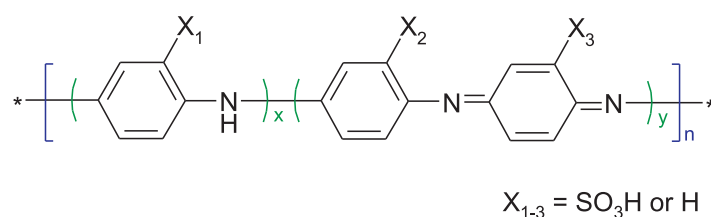


Figure 6.2: Poly(aniline sulfonic acid) (PASA).

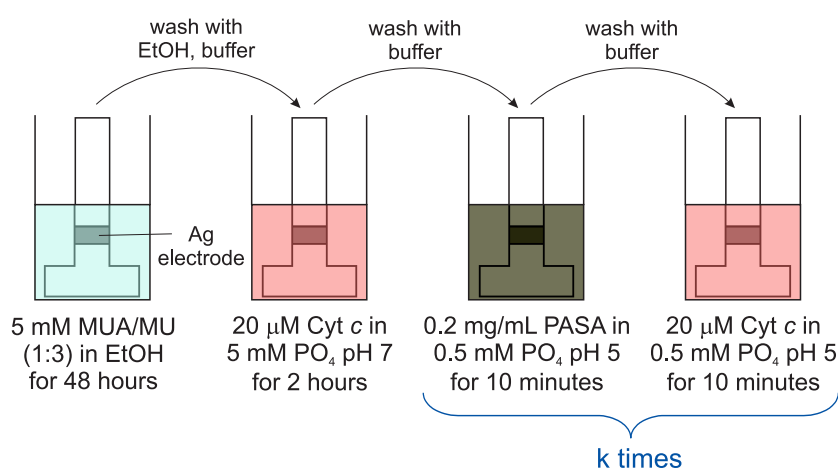


Figure 6.3: Layer-by-layer adsorption technique: preparation of a Ag-MUA/MU-Cyt *c*-(PASA-Cyt *c*)_k electrode.

In some experiments, Cyt *c* was replaced by the redox and SERR inactive apocytochrome *c*. Horse heart apocytochrome *c* was prepared by chemical removal of the heme group from the protein in the group of F. Lisdat (Max Planck Institute of Colloids and Interfaces in Golm) according to a published procedure.⁹³

6.2.3 His-tag immobilization of CcO

The immobilization procedure is based on the affinity of a His-tagged cytochrome *c* oxidase towards a metal ion chelating coating of the electrode, this method is inspired by the metal ion affinity chromatography. Two different protein variants of CcO from *Rhodobacter sphaeroides* have been used with the six-histidine-tag (His-tag) engineered to the C-terminus of subunit I (CcO-I) or to the C-terminus of subunit II (CcO-II). The His-tagged proteins have been expressed and purified in the group of J. Heberle as described elsewhere.^{94,95}

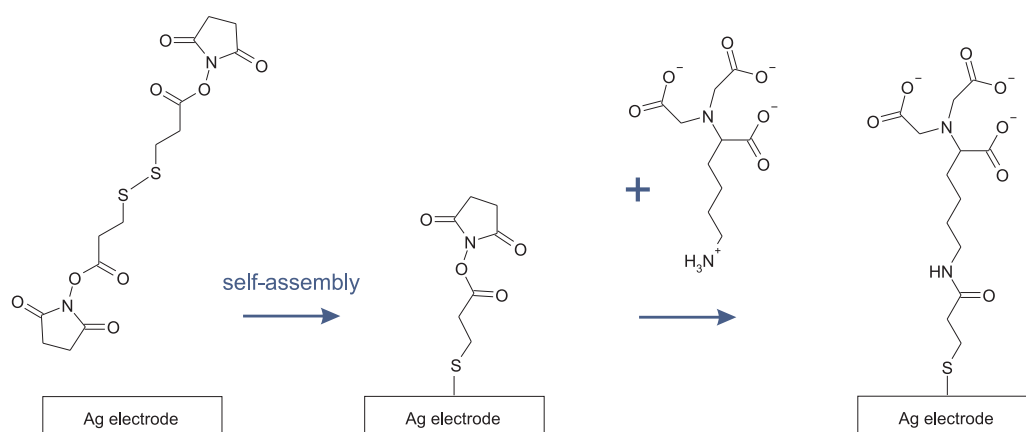


Figure 6.4: Two-step modification of the Ag electrode with an NTA SAM: self-assembly of DTSP on the surface followed by the reaction with A-NTA.

For protein immobilization, the rough Ag disk electrodes have to be coated with a SAM containing the metal chelating nitrilo-triacetic acid (NTA) as the functional group. Originally, this surface modification was done in two steps that are depicted in Figure 6.4.^{96,97} First the Ag disk electrode was immersed in a solution of dithiobis-(*N*-succinimidyl propionate) (DTSP, Sigma) in DMSO (2 mg.mL^{-1}) for 60 min. After rinsing with DMSO and ethanol, the dried modified surface was placed into an aqueous solution (pH 9.8, $0.5 \text{ M K}_2\text{CO}_3$) of $0.15 \text{ M N}_\alpha, \text{N}_\alpha$ -bis(carboxymethyl)-L-lysine (A-NTA, Fluka) for 3 hours. Later on this two step preparation was simplified

with the help of a commercially available NTA terminated thiol compound. The rough Ag disk electrodes were then immersed in an 1 mM aqueous solution of 3,3'-dithiobis[*N*-(5-amino-5-carboxypentyl)propionamide-*N*',*N*'-diacetic acid] (dithiobis(C2-NTA), Dojindo) for roughly 15 hours.

Both preparation procedures yielded an NTA terminated SAM on the electrode surface. In order to activate the coordination sites for the His-tag, the Ag electrode was immersed in 40 mM NiCl_2 or 40 mM ZnCl_2 (50 mM acetate buffer, pH 5.5) for ca. 1 hour. After rinsing with water, the electrode was incubated in a phosphate buffer solution (50 mM, pH 8, 100 mM KCl) containing 0.2 μM CcO and 0.1% *n*-dodecyl- β -D-maltoside (DDM, Sigma) for 2 hours (Figure 6.5). The electrode was then rinsed with buffer/DDM solution in order to remove excess protein. For reconstitution of the lipid environment, the electrode was subsequently immersed in a buffer/DDM solution containing additionally 0.05 $\text{mg}\cdot\text{mL}^{-1}$ 1,2-diphytanoyl-*sn*-glycero-3-phosphocholine (Avanti Polar Lipids) for 30 min. Finally, the detergent was removed by addition of Bio-Beads (Bio-Rad) to the solution for 2 hours under continuous stirring.^{98,99} The immobilized enzyme after membrane reconstitution is shown in Figure 6.6 for the two different orientations.

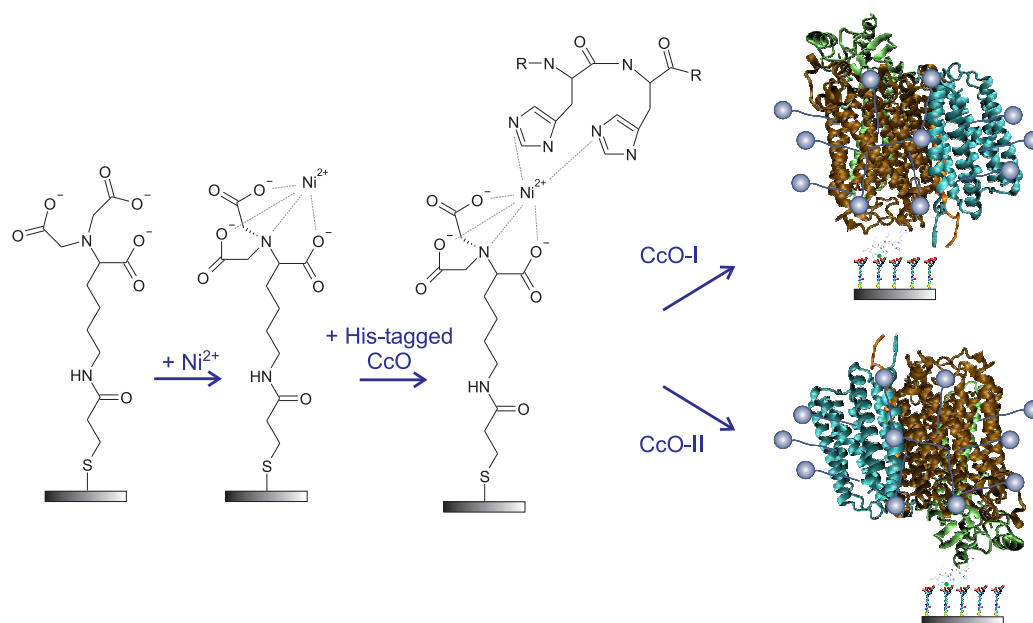


Figure 6.5: CcO immobilization procedure: activation of the NTA SAM by Ni^{2+} ions and subsequent attachment of the His-tagged detergent-solubilized CcO (structure from *Rhodobacter sphaeroides*, PDB code 1M56). Brown: subunit I, green: subunit II, cyan: subunit III and orange: subunit IV.

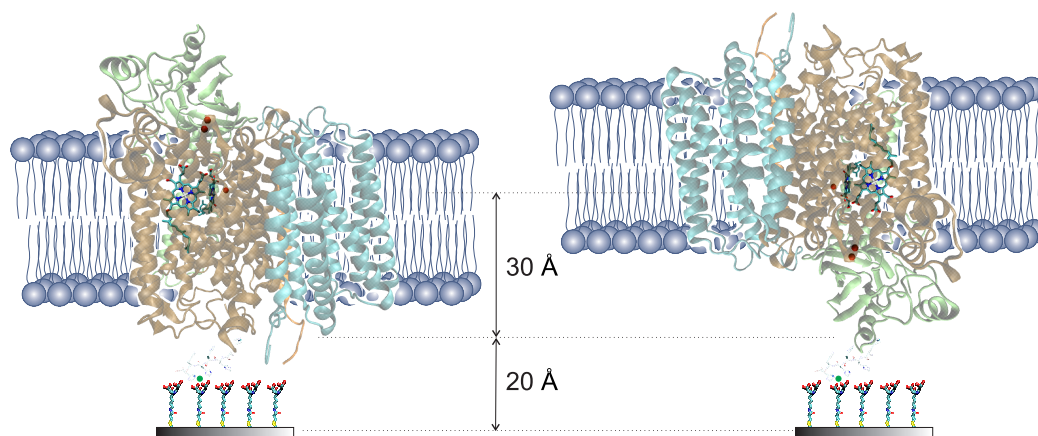


Figure 6.6: Immobilized CcO after reconstitution of the lipid environment in the two different orientations (left CcO-I and right CcO-II). Structure of CcO from *Rhodobacter sphaeroides* (PDB code 1M56). Cu atoms are depicted as red spheres, the position of the two hemes is indicated.

New holder type which allows to perform all preparation steps in an easy way without electrode manipulation was realized by the mechanical workshop (see Figure 6.7). The holder was made of nylon like the electrochemical cell. As depicted in Figure 6.7, very small sample volumes ($< 200 \mu\text{L}$) were sufficient for incubation of the electrode in the alkanethiol and protein solution. This represents a decrease in material consumption by a factor of about 20 with respect to the standard ring electrodes. The holder was also designed to facilitate the detergent removal by Bio-Beads. For this purpose, the holder is rotated by 90° so that the disk electrode is in an upright position. The holder is filled with 1 mL of the appropriate solution, Bio-Beads and a stirring bar are inserted and the holder is placed on a magnetic stirrer.

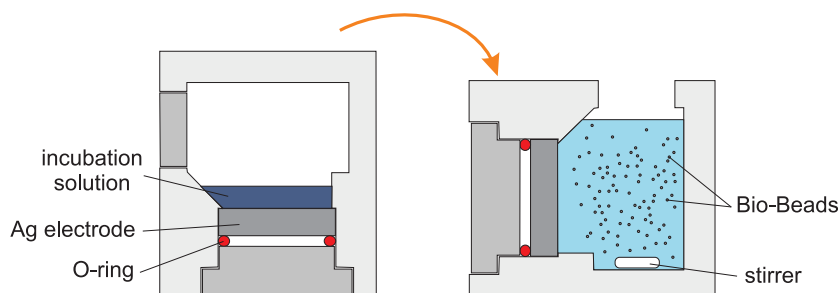


Figure 6.7: New nylon holder for the disk electrode preparation (side view): (left) incubation of the electrode with small sample volumes (SAM, protein) and (right) detergent removal by Bio-Beads under continuous stirring.

Chapter 7

RR and SERR spectroscopy

7.1 Experimental setup

Raman spectra were measured at ambient temperature using a confocal Raman microscope (LabRam HR-800, Jobin Yvon) equipped with a liquid nitrogen cooled back-illuminated CCD[†] detector. Experimental configuration is schematized in Figure 7.1, the abbreviations used in the text below refer to the figure.

Cyt *c* and CcO were excited in the Soret absorption band with the 413 nm laser line of a Kr⁺ laser (Innova 300, Coherent). The laser beam passed through two consecutive laser modulators, which were employed to create laser pulses for the time-resolved experiments (see below), and entered the spectrometer part. Laser plasma lines were removed by an interference filter (IF). After passing a pinhole (P) the laser beam was reflected by a dichroic beam-splitter (DS) towards the microscope part (Olympus BX 40). The beam was focused on the sample by means of a microscope objective (O). For RR measurements in solution, the sample was contained in a spinning quartz cell. Most experiments were performed on a modified Ag electrode in an electrochemical cell as described above. A long working distance (24 mm) objective (Olympus, 20 \times , NA 0.35) was employed for Cyt *c* measurements and a water immersion objective (Olympus, 100 \times , NA 1.00) with a working distance of 1.5 mm for CcO experiments. An additional adapter was mounted to the objective holder in order to enable horizontal detection with the long working distance objective, as illustrated in Figure 5.2.

Raman signals were collected in the 180° geometry by the same objective (O). The scattered radiation passed through the dichroic beam splitter (DS) which operates in transmission mode as a first notch filter and then

[†]charge-coupled device

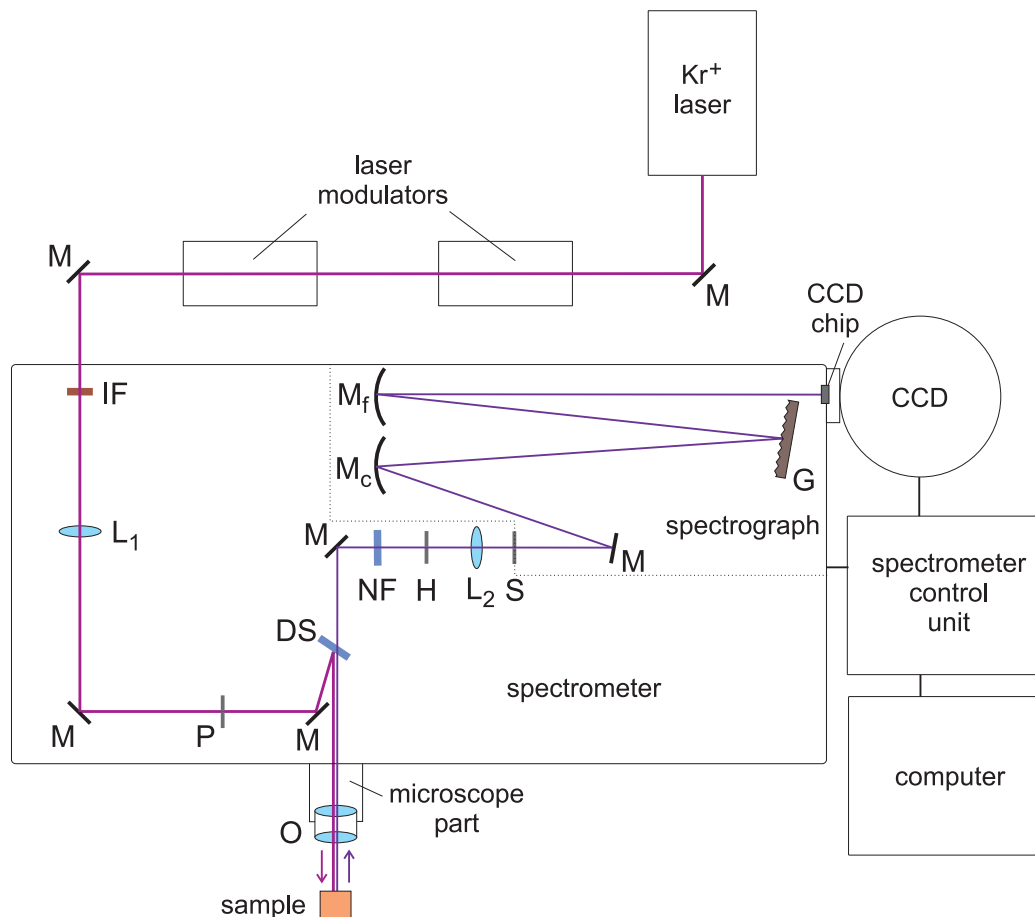


Figure 7.1: Experimental setup for Raman measurements. The sample consisted mostly of a modified Ag electrode, it can also be a quartz rotating cell for RR measurements in solution.

Legend:	DS	dichroic mirror/notch filter	M_c	colimating mirror
	G	grating	M_f	focusing mirror
	H	confocal hole	NF	notch filter
	IF	interference filter	O	microscope objective
	L	lense	P	pinhole
	M	mirror	S	slit

through a second notch filter (NF). This arrangement allows to efficiently remove the elastic Rayleigh scattering. The light collected by the objective was focused onto a confocal hole (H) adjusted to 1000 μm . An additional lense (L_2) focuses the scattered radiation onto a slit at the entrance of the spectrograph. The width of the entrance slit was set to 100 μm . The spectrograph consists of a single monochromator with two interchangeable gratings (G) with groove densities of 2400 and 600 1/mm, the 2400 1/mm was used throughout. The monochromator in the Czerny-Turner design has a focal length of 800 mm. The scattered light was dispersed by the grating (G) and focused on a CCD chip. The dimensions of the chip are 2048×512 . Usually, spectra were acquired with a binning factor of 2, i.e. intensities of two adjacent pixels are summed up. This setting implies a spectral resolution of 2 cm^{-1} and a wavenumber increment per pixel of 0.57 cm^{-1} . The spectrometer is controlled by the LabSpec[®] software (version 4.07, Dilor-Jobin Yvon-Spex) which removes the cosmic radiation peaks. The spectrograph was calibrated before and after each experiment with a standard mercury lamp. The reported frequencies are accurate to $\pm 0.5 \text{ cm}^{-1}$.

7.2 Stationary and time-resolved SERR spectroscopy

Stationary SERR spectra were acquired as a function of potential in the range between -0.65 and +0.2 V. SERR spectra at a given potential were measured after ca. 1 min of equilibration time and accumulated for 4-10 s in the case of Cyt *c* and 20 s during CcO investigations. In the latter case, several accumulations at each potential were performed and summed up in order to improve the signal-to-noise ratio (real accumulation time corresponds to at least 1 min).

Time-resolved (TR) SERR spectroelectrochemistry consist in synchronizing fast potential jumps with short measuring intervals.⁹⁰ As depicted in Figure 7.2, potential jumps of variable height and duration are applied in a TR-SERR experiment to trigger the redox reaction. The relaxation process is probed by measuring SERR spectra at variable delay times δ after each jump. Following the measurement interval Δ , the electrode potential is reset to the initial value during a sample recovery phase, which must be long enough to restore the original equilibrium. The sequence of potential jumps is repeated until SERR spectra reach sufficient signal-to-noise ratio. The TR-SERR technique assumes a full reversibility of the potential-induced processes.

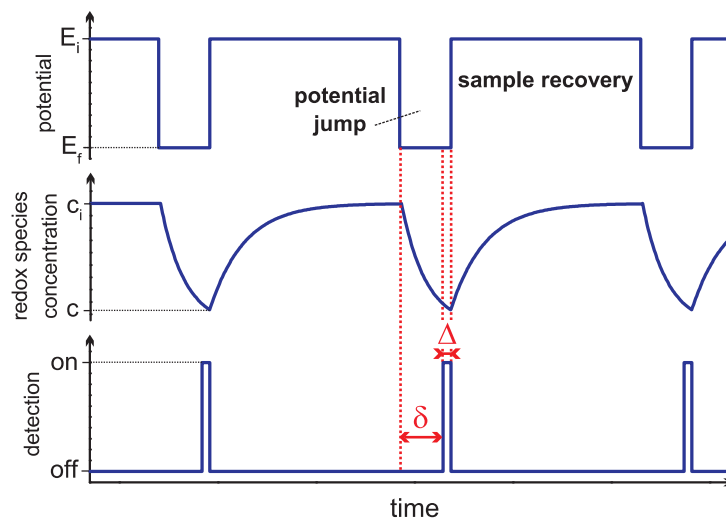


Figure 7.2: TR-SERR setup.

Synchronization of potential jumps and measuring laser pulses is achieved with a home made four channel pulse-delay generator. The measuring laser pulses are generated by passing the continuous-wave laser beam through two consecutive laser intensity modulators (LM 0202, Linos) which are controlled by digital pulse amplifiers (Linos) and give a total extinction better than 1:25000 and a time response of 20 ns. The real accumulation time of the TR-SERR spectra was 1-4 s (the real accumulation time is the product of the measuring laser pulse length Δ and the number of cycles). The time-dependent results are displayed as a function of the delay time δ' defined as $\delta' = \delta + \frac{\Delta}{2}$.

Chapter 8

Spectra treatment

A meaningful quantitative analysis of SERR spectra requires a proper and reproducible baseline subtraction. For spectra of high signal-to-noise ratio (SNR) this task can be accomplished by simple polynomial subtraction. If SNR becomes unfavorable, complex background shapes are observed and the measured spectra reflect significantly more the variations in spectrometer sensitivity. Therefore, a more careful pretreatment, which includes accounting for the instrument response function and proper baseline correction, is required for spectra with low SNR before they are subjected to quantitative analysis.

8.1 CCD image correction

Immobilized CcO gives rise to lower signals than Cyt *c* owing to the weaker resonance enhancement (Soret absorption of the hemes is more far away from the excitation line) and poor surface enhancement (higher distance from the electrode). Longer accumulation times are therefore required in order to get an acceptable SNR in CcO spectra. Nevertheless, it was observed that accumulation times longer than 1 minute did not improve the spectral quality. On the contrary, a strange pattern started to appear. This pattern was independent of the spectral region or, in other words, of the grating position and thus related to the properties of the CCD chip. This observation was confirmed by acquiring spectra of white light at different spectrometer positions and plotting them as a function of pixel number (see Figure 8.1). There is no reason to expect such a complicated structure in the case of uniform illumination.

CCD arrays are mechanically quite stable, however, each pixel within the

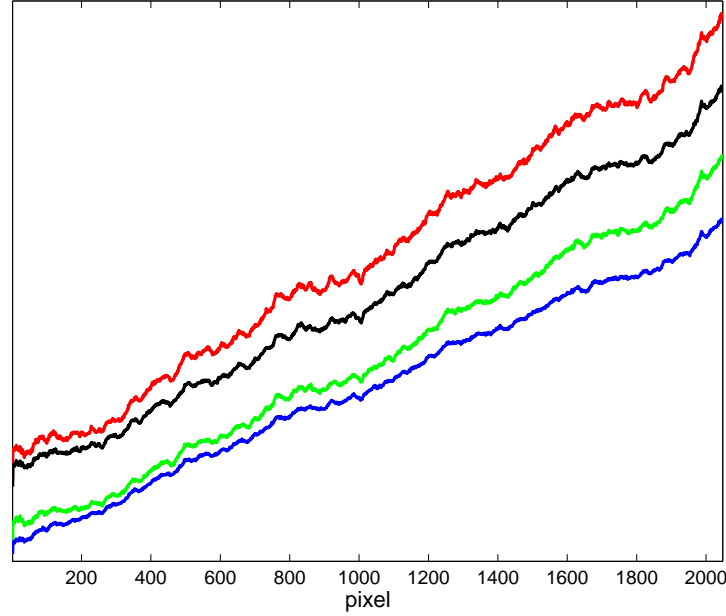


Figure 8.1: Spectra of the white lamp acquired with the binning of 1 at different monochromator positions: 900 cm^{-1} (blue), 1500 cm^{-1} (green), 1600 cm^{-1} (black) and 2100 cm^{-1} (red).

array has a unique light sensitivity characteristic.* The pixel characteristics affect the CCD image quality and thus have to be removed through calibration which is known as flat fielding. In order to perform this correction, it is necessary to acquire a CCD image under uniform illumination which is called the flat field image. In a two dimensional CCD image, raw data are then calibrated according to

$$R_{ij} = A_{ij} \frac{\langle m \rangle}{F_{ij}} \quad (8.1)$$

where R and A are matrices corresponding to the corrected and raw data respectively, F stands for the flat field CCD image and $\langle m \rangle$ represents the mean of the entire flat field.

In the case of spectroscopic measurements, the intensities along one dimension are integrated yielding a one dimensional vector. The different light sensitivities of the individual pixels in one column are also summed up. Therefore, the distortion of the spectral intensity will depend on the horizontal area of the CCD chip chosen for accumulation (this option offered by the operating software helps to reduce the noise coming from regions out of focus). It is thus necessary to record a flat field spectrum under identical

*www.roperscientific.de

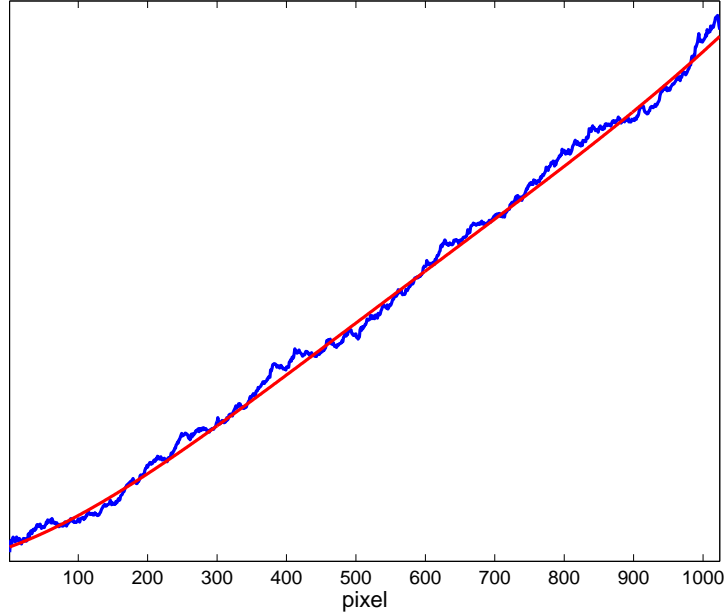


Figure 8.2: Flat field spectrum at the binning of 2 (blue) and the polynomial fit (red) used for the determination of the correction factor.

conditions as the experimental data. The uniform illumination for the flat field image is supplied by the white lamp which is coupled to the microscope.

The correction of the acquired spectra is performed according to the modified eq (8.1):

$$R_i = A_i \frac{P_i}{F_i} \quad (8.2)$$

where R , A and F have the same meaning as previously and i refers to the position on the horizontal axis of the CCD array (pixel number in the resulting spectrum). Because the flat field spectrum displays a strong intensity variation over the whole pixel range, the mean $\langle m \rangle$ of the flat field was replaced by a polynomial fit P to the flat field, as depicted in Figure 8.2. The ratio of the polynomial fit to the flat field defines a correction factor with which all measured spectra have to be multiplied. Figure 8.3 illustrates the improvement achieved by this procedure. It allows also to smooth the spectra without amplifying strange features and creating artificial peaks, as shown in Figure 8.4.

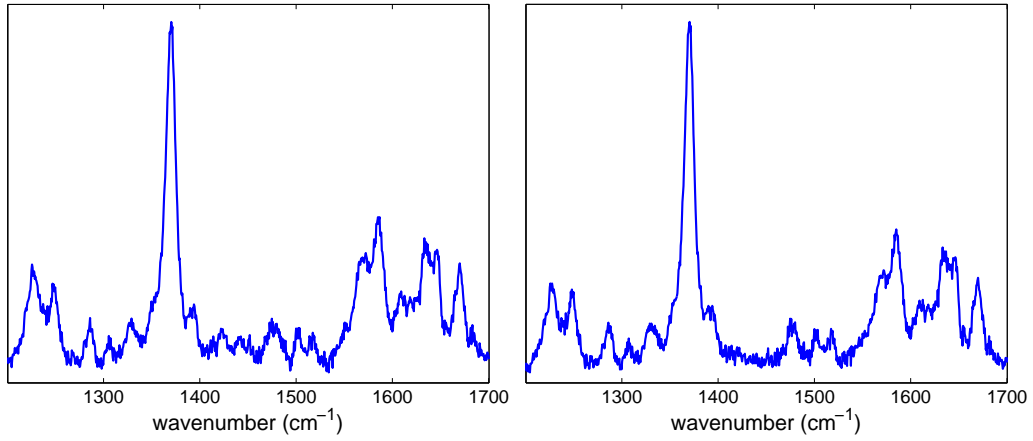


Figure 8.3: Background subtracted CcO SERR spectra before (left) and after (right) flat field correction.

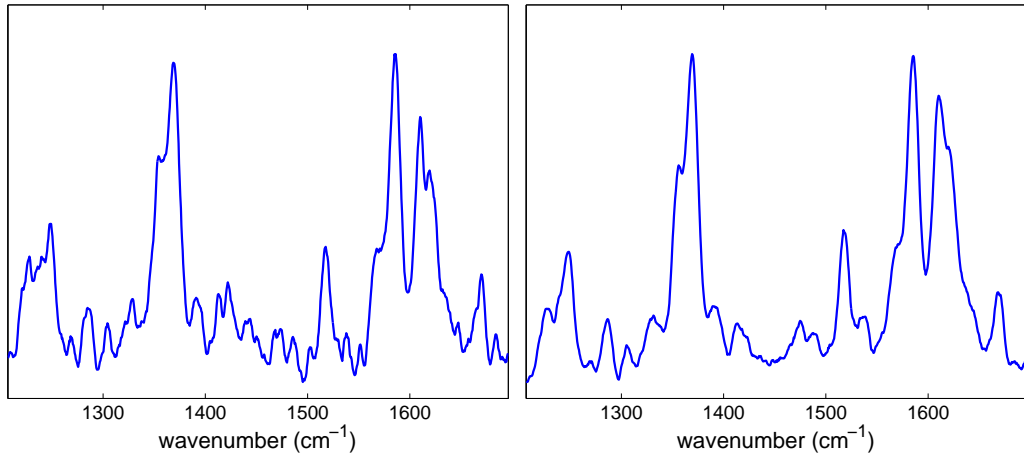


Figure 8.4: Background subtracted and smoothed CcO SERR spectra before (left) and after (right) flat field correction.

8.2 Background subtraction

Due to their high SNR, SERR spectra of Cyt *c* usually do not require any special treatment. The structureless offset was removed by subtracting a straight line from the raw data. In contrast, acquired CcO SERR spectra showed a high structured background as illustrated in Figure 8.5. The broad band at around 1600 cm^{-1} appears in the SER spectrum of an unmodified rough Ag electrode as well and was attributed to carbon impurities present on the metal surface.^{100,101,102} Polynomial background subtraction from a large number of spectra is a tedious task, and, more importantly, it is difficult to subtract consistently the same background shape for each spectrum. In the case of large series of spectra, background subtraction was therefore performed with the help of factor analysis.

Factor analysis is a multidimensional statistical method which originated at the very beginning of the 20th century in the field of psychometrics. Applications of factor analysis to various domains including social sciences or marketing have spread ever since especially thanks to a tremendous computer development. It is also one of the methods widely used in chemometrics, a branch of analytical chemistry.¹⁰³ Factor analysis enables to extract the essential information contained in a large set of data and thus can be useful in spectroscopic measurements as well.^{104,105,106,107}

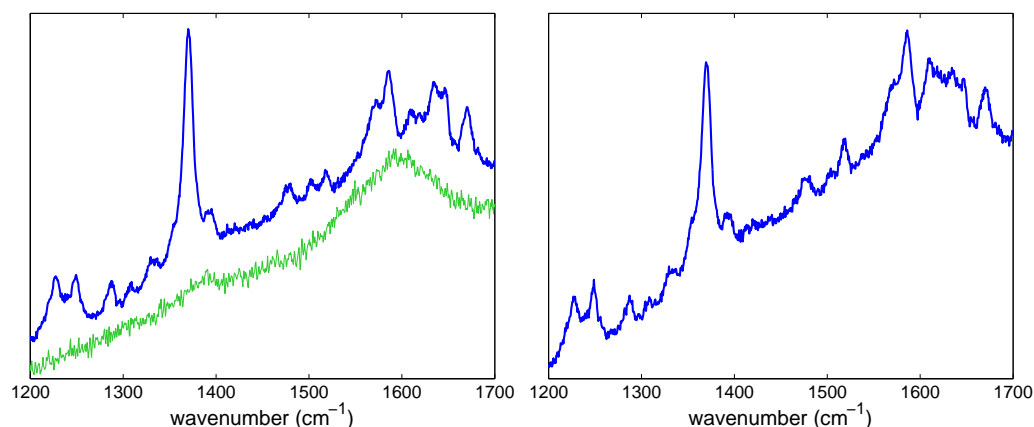


Figure 8.5: Illustration of the background shape for raw CcO SERR spectra. Accumulation time: 10 minutes (left) and 5 minutes (right). SER spectrum of an unmodified Ag electrode is displayed in the left plot in green, its intensity was adjusted to fit in the same range as CcO spectrum.

Factor analysis is based on the singular value decomposition (SVD) algorithm. An $n \times m$ matrix A can be expressed according to

$$A = USV^T \quad (8.3)$$

where U and V are $n \times n$ and $m \times m$ orthogonal matrices respectively.* S represents a diagonal matrix of the same size as A . The so called singular values S_{ii} are computed in a decreasing order. In the specific case of spectroscopic data, A contains the original spectra (m spectra with n spectral points) which have been measured as a function of a certain variable (time, potential, temperature, pH, etc.). SVD analysis yields a matrix U whose columns represent a set of orthonormal subspectra, the statistical weight of each subspectrum is expressed by the singular values S_{ii} . V consists of normalized coefficients which express the relative contribution of each subspectrum in the experimental spectrum.

Spectra in large data sets are mostly correlated and can be expressed as a linear combination of a limited number of components which can be determined by SVD. The best approximation of m experimental data by a linear combination of r subspectra ($r < m$) is namely given by

$$A \simeq US_rV_r^T \quad (8.4)$$

where the S_r and V_r stand for S and V matrices with dimensions restricted to $n \times r$ and $r \times r$ respectively. The minimum, but large enough value of r , for which the restricted combination on the right side of eq (8.4) just approximates the experimental spectra within the experimental error, represents the factor dimension of the data. The factor dimension determines the number of spectroscopically distinguishable components in the experimental data set. The determination of the factor dimension r represents thus the key point of factor analysis. It can be deduced from the succession of the decreasing singular values or from the dependence of the residual error on a tentative r value.

Subspectra with a rank higher than r do not contain any spectroscopic information. Therefore, eq (8.4) can be used as a noise-filtering tool.¹⁰⁸ Moreover, factor analysis can facilitate background subtraction since the meaningful subspectra reflect the background shape of all spectra in the data set. It is thus sufficient to define a polynomial background for the first subspectra (illustrated in Figure 8.6 for the first two subspectra of a measurement series) and perform the subtraction for the data set according to

$$A_{subtracted} = A - BS_rV_r^T \quad (8.5)$$

* V^T stands for the transpose of V , $V_{ij}^T = V_{ji}$

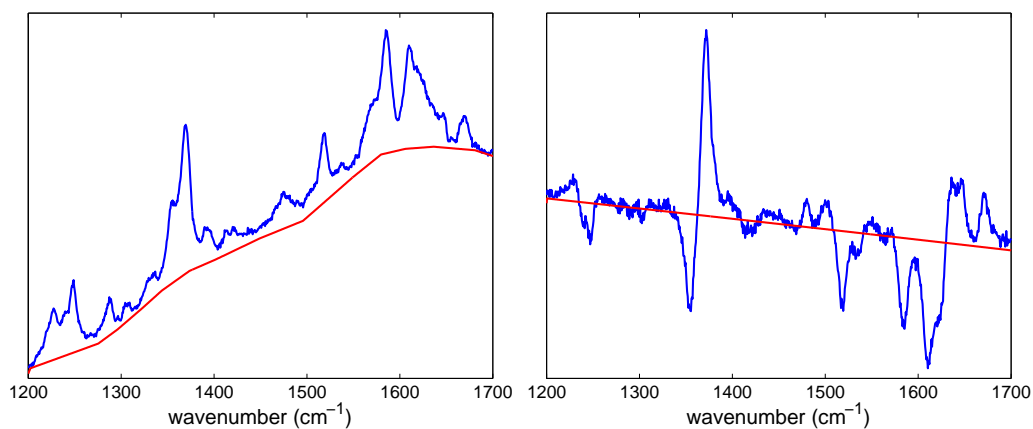


Figure 8.6: Polynomial background subtraction for the two first subspectra from factor analysis. The first subspectrum (left), which is of the highest statistical weight, represents an average spectrum of the experimental data set. The second subspectrum (right) describes the average differences between the experimental spectra and the first subspectrum.

where B stands for the background spectral shape for r first subspectra. This method presents the unique advantage of subtracting exactly the same background shape for all spectra in the data set. The resulting spectra are plotted in Figure 8.7.

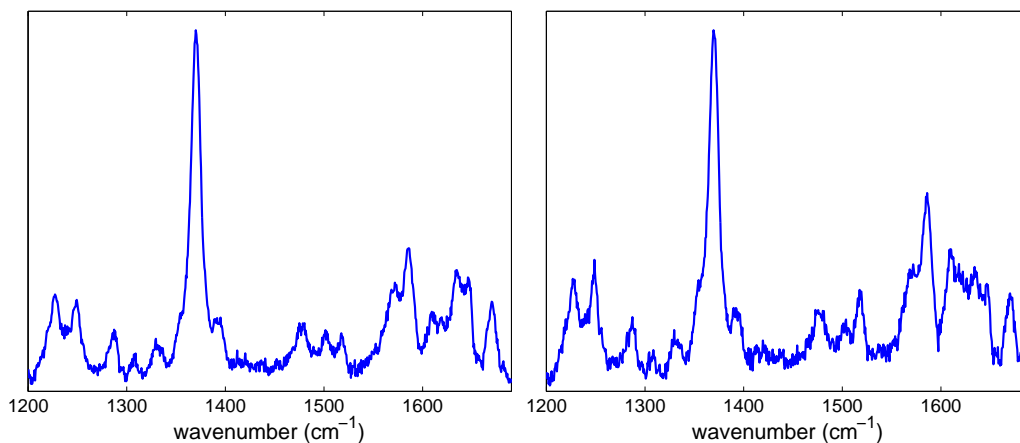


Figure 8.7: Spectra from Figure 8.5 after background subtraction with the help of factor analysis according to eq (8.5).

8.3 Component analysis

After background subtraction, Cyt *c* and CcO spectra were analyzed by component analysis.¹⁰⁹ Different spectral components which correspond to distinct protein species contribute to the acquired SERR spectra. The spectral components present in a particular spectrum can be determined for example on the basis of RR measurements under conditions favoring the occurrence of only one species or have to be determined iteratively.¹⁰⁹ Each experimental spectrum is then fitted with the relevant component spectra using only their relative contributions as adjustable parameters. Examples of component analysis for all studied systems are shown in the corresponding sections.

Component analysis results in relative intensities of the individual spectral components I_i which are related to the relative surface concentrations of the species c_i according to:

$$c_i = I_i f_i \quad (8.6)$$

where f_i is a factor proportional to the reciprocal SERR cross section of species i . Factors f_i are estimated experimentally from the RR intensity ratio of the different species measured in solution with the same concentration and under identical conditions.

All spectra treatment steps were performed in Matlab 7.1 (The Math-Works) except for the component spectra definition which was done with the help of a home-made component analysis software.

Part IV

Results and discussion

Chapter 9

Cytochrome *c* wired to metal electrodes

In a collaboration with David H. Waldeck (University of Pittsburgh), the electron transfer dynamics of Cyt *c* coordinatively bound to pyridine-terminated alkanethiols on electrodes (see Figure 6.1 for the immobilization scheme) was investigated by time-resolved surface-enhanced resonance Raman spectroelectrochemistry (Ag electrodes; Berlin) and cyclic voltammetry (Au electrodes; Pittsburgh).

9.1 Introduction

Cyt *c* acts as electron carrier in the respiratory chain and represents thus a frequently used model system to study electron transfer in proteins. Cyt *c* transfers electrons between two closely spaced enzyme complexes embedded in the mitochondrial membrane, it operates permanently at a membrane/solution interface. Different model interfaces have been therefore designed to immobilize Cyt *c* on electrodes and investigate various aspects of the heterogeneous electron transfer.^{10,11,38}

In an effort to mimic the interaction of Cyt *c* with biological membranes, most studies have been conducted on Cyt *c* attached to a carboxyl-terminated interface.^{60,110,111} Cyt *c* possesses a strong dipole moment, the exposed heme cavity is surrounded by seven lysine residues, which are positively charged at pH 7. This positive patch, which is involved in binding to Cyt *c*'s natural redox partner CcO, interacts with the anionic surface of the electrode biocompatible coating via electrostatic interactions. The dipole moment and a well defined binding domain ensure uniformity of the electrostatically immobilized Cyt *c*. Under these conditions, electron transfer between the redox

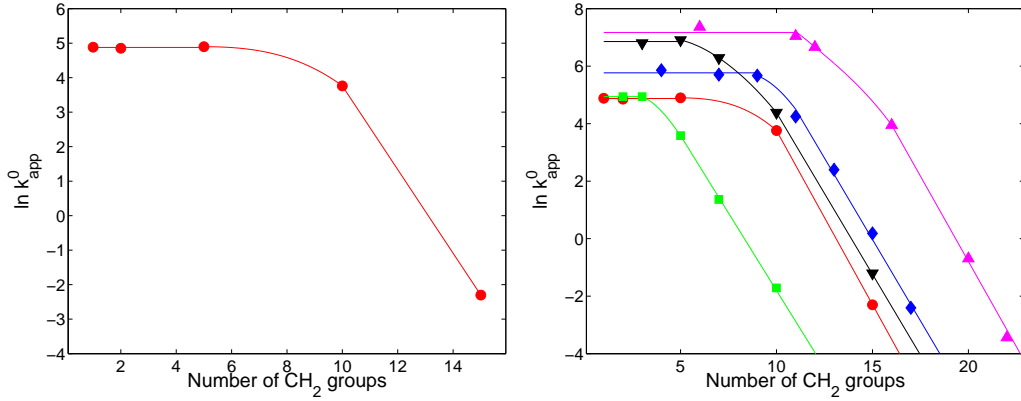


Figure 9.1: Distance dependence of the apparent standard electron transfer rate for: (a) Cyt c electrostatically adsorbed to COOH-terminated SAMs on Ag electrodes;¹¹² (b) different systems (if not noted otherwise, the data stem from Au electrodes): green squares: cytochrome c' on COOH-terminated SAMs¹¹³; red circles: Cyt c on Ag electrodes coated with COOH-terminated SAMs¹¹²; black down-triangles: Cyt c on COOH-terminated SAMs¹¹³; blue diamonds: azurin on CH_3 terminated SAMs⁵⁸ and magenta up-triangles: Cyt c coordinatively bound to pyridine-terminated SAMs⁹¹.

center and the electrode is expected to occur in the nonadiabatic regime due to the relatively large separation.

Different parameters that control the long range heterogeneous electron transfer have been investigated revealing, however, an unusual distance dependence of the apparent electron transfer rate at zero overpotential, k_{app}^0 . As depicted in Figure 9.1(a), for Cyt c adsorbed on ω -mercaptoalkanoic acids with alkyl chains of 10 or more methylene units, the electron transfer rate falls exponentially in agreement with the exponential decay of the electronic coupling in the nonadiabatic electron transfer model. Hence the variation of the rate constant can be described by

$$k_{\text{ET}} \propto \exp(-\beta(r - r_0)), \quad (9.1)$$

where r stands for the separation of the redox center from the electrode, r_0 is the van der Waals distance and β denotes the tunneling parameter. Surprisingly, the apparent electron transfer rate levels off at shorter spacer lengths and becomes distance independent.¹¹² Moreover, the observed rate decreases upon increasing viscosity.^{111,112,114}

A similar distance dependence of the electron transfer rate has been observed for other heme and non-heme proteins immobilized on different SAMs and investigated by a variety of electrochemical and spectroelectrochemical

methods. Some examples are azurin⁵⁸ and Cu_A domain of CcO on hydrophobic surfaces,¹¹⁵ cytochrome *c*₆ on mixed CH₃/OH-terminated SAMs¹¹⁶, cytochrome *b*₅₆₂ on NH₂-terminated coatings⁵⁷ and cytochrome *c*' on COOH-terminated SAMs.¹¹³ A unified plot of several data sets is shown in Figure 9.1(b). Analysis of the exponential regions of the rate-distance plots for different proteins yields a unique tunneling decay parameter of 1.1 per methylene unit independently of the system under study.

An alternative immobilization scheme consists in directly tethering the heme to the electrode surface by means of a nitrogen containing terminal group of the SAM.¹¹⁷ Most studies focused on Cyt *c* attached to mixed SAMs of pyridine-terminated alkanethiols embedded in an alkanethiol diluent of shorter chain length.^{91,117,118,119,120} The immobilization strategy was shown to be successful by STM imaging and electrochemistry. A pronounced negative shift of the standard redox potential indicated pyridine binding to the heme iron.¹¹⁷

Additional evidence for the replacement of the axial heme ligand by pyridine was brought by SERR spectroelectrochemistry.¹²¹ Cyt *c* coordinatively bound to PyC₁₁/C₁₀ modified electrodes was characterized by stationary potential-dependent SERR spectroelectrochemistry and it was shown that the immobilized protein is in equilibrium between two forms that lack the natural axial heme ligand Met 80. The dominant form corresponds to a six-coordinated low spin heme (6cLS), in which the sixth ligand is the pyridine group of the monolayer. The less populated form contains a five-coordinated high spin heme (5cHS). In this form, the protein remains attached to the mixed monolayer presumably due to hydrophobic interactions. The coordination equilibrium is potential dependent with the ferric form displaced toward the 6cLS state, reflecting the larger affinity of Fe³⁺ for pyridine as compared to Fe²⁺.

The distance dependence of the electron transfer rate for coordinatively bound Cyt *c* displays a qualitatively similar shape as that observed for electrostatic immobilization. As can be inferred from Figure 9.1(b), the transition between the exponential and the plateau region of the plot occurs however at a methylene chain length of 12 rather than 9. This shift can be rationalized in terms of a change in the dominant tunneling pathway.^{91,117} In the case of electrostatic immobilization, the electron tunnels through the methylene chain across the SAM/protein interface and through the protein to the Fe redox site.¹²⁰ In contrast, for the coordinated Cyt *c*, the electron tunnels through the methylene chain and across the pyridine ring directly to the Fe site. The same argument, i.e. a change in the tunneling pathway, was also employed to explain the shift of the rate-distance plot for cytochrome *c*' (see Figure 9.1(b)).¹¹³ Similar to the electrostatic adsorption, the electron

transfer rate for the coordinative immobilization decreases with increasing viscosity at short spacer lengths.^{91,122}

The two immobilization schemes yield thus a very similar picture concerning the distance and viscosity dependence of the Cyt *c* rate constant. The exponential decrease of the electron transfer rate at long SAMs together with its insensitivity to viscosity agrees well with the nonadiabatic long-range electron transfer model governed by electron tunneling. The near distance independence of the apparent rate at shorter distances from the electrode together with its sensitivity to viscosity can be rationalized in two different ways. First, a gated mechanism, in which the nonadiabatic electron transfer process is preceded by protein rearrangement or reorientation, can be responsible for the distance independence of the apparent electron transfer rate at short spacer lengths since nuclear rearrangement should become rate limiting at sufficiently short distances. Moreover, provided that the gating step involves some sort of nuclear motion, this mechanism accounts for the viscosity dependence of the apparent rate constant for short tethers and independence at long distances.^{10,111,123} Alternatively, the experimental data can be explained in terms of a transition from a nonadiabatic reaction at long distances, in which the rate is controlled by the tunneling probability, to a friction controlled mechanism at short distances, where the electron transfer rate is determined by overdamped relaxation processes of the solvent and protein matrix.^{91,119}

The decisive experiment which can disentangle between the two scenarios consists in measuring the driving force dependence of electron transfer rate. This has been already performed for the electrostatically immobilized Cyt *c* for which the overpotential dependence of the apparent rate constant was monitored by TR-SERR spectroscopy.^{114,124} At large spacer length (15 methylene units), the Cyt *c* reduction rate increases with increasing overpotential. The data were analyzed in terms of the Marcus-DOS theory for nonadiabatic electron transfer reactions (eq (4.26)) resulting in a reorganization energy of 0.24 V.* In contrast, for distances corresponding to the plateau region of the rate-distance plot, the measured rate of Cyt *c* reduction is independent of the overpotential suggesting that electron transfer is gated at short distances. It can be thus concluded that heterogeneous electron transfer of the electrostatically adsorbed Cyt *c* is coupled to a process which becomes rate-limiting at short separations from the electrode.

Coordination of Cyt *c* to the interface should eliminate possible large-

*The significantly lower reorganization energy for the immobilized protein as compared to Cyt *c* in solution (0.6 eV) can be explained by a lower contribution of the solvent and protein rearrangement in the adsorbed state.⁹

amplitude conformational motions of the protein and preclude thus the gating mechanism.¹¹⁹ Accordingly, the distance independence of the apparent rate at short distances was interpreted in terms of a change of the electron transfer mechanism from the nonadiabatic to the friction controlled regime, a gated mechanism could however not be ruled out.^{91,119} In collaboration with the group of D. H. Waldeck, the response of the electron transfer rate of Cyt *c* bound to pyridine-terminated SAMs to the temperature, distance and overpotential was investigated in order to elucidate the heterogeneous electron transfer mechanism at small donor-acceptor separations.

9.2 Distance and temperature dependence of the electron transfer rate constant

In the Pittsburgh group, cyclic voltammetry was employed to determine the electron transfer rate constant of Cyt *c* immobilized on PyC_{*n*}/C_{*n*-1} SAMs at zero overpotential as a function of distance from the electrode (corresponds to different *n*, *n* = 6, 11, 12 and 16) and temperature. Cyclic voltammograms (CV) were collected at scan rates increasing from 10 to 500 Vs⁻¹ for *n* ≤ 12 and from 1 to 100 Vs⁻¹ for *n* = 15. Peak currents increase linearly with the scan rate, as expected for a surface-confined redox species. Voltammetric waves are symmetric and indicative of a quasireversible electrochemical reaction. The experimentally determined formal potential, -162 mV for Cyt *c* on a PyC₆/C₅ SAM, exhibits a negative shift compared to the protein in solution characteristic for the substitution of the natural axial ligand Met-80 by the pyridine group of the SAM.

Electron transfer rates at zero overpotential (k_{ET}^0) were extracted from the scan rate dependence of the peak separation in the CVs by fitting the data to Marcus theory and correcting for the uncompensated solution resistance as described previously.^{117,125} For each SAM thickness, the temperature was varied from 2°C, slightly above the freezing point, to 40°C, before Cyt *c* starts to denature. The temperature and distance dependence of the standard rate constant for Cyt *c* on different PyC_{*n*}/C_{*n*-1} SAMs is displayed in Figure 9.2 in a three-dimensional representation. In agreement with previous measurements,^{91,119} the observed electron transfer rate constant of the pyridine-coordinated Cyt *c* shows an exponential distance dependence for long tethers (*n* ≥ 12), but remains nearly constant at thinner films.

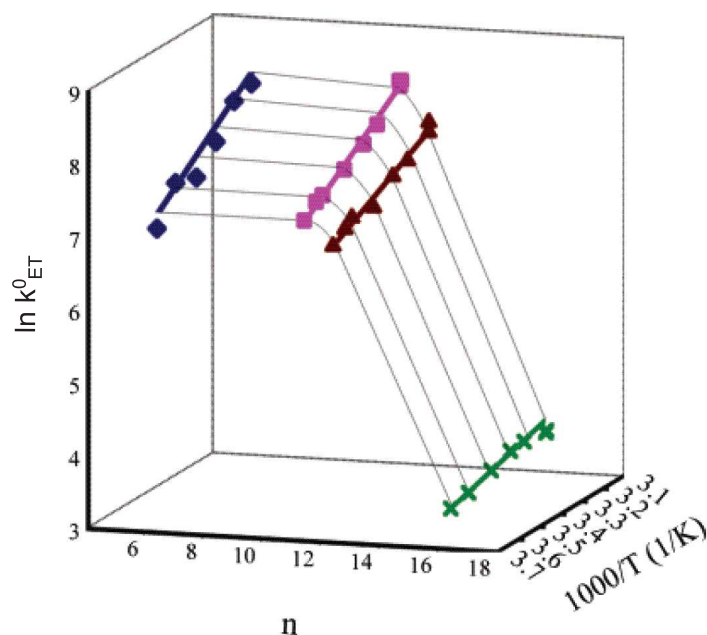


Figure 9.2: Distance and temperature dependence of the standard electron transfer rate constant for Cyt *c* on SAMs of different composition on Au. Green crosses: PyC₁₆/C₁₅, purple triangles: PyC₁₂/C₁₁, pink squares: PyC₁₁/C₁₀, blue diamonds: PyC₆/C₅.¹²⁶

9.3 Overpotential dependence of the electron transfer rate constant

In order to discriminate between the two possible explanations for the distance independance of the observed rate at small donor-acceptor separations electron transfer kinetics of Cyt *c* bound to PyC₆/C₅ coated electrodes was investigated by TR-SERR spectroscopy (see Figure 7.2 for measurement setup). Spectra were measured at variable delay times δ following potential jumps from a fixed initial potential $E_i = +0.1$ V, where Cyt *c* is predominantly in the oxidized state, to different values of the final potential E_f . This corresponds to activation overpotentials ($\eta = E_f - E^0$) ranging from 0.0 to -0.4 V for the 6cLS redox couple (see below). Potential jumps to lower final potentials ($E_f < -0.7$ V) led to a decrease of the SERR signal intensity presumably due to the reductive desorption of the SAM. Investigation of the Cyt *c* oxidation kinetics was not possible due to the relatively low oxidation potential of Ag.

Figure 9.3 shows TR-SERR spectra of coordinatively immobilized Cyt *c*

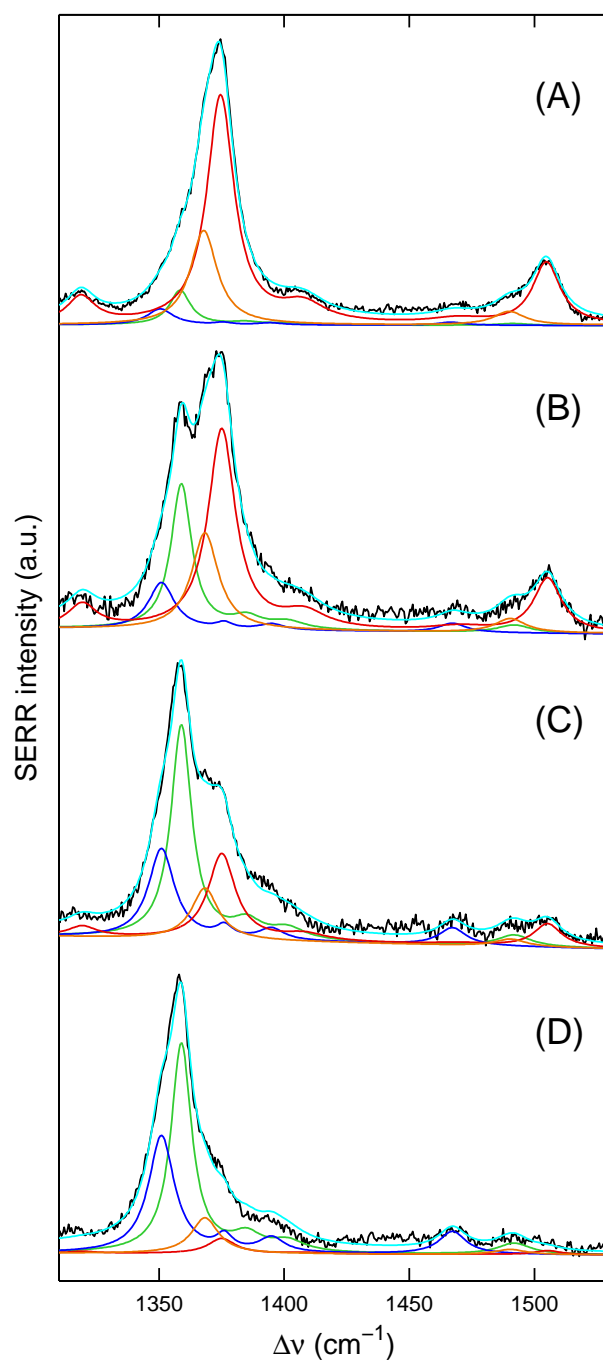


Figure 9.3: TR-SERR spectra of Cyt *c* bound to PyC₆/C₅ coated electrodes as a function of the delay time δ' for a potential jump from +0.1 V to -0.5 V: (A) $\delta' = 0$, (B) $\delta' = 165 \mu\text{s}$, (C) $\delta' = 800 \mu\text{s}$, (D) $\delta' = 11 \text{ ms}$. Black: experimental spectra, cyan: overall fit, green: 6cLS^{red}, red: 6cLS^{ox}, blue: 5cHS^{red}, orange: 5cHS^{ox}.

at different delay times δ' for a potential jump to -0.5 V. The acquired spectra were subjected to the component analysis procedure as described in Section 8.3. Accumulation of spectra with a satisfactory SNR was hampered by the SAM instability at potentials below -0.2 V inducing Cyt *c* SERR signal loss at the time scale of minutes. The SAM instability is presumably caused by irreversible structural changes in the hydrophobic phase of the mixed SAM.¹²⁷ The more complex ν_2 region of the spectra (around 1580 cm⁻¹) was negatively influenced by the pronounced background due to lower spectral quality and thus excluded from the analysis. Nevertheless, as outlined previously, the ν_3 and ν_4 represent the most prominent and well separated marker bands which enable an unambiguous determination of different species. All experimental spectra could be consistently simulated by using four spectral components, namely 6cLS^{red}, 6cLS^{ox}, 5cHS^{red} and 5cHS^{ox} species. The spectral parameters of these four components are identical to those determined previously in the stationary SERR studies¹²¹ except for the bandwidth which was decreased in agreement with the higher resolution of the present spectrometer.

Relative intensities of the four spectral contributions resulting from the component analysis are plotted in Figure 9.4 for a potential jump to -0.4 V. Ideally, relative intensities should be converted to relative concentrations of the four species using respective proportionality factors according to eq (8.6). Because the involved species cannot be prepared in a pure form, the proportionality factors cannot be determined and the quantitative analysis is thus restricted only to relative intensities. The kinetics of the four species was analyzed according to the proposed redox-coordination square equilibrium model¹²¹ (Figure 9.5) with the help of the Specfit/32TM software. Eight rate constants represent a very large set of parameters, nevertheless, consistent and satisfactory results could be obtained for the reduction rate constants of the 6cLS and 5cHS redox couples, k_1 and k_3 , respectively.

The total relative amounts of 6cLS and 5cHS species do not change within the first ca. 10 ms after a potential jump, indicating that the dynamics of the coordination equilibrium is slower than electron transfer. This observation is supported by the range of fitted values for the rates corresponding to the coordination equilibrium (k_5 , k_6 , k_7 and k_8) which are in most cases lower than 10 s⁻¹ and thus at least one order of magnitude smaller than the rates for reduction. Unfortunately, the too high uncertainty in fitting eight parameters to data like in Figure 9.4 does not allow for a more detailed discussion. Nevertheless, it is clear that the 6cLS and 5cHS species can be regarded as nearly independent redox couples. Consistent with these observations, fitting the TR-SERR data to two independent redox couples results in essentially the same reduction rate constants as the square equi-

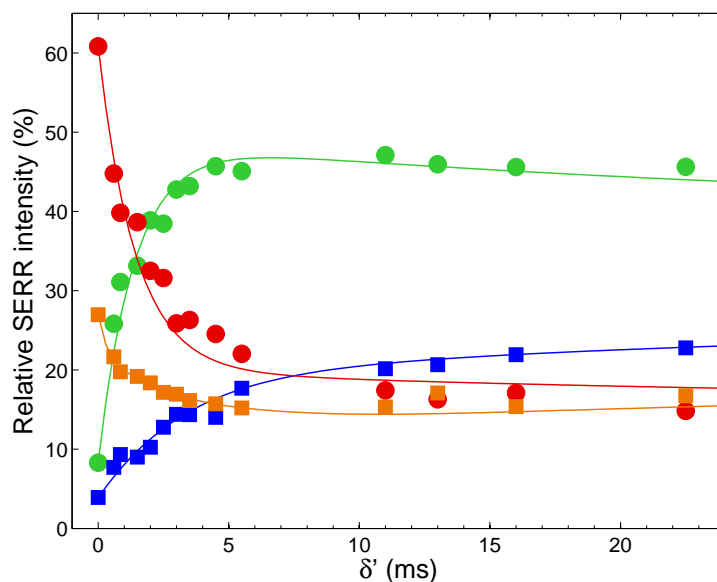


Figure 9.4: Relative intensities of the different Cyt *c* species on PyC₆/C₅ modified electrodes as a function of the delay time δ' after a potential jump from +0.1 V to -0.4 V ($\eta_{6\text{cLS}} = -0.16$ V and $\eta_{5\text{cHS}} = -0.22$ V). Green: 6cLS^{red}, red: 6cLS^{ox}, blue: 5cHS^{red}, orange: 5cHS^{ox}. The lines correspond to the fit of the data according to the redox-coordination square equilibrium scheme.

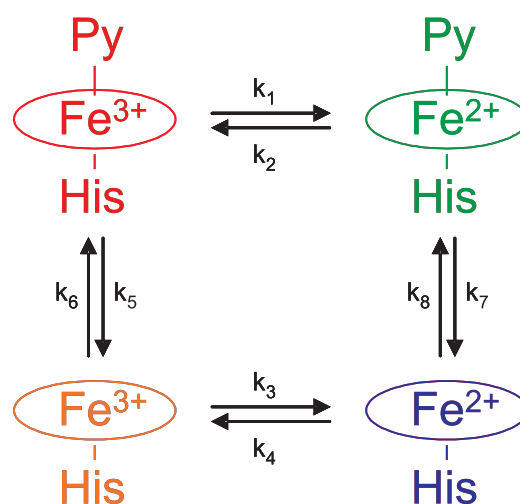


Figure 9.5: Redox-coordination square equilibrium scheme of Cyt *c* coordinated to PyC₆/C₅ coated electrodes.

librium model. The reduction rate constants for all examined overpotentials are plotted in Figure 9.6.

As explained above, SERR cross sections of the four species present in the TR-SERR spectra are not known and relative intensities instead of relative concentrations were used in the analysis of the data. This approximation does not have any impact on the determined rate constants. Assuming the simple model of two independent redox couples, the decay of the oxidized 6cLS (5cHS) form after a potential jump can be described by

$$\frac{c_\delta - c_\infty}{c_0 - c_\infty} = \exp(-(k_1 + k_2)t), \quad (9.2)$$

where c_0 , c_∞ and c_δ stand for the concentrations of the oxidized 6cLS (5cHS) species at the initial and final potential and at time δ after the potential jump, respectively. k_1 and k_2 (k_3 and k_4) have the same meaning as in Figure 9.5 and represent the rate constants for reduction and oxidation of the 6cLS (5cHS) redox couple, respectively. In eq (9.2), the concentrations can be substituted by intensities since after replacing the concentrations by eq (8.6) all terms on the left side of eq (9.2) contain the same cross section factor, i.e. that of the oxidized 6cLS (5cHS) species.

In contrast, the difference between concentration and intensity can influence the redox potential determined by SERR measurements. Previous SERR potential-dependent investigations of Cyt *c* coordinated to PyC₁₁/C₁₀ resulted in formal potentials (E^0) of -0.24 V and -0.18 V for the 6cLS and 5cHS redox couple, respectively.¹²¹ The data were analyzed in terms of relative intensities by the Nernst equation

$$E = E^0 - \frac{RT}{nF} \ln \frac{c_{\text{red}}}{c_{\text{ox}}} = E^0 - \frac{RT}{nF} \ln \frac{f_{\text{red}}}{f_{\text{ox}}} - \frac{RT}{nF} \ln \frac{I_{\text{red}}}{I_{\text{ox}}}, \quad (9.3)$$

where R is the universal gas constant, T the absolute temperature, F the Faraday constant, n stands for the number of transferred electrons, c_{red} , c_{ox} , I_{red} and I_{ox} represent the concentrations and the intensities of the reduced and oxidized 6cLS (5cHS) species and f_{red} and f_{ox} denote the relative cross sections of the reduced and oxidized form. Therefore, the redox potential determined on the basis of relative intensities will differ from the real E^0 by a factor of $\frac{RT}{nF} \ln \frac{f_{\text{red}}}{f_{\text{ox}}}$. This factor is ca. -0.03 V for native Cyt *c*, for which the cross section factors are known. The value may differ for other forms of Cyt *c*, although a change of sign is unlikely,¹²⁸ and thus it cannot account for the negative shift of the redox potential from SERR determination compared to that from cyclic voltammetry. The values of -0.24 V and -0.18 V for the 6cLS and 5cHS redox couples are in agreement with the present TR-SERR

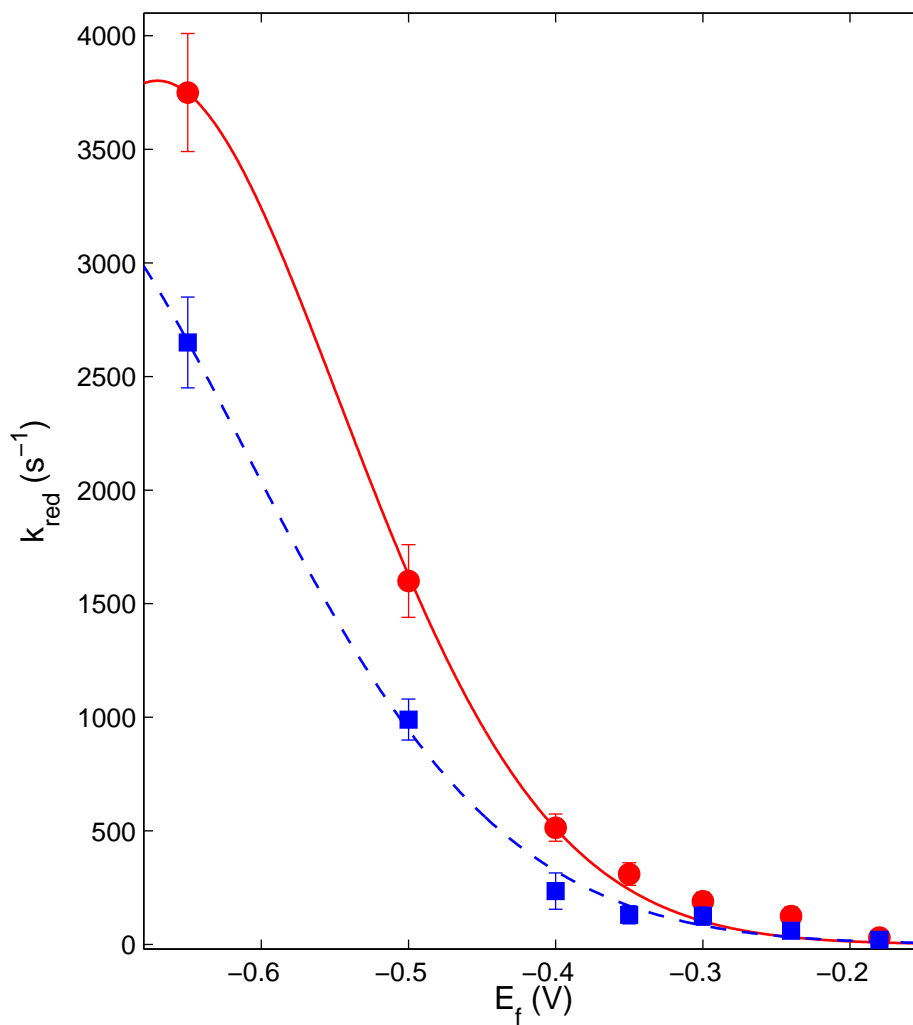


Figure 9.6: Rate constant for reduction (k_{red}) of Cyt *c* coordinatively bound to PyC₆/C₅ coated electrodes as a function of the final potential E_f in the TR-SERR experiments. Red circles: 6cLS redox couple and blue squares: 5cHS redox couple. The lines represent the best fit to eq (4.34). The error bars at potentials above -0.4 V are identical with the size of the symbols.

results and were further used in the quantitative analysis even if they are marked by a substantial uncertainty.

The dependence of the rate constant on the driving force enables to elucidate the electron transfer mechanism at short distances from the electrode. For the gated mechanism, the rate constant should not depend on the overpotential, because it is limited by a nuclear rearrangement rather than electron transfer, whereas in the case of the friction controlled mechanism the rate should change with overpotential (see eq (4.34)). As shown in Figure 9.6, the rate constant for Cyt *c* reduction readily increases with increasing overpotential both for the 6cLS and 5cHS species. The TR-SERR overpotential measurements provide thus a clear evidence for a friction controlled electron transfer mechanism for Cyt *c* adsorbed to a short PyC₆/C₅ SAM, which is well in the region where the observed electron transfer rate is distance-independent (see Figure 9.2).

The overpotential dependence of the reduction rate constant for the pyridine-coordinated Cyt *c* (6cLS) (k_1) can be satisfactorily approximated by the friction model developed by Zusman (eq (4.34)) yielding a reorganization energy $\lambda = 0.58 \pm 0.03$ eV. The error was estimated from various fits within the error bars of the rate constants plotted in Figure 9.6 which were in turn assessed from at least four TR-SERR measurements for a given overpotential. The real error is larger, approx. ± 0.1 eV, due to the above discussed uncertainty of the redox potential. The fitted value of λ falls within the range expected for a heme protein³⁸ and shows an excellent agreement with the value reported for Cyt *c* attached to a PyC₂₀/C₁₉ modified Au electrode,¹²⁰ well in the nonadiabatic regime. Therefore it can be concluded that the electron transfer rate of Cyt *c* coordinatively bound to short PyC_{*n*}/C_{*n*-1} SAMs is not limited by a major gating step but by frictional effects related to polarization relaxation processes of the solvent and/or protein matrix.

A similar analysis for the 5cHS form of Cyt *c*, which is not detected in CV experiments on Au electrodes, results in a reorganization energy $\lambda_{5cHS} = 0.7 \pm 0.1$ eV. The relatively large error comprises the uncertainty of the redox potential. The reorganization energy of the 5cHS redox couple is thus estimated to be ca. 10-30 % larger than that of the 6cLS form. This relatively small variation can be understood under the condition that the adsorbed protein does not undergo a major conformational rearrangement upon removal of the sixth axial ligand. The contribution of the inner sphere protein modes to the total reorganization energy is namely estimated to 10-50 % by different theoretical models.^{129,130}

Fitting the overpotential dependent data to eq (4.34) provides also an estimation for the relaxation time τ_S . For both the 6cLS and 5cHS redox couple, the analysis yields $\tau_S = 500 \pm 200 \mu s$. The value of the relaxation

time is more sensitive to the errors of the individual rate constants and to the uncertainty associated with the redox potential as compared to the reorganization energy, nevertheless, it remains always within the time range of hundreds of microseconds.

9.4 Discussion

The pronounced overpotential dependence of the reduction rate constant of Cyt *c* attached to PyC₆/C₅ modified Ag electrodes observed in the spectroelectrochemical investigations provides a clear evidence for the friction controlled mechanism of electron transfer at short distances. This finding allowed us to analyze the electrochemical distance and temperature dependent data for Cyt *c* coordinated to PyC_{*n*}/C_{*n*-1} SAMs on Au electrodes accordingly. The measured rate constants correspond to a pure electron transfer process, the variation of the electron transfer rate constant at zero driving force (k_{ET}^0) with temperature can be thus used to determine the reorganization energy of Cyt *c*. Fitting the temperature dependence of k_{ET}^0 to the friction controlled model for $n \leq 12$ (eq (4.35)) and to the nonadiabatic model for $n = 16$ (eq (4.26)) yields reorganization energy values λ_C decreasing from 0.84 to 0.38 eV as the length of the SAM increases (see Table 9.1 and Figure 9.7).

Such variation of λ_C clearly contradicts the theoretical predictions based on the dielectric continuum model. Indeed, because of image charge effects, the outer-sphere reorganization energy is expected to decrease with decreasing distance between the electrode and the redox moiety, as anticipated first by Marcus for systems involving a metal electrode and solvent⁸⁰ and later on extended to systems containing a metal electrode, a film and solvent.¹³¹ A qualitatively different behavior, i.e. an increase of the reorganization energy with decreasing the distance of the reactant from the electrode, was however predicted by a theoretical model based on nonlocal electrostatic treatment involving solvent spatial correlations.¹³²

The electron transfer mechanism at short donor-acceptor separations is governed by frictional coupling between the changing charge distribution of the reactants and the polarization of the surrounding medium, this coupling is described by the relaxation time of medium polarization τ_S . The calculation of the reorganization energy was performed under the assumption that τ_S is temperature independent, which is certainly not the case. Therefore a simple phenomenological approach was employed in order to account for the influence of the temperature on the friction controlled electron transfer reaction.

Table 9.1: Reorganization energies λ_C and λ and viscosity parameter γ for Cyt *c* attached to PyC_{*n*}/C_{*n*-1} coated Au electrodes.

SAM	λ_C (eV)	γ	λ (eV)
PyC ₆ /C ₅	0.84	0.58	0.48
PyC ₁₁ /C ₁₀	0.76	0.36	0.56
PyC ₁₂ /C ₁₁	0.56	0.22	0.44
PyC ₁₆ /C ₁₅	0.38	0	0.38

In line with the commonly used dielectric continuum approximation, the relaxation time τ_S was expressed as the longitudinal relaxation time, τ_L . The solvent relaxation was approximated by the simple Debye model for an ideal, noninteracting population of dipoles with a single relaxation time. Although pure water exhibits at least two characteristic relaxation times, it is reasonable to consider only the slower one which makes the largest contribution to the dielectric loss.^{86,133} The Debye dielectric relaxation is usually described by the complex permittivity $\hat{\epsilon}$ of the medium as a function of the field's frequency ω ¹³⁴

$$\hat{\epsilon}(\omega) = \epsilon_\infty + \frac{\epsilon_S - \epsilon_\infty}{1 - i\omega\tau_D}, \quad (9.4)$$

where ϵ_S stands for the solvent static dielectric constant, ϵ_∞ represents the solvent dielectric constant at the high frequency limit and τ_D denotes the Debye microscopic relaxation time. In this model, the longitudinal relaxation time is proportional to the solvent shear viscosity ξ^\dagger ^{85,86}

$$\tau_S \approx \tau_L = \frac{\epsilon_\infty}{\epsilon_S} \tau_D = \frac{\epsilon_\infty}{\epsilon_S} \frac{3\xi V_m}{RT}, \quad (9.5)$$

where V_m denotes the solution molar volume.

Replacing τ_S in eq (4.35) by the expression in eq (9.5) and neglecting the logarithmic term, which is not expected to vary significantly, the frictional model predicts a linear relationship between the standard electron transfer rate and the reciprocal solvent viscosity, $k_{ET}^0 \propto \xi^{-1}$. This relationship was called dynamical solvent effect.⁸⁶ A full solvent/protein coupling is however not observed in experimental studies. Frequently, a different power law is found to characterize the viscosity dependence of the rate constant

$$k_{ET}^0 \propto \xi^{-\gamma}, \quad (9.6)$$

[†]Viscosity is denoted ξ within this work to avoid confusion with the activation overpotential η .

in which γ is an empirical parameter that varies within the range $0 < \gamma \leq 1$ and describes an intermediate friction regime.^{91,135} The parameters γ for the different SAMs were obtained by measuring k_{ET}^0 as a function of solvent viscosity, which is varied by additions of sucrose to the electrolyte solution, and are listed in Table 9.1.

The temperature dependence of the solvent viscosity was further expressed through Andrade's empirical equation

$$\xi = A \exp \left(\frac{\Delta G_{\xi}^{\ddagger}}{RT} \right), \quad (9.7)$$

in which A is an empirical parameter for the solution and $\Delta G_{\xi}^{\ddagger}$ is the activation free energy for viscous flow. The value for pure water $\Delta G_{\xi}^{\ddagger} = 17.48 \text{ kJ.mol}^{-1}$ can be reasonably adopted for diluted solutions.¹³⁶ Inserting eq (9.5), (9.6) and (9.7) into eq (4.35) the electron transfer rate constant at zero driving force can be rewritten as

$$k_{\text{ET}}^0 = \frac{\epsilon_S}{3AV_m\epsilon_{\infty}} \sqrt{\frac{RT}{4\pi\lambda}} \exp \left(-\frac{\Delta G^{\ddagger} + \gamma\Delta G_{\xi}^{\ddagger}}{RT} \right). \quad (9.8)$$

Hence, the activation Gibbs free energy extracted from temperature dependence measurements contains two contributions: a term arising from the intrinsic reorganization energy of the system, $\Delta G^{\ddagger} = \frac{\lambda}{4}$; and a term $\gamma\Delta G_{\xi}^{\ddagger}$, which accounts for the temperature dependence of the relaxation dynamics of the medium.

Correcting the experimentally determined Gibbs activation energies for the friction contribution yields a consistent data set of reorganization energies that does not exhibit a distance dependence, despite the experimental scattering; as listed in Table 9.1 and depicted in Figure 9.7. This result is considered as a reasonable one in view of the contradictory theoretical predictions mentioned above. Moreover, the λ values determined in this way are in a reasonable agreement with the overpotential determinations for PyC₆/C₅ (TR-SERR) and PyC₂₀/C₁₉ (CV¹²⁰). The above described treatment provides thus a satisfactory agreement between the different methods, even if the validity of the relatively crude assumptions, i.e. Debye-type relaxation of the solvent, solvent considered as a diluted aqueous solution, is likely to be limited at the SAM/protein interface. As illustrated in Figure 9.7, a common plot of the reorganization energy values points to an average value of $0.5 \pm 0.1 \text{ eV}$.

Zusman model of the friction controlled electron transfer also yielded a relaxation time of the medium for Cyt *c* adsorbed to the PyC₆/C₅ coated

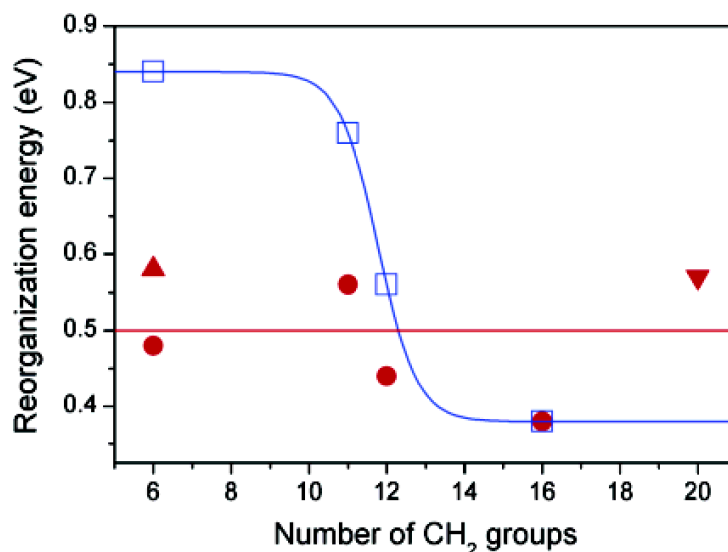


Figure 9.7: Reorganization energy λ of Cyt *c* coordinatively bound to PyC_{*n*}/C_{*n-1*} SAMs as a function of the chain length *n*. Blue squares: λ_C determined by CV from the temperature dependence of k_{ET}^0 using eq (4.35). Red circles: λ determined by CV from the temperature dependence of k_{ET}^0 using eq (9.8) (except *n* = 16 that is treated as nonadiabatic). Red up triangle: λ determined by TR-SERR from the overpotential dependence of k_{ET} . Red down triangle: λ determined by fitting the voltammetric peak separation vs. scan rate to the nonadiabatic model.¹²⁰ The lines are included to guide the eye. All data refer to Au electrodes except for the red up triangle that was determined on Ag.

Ag electrodes. The theory was originally developed for solvent relaxation, however protein interior and protein/SAM interface contribute to the relaxation processes related to heterogeneous electron transfer of biomolecules as well. Indeed, the characteristic relaxation time was found to be in the time scale of hundreds of microseconds, which is extremely long for a pure solvent response. Pure water displays relaxation times on the picosecond time scale. Longitudinal relaxation times in the order of picoseconds were observed for heterogeneous electron transfer of a hexacyanoferrate redox system in aqueous solution¹³⁷ or for a metallocene redox couple in various organic solvents.¹³⁸ A protein, however, provides a highly structured solvation environment and its polarization relaxation can be expected to be slower than that of an ordinary solvent. Protein relaxation on the time scale of hundreds of nanoseconds was estimated for Cyt *c* coordinatively bound to PyC₆/C₅ on Au electrodes,⁹¹ in agreement with values typical for the interior of a glob-

ular protein.¹³⁹ This value is still ca. 3 orders of magnitude faster than the relaxation time observed for the same system on Ag electrodes.

Two other major differences were observed between experiments on Ag and Au electrodes. First the standard electron transfer rate constant k_{ET}^0 for the pyridine-coordinated redox couple is ca. 15 times lower on Ag (150 s^{-1}) compared to Au (2500 s^{-1}) and, second, only the 6cLS Cyt *c* species is detected on Au whereas there is an important population of the 5cHS Cyt *c* form on Ag electrodes. A similar discrepancy in the k_{ET}^0 values between Ag and Au is observed also for Cyt *c* electrostatically adsorbed to carboxylic acid-terminated SAMs. The electron transfer rates are essentially the same in the tunneling regime at long spacer lengths, whereas roughly 10 times slower rates are determined on Ag compared to Au at short chainlengths, i.e. in the plateau region of the k_{ET}^0 distance dependence (see Figure 9.1).^{112,140} This behavior cannot be ascribed to the difference of the densities of states at the Fermi level for the two metals since it is relatively small ($\rho_f = 0.29/\text{atom}/\text{eV}$ for Au and $\rho_f = 0.26/\text{atom}/\text{eV}$ for Ag)¹⁴¹ and moreover was shown not to have a big impact on the nonadiabatic reaction rate.^{81,142} In the adiabatic regime, the electron transfer rate is independent of ρ_f .

Nevertheless, as described in Section 3.3, the magnitude of the electric field strength at the SAM/protein interface depends on the charge density at the metal surface, that is, on the difference between the actual potential and the potential of zero charge of the electrode, E_{pzc} (see eq (3.4) and (3.5)). The values of E_{pzc} for the two metals are very different, namely -1 V for polycrystalline Ag¹⁴³ and 0 V for polycrystalline Au¹⁴⁴ (vs. Ag/AgCl sat. KCl). Therefore, at the standard potential for coordinatively bound Cyt *c*, the difference between E^0 and E_{pzc} is ca. four times larger for Ag than for Au. The larger electric field at the Ag interface is likely to retard solvent and protein relaxation dynamics, slowing the electron transfer rate in the friction controlled regime. An electric field induced increase of the relaxation time τ_S on Ag with respect to Au can thus be expected as well.

The stronger electric field on Ag surfaces may also explain the relatively large population of 5cHS species on this metal. Ligand exchange reactions of Cyt *c* have been shown to be strongly dependent on the applied electric field strength.^{10,11,145} Cyt *c* can undergo conformational transitions between the native B1 form and the nonnative B2 states, which are characterized by the loss of the Met-80 axial ligand of the heme group. The sixth coordination site may either remain vacant, yielding a 5cHS species, or be occupied by a histidine residue, resulting in a bis-histidine coordinated heme (6cLS form).¹⁴⁶ A correlation between the amount of B2 species and the electric field strength could be established for Cyt *c* attached to differently coated Ag electrodes pointing to a shift of the conformational equilibrium towards

B2 states with increasing electric field.^{10,11} Furthermore, a significant electric field dependence of the dissociation energies for different ligands in porphyrin model systems has recently been predicted based on DFT calculations.¹⁴⁵

9.5 Summary

The overpotential, temperature, distance and viscosity dependencies of the electron transfer rate of Cyt *c* immobilized on PyC_{*n*}/C_{*n*-1} SAMs give a uniform picture consistent with a nonadiabatic reaction at long distances and an increasingly solvent/protein friction controlled mechanism for thinner films. Zusman formulation was successfully employed to describe the effect of friction on electron transfer. Despite its simplicity, the theory provides a consistent qualitative picture. The underlying assumption of a single relaxation time could contribute to the extremely high value of τ_S as presumably a manifold of relaxation processes take place at the SAM/protein interface. The change of mechanism is linked to the increase in the electronic coupling and to the slowing of the polarization relaxation with decreasing SAM thickness. The overpotential dependence of the rate constant at short distances discounts conformational gating as the rate limiting step. In contrast, the apparent rate constant on short carboxylic acid-terminated SAMs shows no variation with increasing driving force,^{114,124} what can be regarded as a typical signature of a gated mechanism.

Chapter 10

Cytochrome *c*-polyelectrolyte layer assemblies

10.1 Introduction

Protein immobilization on biocompatible electrodes represents an ideal approach to study electron transfer reactions, as illustrated in the previous section, but it also constitutes a promising approach for the design of bio-electronic devices like biosensors and biofuel cells. For example, Cyt *c* electrostatically attached to carboxylate-terminated SAMs is a simple system that can be used for detection and quantification of superoxide radicals.¹⁴⁷ It was shown that superoxide reduces the immobilized protein which can be in turn reoxidized by applying an appropriate potential giving rise to a current that is proportional to the radical concentration. The sensitivity of this simple sensor increases with the amount of adsorbed protein. In order to improve the detection parameters of this system it is thus necessary to construct stable multilayers of the electroactive protein. Such multilayers were successfully prepared by the layer-by-layer deposition of heme proteins and electrolytes.¹⁴⁸ However, inefficient electronic communication of the upper protein layers has restricted the applicability of the method to only 2-5 layers.^{149,150,151}

More recently, it was shown that alternating layer-by-layer deposition of Cyt *c* and poly(aniline sulfonic acid) (PASA) leads to a nearly linear increase of the current generated by superoxide with the number of deposited adlayers.¹⁵² The multilayer formation was further confirmed by electrochemical quartz crystal microbalance (QCM) studies.¹⁵³ The assembly displays a roughly 4 times higher sensitivity towards superoxide than a Cyt *c* monolayer electrode.¹⁵⁴

The nearly linear increase in the amount of the redox active protein was observed up to 15 adsorbed layers, raising questions about the mechanism of this long range electron transfer.¹⁵² Exchanging Cyt *c* in the inner layers with the redox inactive apo-cytochrome *c* (Apo) led to effective blocking of electron transfer only if the number of Apo layers was large enough (8 or more inner layers in a 12 layer assembly).^{152,153} It was concluded from these experiments that electron transfer in the multilayer assemblies proceeds via protein-protein electron exchange between face-to-face oriented Cyt *c* molecules. This mechanism requires a certain degree of rotational flexibility of the Cyt *c* molecules provided by the weak PASA polyelectrolyte matrix in which they are embedded.^{152,153,154} However, a contribution of the polyelectrolyte to electron transfer could not unambiguously be ruled out. Moreover, PASA is a derivative of polyaniline and is well-known for its conductive properties.^{155,156,157,158}

The present section focuses on structural and mechanistic aspects of the PASA-Cyt *c* assembly adsorbed to a mixed COOH/OH terminated SAM investigated by stationary and TR-SERR spectroelectrochemistry, which has been previously employed to study Cyt *c*-polyelectrolyte electrodes of a different type.¹⁵⁹ Special stress is laid on elucidating the electron transfer mechanism within the PASA-Cyt *c* layer.

10.2 Electrostatically adsorbed Cyt *c*

Cyt *c* electrostatically immobilized on MUA/MU SAMs on Ag electrodes (Ag-MUA/MU-Cyt *c*) served as a cornerstone for the multilayer assembly and was thus studied first to be used as a reference for the subsequent measurements. The redox equilibrium was investigated in the potential-dependent stationary mode and the dynamics of electron transfer in the time-resolved mode of SERR spectroscopy. The spectroelectrochemical measurements were supplemented by CV acquisitions.

10.2.1 Redox equilibrium

SERR spectra of the Ag-MUA/MU-Cyt *c* coated electrodes, when measured at potentials sufficiently negative or positive with respect to the formal potential E^0 , were almost identical to the resonance Raman spectra of the ferrous and ferric forms of Cyt *c* in solution. Minor variations in band intensities can be identified only in the ν_2 region of reduced Cyt *c*. This deviation can be explained by different enhancement of modes originating from the largely uniformly oriented heme groups in the immobilized protein and from the

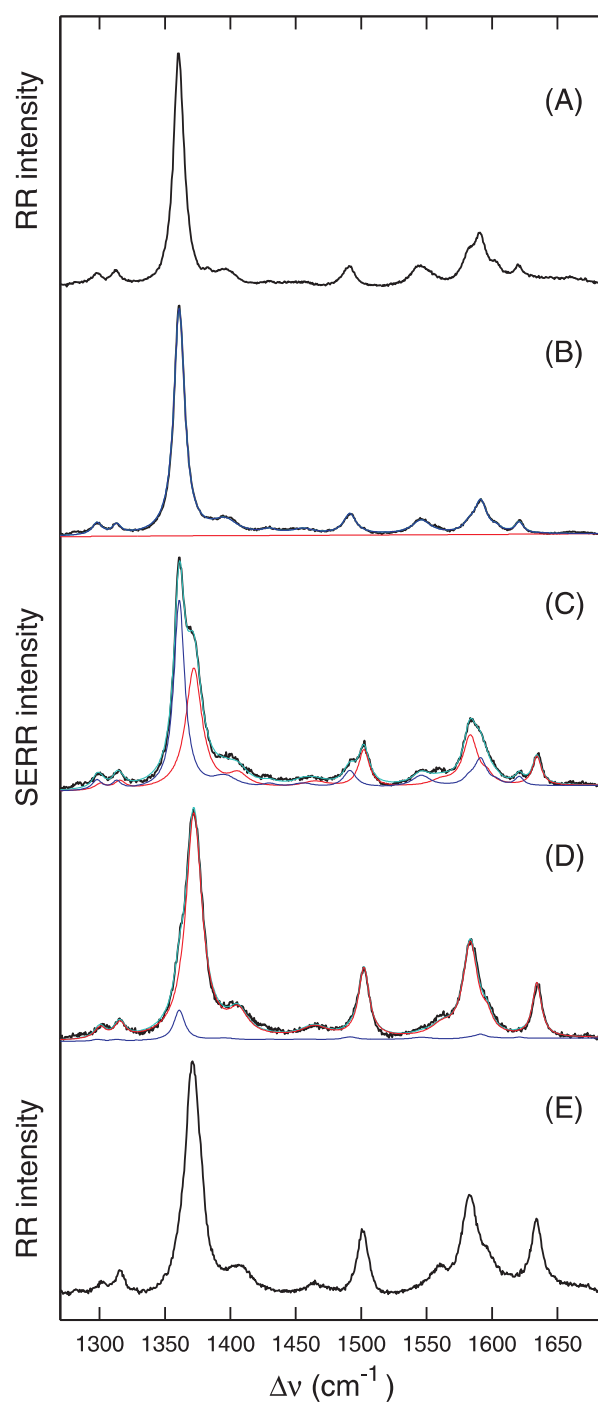


Figure 10.1: Measured SERR spectra and component analysis of the Ag-MUA/MU-Cyt *c* electrodes at three different potentials: (B) -0.2 V, (C) +0.04 V and (D) +0.14 V; compared to the RR spectra of Cyt *c* in solution in the: (A) fully reduced and (E) fully oxidized form. Black: experimental spectra, cyan: overall fit, red: Cyt *c* oxidized, blue: Cyt *c* reduced.

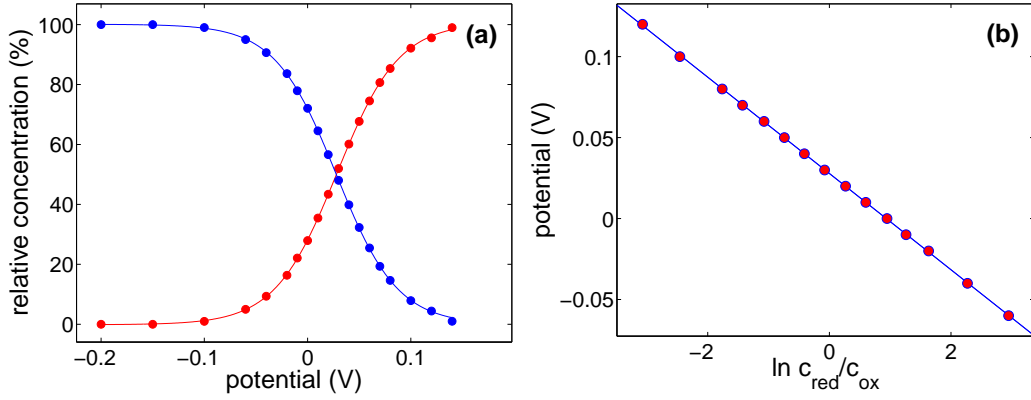


Figure 10.2: Results of potential-dependent measurements for a Ag-MUA/MU-Cyt *c* electrode: (a) concentration profile (red: Cyt *c* oxidized, blue: Cyt *c* reduced) and (b) the corresponding Nernst plot.

isotropic sample in solution. As illustrated in Figure 10.1, a series of SERR spectra measured at variable potentials from -0.2 V to +0.14 V could be consistently fitted with only two spectral components corresponding to the RR spectra of ferrous and ferric Cyt *c*, using only their relative contributions as adjustable parameters.

The SERR relative intensities of the individual spectral components I_i are proportional to the relative surface concentrations of the species c_i according to eq (8.6). The proportionality factors for Cyt *c*, $f_{\text{red}} = 0.28$ and $f_{\text{ox}} = 1.00$, were estimated from the relative RR intensities of the fully reduced and fully oxidized Cyt *c* measured in solution under identical conditions. The Nernst equation can be then written as

$$E = E^0 - \frac{RT}{nF} \ln \frac{f_{\text{red}} I_{\text{red}}}{f_{\text{ox}} I_{\text{ox}}}, \quad (10.1)$$

in which E denotes the potential poised at the working electrode, E^0 stands for the standard potential of the redox couple, R is the universal gas constant, T the absolute temperature, F the Farady constant and n represents the number of transferred electrons.

As shown in Figure 10.2 on one example, this procedure yields a nearly ideal Nernst plot for a one electron process. SERR measurements performed on 8 distinct Ag-MUA/MU-Cyt *c* electrodes result in an average value of $E^0 = 20 \pm 8$ mV and $n = 0.9 \pm 0.1$.

Cyclic voltammograms were acquired from the same electrodes, an example is plotted in Figure 10.3. Redox potentials were obtained from the

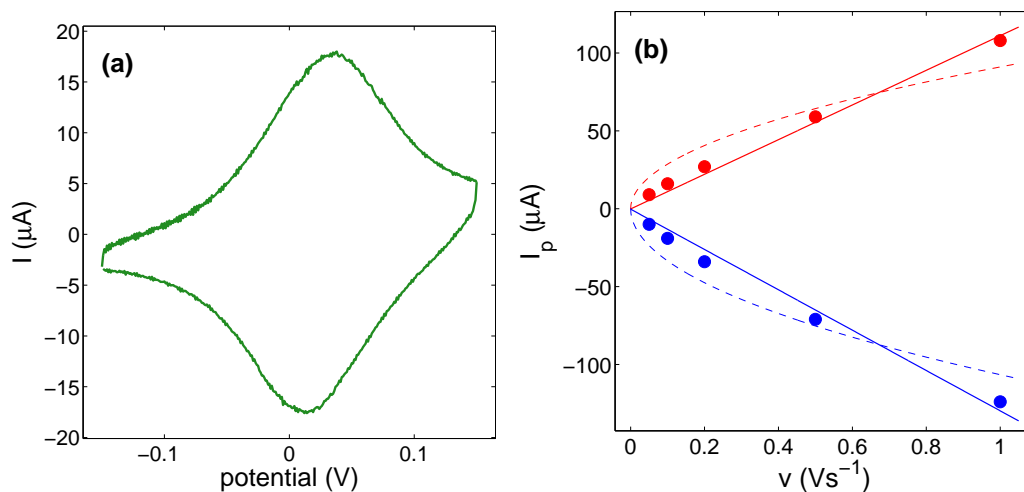


Figure 10.3: (a) Cyclic voltammogram of the electrostatically adsorbed Cyt *c* (Ag-MUA/MU-Cyt *c* electrode) at a scan rate of 0.1 Vs^{-1} . (b) CV anodic (red) and cathodic (blue) peak currents as a function of scan rate (average values from 5 different preparations, errorbars are not shown since they are smaller than the symbols). The solid lines represent a linear fit to $I_p \propto v$, the dashed lines illustrate a fit to $I_p \propto \sqrt{v}$.

anodic and cathodic peak potentials, E_{pa} and E_{pc} , respectively

$$E^0 = \frac{E_{pa} + E_{pc}}{2}. \quad (10.2)$$

CV scans of the Ag-MUA/MU-Cyt *c* electrodes yield $E^0 = 19 \pm 8 \text{ mV}$ which is in a very good agreement with the spectroscopic determination.

The determined redox potential is within the experimental error identical to that measured by CV on the same system,^{147,152} and very close to that obtained by SERR spectroelectrochemistry for Cyt *c* immobilized on a pure MUA SAM.⁶⁴ The ca. 30 mV downshift of the redox potential with respect to Cyt *c* in solution can be rationalized in terms of the potential drop at the electrode/SAM/redox center interface as described in Section 3.3.⁶⁴

Additional information on the interfacial electron transfer process can be extracted from the dependence of the peak current on the scan rate. I_p varies linearly with v in the case of immobilized electroactive species whereas I_p is proportional to \sqrt{v} in a diffusion-controlled process. Anodic and cathodic peak currents as a function of scan rate between 0.05 and 1.0 Vs^{-1} are plotted in Figure 10.3(b). The potential range which can be examined on Ag electrodes is limited in the positive direction by the oxidation of Ag. In order to obtain a well defined anodic peak, only scan rates up to ca. 1 Vs^{-1} could

be applied. As can be inferred from Figure 10.3(b), a diffusion-controlled mechanism can be unambiguously ruled out, fitting the data to $I_p \propto v$ yields very good results, the species under study are well surface-confined.

The surface concentration of the electroactive species (Γ) can be calculated on the basis of CV scans according to

$$\Gamma = \frac{Q}{nFA}, \quad (10.3)$$

where Q stands for the average charge of the integrated anodic and cathodic wave, n represents the number of transferred electrons, F is the Faraday constant and A denotes the effective electrode surface, i.e. the geometric area corrected for surface roughness. The surface roughness factor has not yet been determined for the Ag electrodes used in our laboratory. A roughness factor of 8 was estimated for rough Ag electrodes prepared in a similar way as ours by a group working with SERR spectroscopy as well.¹⁶⁰ Roughness factors of 5–8 were obtained for electrochemically roughened palladium electrodes optimized for SER investigations.¹⁶¹ Ag-MUA/MU-Cyt *c* electrodes yield an average charge of 15 μC . Using eq (10.3) with a surface roughness factor of 8 results in a surface protein coverage of 30 pmol.cm^{-2} . The calculated theoretical maximum coverage of Cyt *c* is 15 pmol.cm^{-2} ,³⁸ a slightly larger experimental value was reported for Cyt *c* electrostatically attached to MUA (17 pmol.cm^{-2}).¹⁶² The roughness factor of 8 is likely to be underestimated for the present system, the obtained value points nevertheless to a high protein coverage on the MUA/MU SAM. This conclusion is corroborated by the excellent signal-to-noise ratio of the SERR spectra.

To summarize, potential-dependent SERR spectra of the electrostatically adsorbed Cyt *c* consist of two spectral contributions almost identical to the RR spectra of the ferrous and ferric form of Cyt *c* in solution. Hence it can be concluded that the immobilized protein retains the native structure, at least at the level of the heme pocket. Moreover, the adsorbed protein exhibits a quasi ideal electrochemical behavior.

10.2.2 Electron transfer dynamics

Electron transfer dynamics of the electrostatically adsorbed Cyt *c* after a potential jump was followed by TR-SERR measurements, as schematized in Figure 7.2. The initial potential (E_i) was set to ca. -80 mV, which is sufficiently negative with respect to the standard potential so that Cyt *c* is predominantly in the reduced state. Potential jumps of variable duration were performed to the Cyt *c* redox potential ($E_f = E^0$) and to the potential

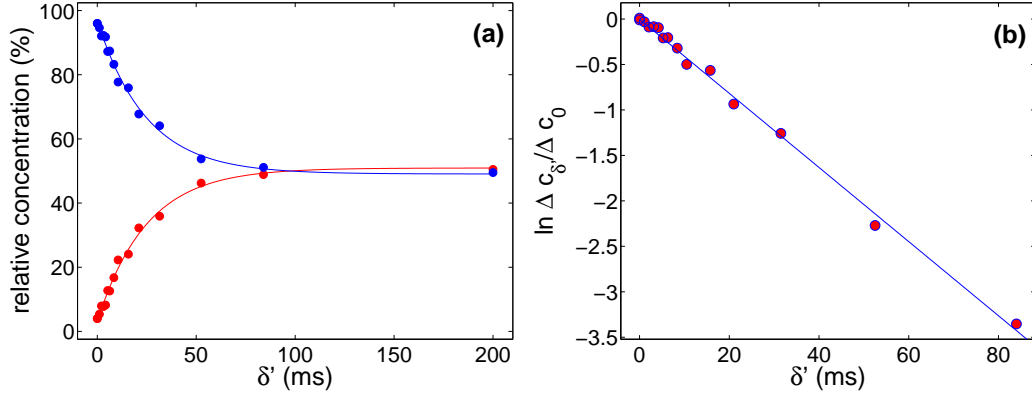


Figure 10.4: (a) Time-dependent concentration profile of the two Cyt *c* components after a potential jump from -80 mV to +20 mV for a Ag-MUA/MU-Cyt *c* electrode (Red: Cyt *c* oxidized, blue: Cyt *c* reduced). (b) Linearized concentration changes as a function of the delay time δ' according to eq (10.5).

of 140 mV, which corresponds to an overpotential of 115 mV with respect to Cyt *c* oxidation.

Concentration changes of the two Cyt *c* spectral contributions following a potential jump to $E_f = E^0$ for a Ag-MUA/MU-Cyt *c* preparation are plotted in Figure 10.4(a) as a function of the delay time δ' . Analysis of the kinetic data assumes a one-step relaxation process



which can be described by the following equation

$$\frac{\Delta c_{\delta'}}{\Delta c_0} = \frac{c_{\text{red}}(t = \delta') - c_{\text{red}}(t = \infty)}{c_{\text{red}}(t = 0) - c_{\text{red}}(t = \infty)} = \exp [-(k_{\text{ox}} + k_{\text{red}})t]. \quad (10.5)$$

Here, $c_{\text{red}}(t = \delta')$ denotes the concentration of reduced Cyt *c* at delay time δ' , $c_{\text{red}}(t = \infty)$ and $c_{\text{red}}(t = 0)$ stand for the equilibrium concentrations at the final potential and at the initial potential respectively. The oxidation and reduction rate constants k_{ox} and k_{red} are linked with the equilibrium constant

$$K = \frac{k_{\text{ox}}}{k_{\text{red}}}, \quad (10.6)$$

which is determined from stationary potential-dependent SERR experiments.

The rate constant for Cyt *c* oxidation is determined from the slope of the semilogarithmic plot according to the logarithmic form of eq (10.5) (see Figure 10.4(b)). The one step relaxation assumption seems to be justified

as the semilogarithmic plots result in straight lines with intercept values close to zero. Data from 7 distinct Ag-MUA/MU-Cyt *c* electrodes give an average value of the electron transfer rate constant at zero overpotential $k_{\text{ox}}^0 = 22 \pm 6 \text{ s}^{-1}$.

The electron transfer rate sensitively responds to the applied overpotential ($\eta = E_f - E^0$). Hence, for $\eta = 0.12 \text{ V}$ $k_{\text{ox}} = 120 \pm 30 \text{ s}^{-1}$ is obtained. Assuming that the heterogeneous electron transfer occurs in the nonadiabatic regime one can predict the theoretical increase of the electron transfer rate for a given overpotential η based on eq (4.25) according to

$$k_{\text{ET}}^\eta = k_{\text{ET}}^0 \frac{1 - \text{erf}\left(\frac{\lambda + F\eta}{2\sqrt{\lambda RT}}\right)}{1 - \text{erf}\left(\frac{\lambda}{2\sqrt{\lambda RT}}\right)}, \quad (10.7)$$

where λ denotes the reorganization energy for which the value of 0.24 eV was adopted from SERR investigations of Cyt *c* electrostatically adsorbed to a mercaptohexadecanoic acid coated electrode.¹²⁴ For an overpotential of ca. 0.12 V the calculation results in a rate constant of $200 \pm 20 \text{ s}^{-1}$. The measured rate is however smaller.

Presumably, the heterogeneous electron transfer at a distance of 11 methylene units from the electrode falls into the intermediate regime between the exponential dependence and the independence of the observed electron transfer rate on the donor-acceptor separation (see Section 9.1 and especially Figure 9.1). The two possible sources of the plateau region in the rate-distance plot at short separations were exhaustively discussed in the previous section and it was concluded that the heterogeneous electron transfer of coordinatively adsorbed Cyt *c* was controlled by friction. In the case of electrostatically attached Cyt *c*, however, a conformational rearrangement was suggested as the rate limiting step^{123,140} and has recently been confirmed by SERR measurements in our laboratory.¹⁶³ Most likely, heterogeneous electron transfer of Cyt *c* immobilized on a MUA/MU SAM is not fully controlled by tunneling. Protein reorientation is probably occurring in a comparable time scale thereby affecting the measured rate constant, although the effect is minimized for measurements at zero driving force.

The standard electron transfer rate constant was also evaluated by cyclic voltammetry based on the method developed by Laviron.¹⁶⁴ For small peak separations, i.e. $\Delta E_p < 0.2/n \text{ V}$ ($\Delta E_p = E_{pa} - E_{pc}$, n is the number of transferred electrons)

$$m^{-1} = \frac{F}{RTk^0}v, \quad (10.8)$$

where m^{-1} is a parameter related to ΔE_p . F stands for the Faraday constant, R denotes the universal gas constant and T the absolute temperature. Peak

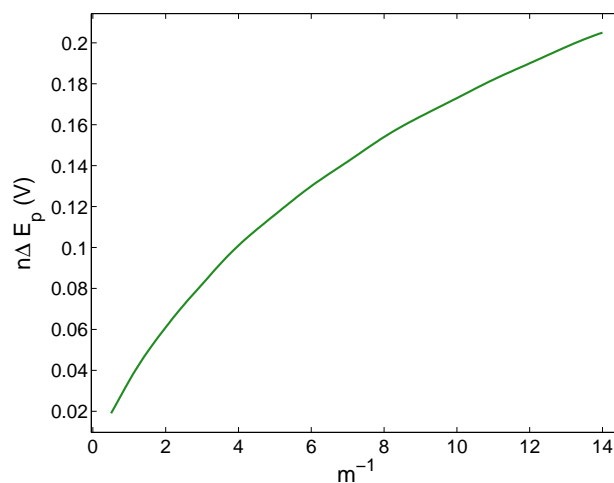


Figure 10.5: Relationship between $n\Delta E_p$ and m^{-1} .¹⁶⁴

separations were determined at different scan rates from 0.05 to 1.0 Vs^{-1} and the corresponding m^{-1} values (Figure 10.5) were plotted as a function of v . The standard rate constant was then calculated from the slope of a linear fit to the data according to eq (10.8).

Cyclic voltammograms for a Ag-MUA/MU-Cyt *c* preparation at different scan rates are depicted in Figure 10.6(a). Figure 10.6(b) displays the corresponding plot of the parameter m^{-1} as a function of the scan rate and the best fit to eq (10.8). An average rate constant of $k_{\text{ox}}^0 = 25 \pm 10 \text{ s}^{-1}$ was obtained from measurements of 4 different Ag-MUA/MU-Cyt *c* electrodes in an excellent agreement with the SERR determination.

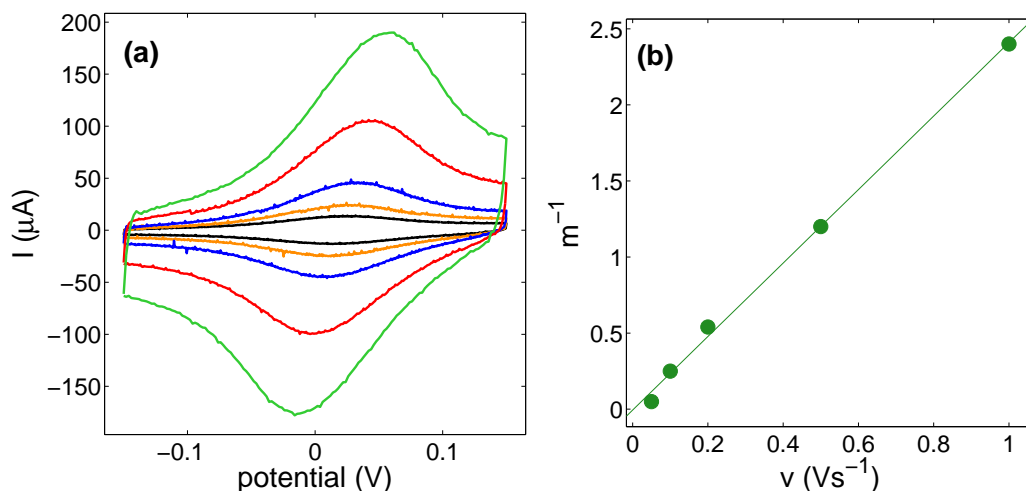


Figure 10.6: Determination of the standard rate constant from the scan rate dependence of the peak separation for a Ag-MUA/MU-Cyt *c* electrode: (a) CVs as a function of scan rate ($v = 0.05, 0.1, 0.2, 0.5$ and 1.0 Vs^{-1}); (b) corresponding plot illustrating the Laviron method.

10.3 Stationary SERR and CV investigations of the multilayer assemblies

10.3.1 PASA-Cyt *c* multilayers

Ag-MUA/MU-Cyt *c*-(PASA-Cyt *c*)_{*k*} multilayers ($k = 1, 3, 6$ and 10) were formed by the layer-by-layer deposition of PASA and Cyt *c* as described in Section 6.2.2. The SERR spectra of the multilayer preparations, plotted in the left panel of Figure 10.7, exhibit the typical bands of the reduced and oxidized native Cyt *c*, which are again identical to the RR spectra of Cyt *c* in solution. Hence, immobilizing Cyt *c* within the polyelectrolyte layer does not induce any Cyt *c* spectral changes indicating that no protein denaturation occurred.

In addition to the Cyt *c* bands, the spectra of the multilayer systems show a band at ca. 1620 cm^{-1} , which was assigned to the C=C and C-C stretching vibrations of the quinoid and benzenoid rings of the PASA polyaniline chain, respectively.^{165,166} Thus apart the component spectra of the reduced and oxidized Cyt *c*, a PASA contribution has to be included in the quantitative treatment of the potential-dependent spectra by component analysis. In order to obtain a satisfactory global fit, it was necessary to define two slightly different PASA spectral contributions, PASA 1 dominates the spectra at negative potentials and PASA 2 at positive potentials (Figure 10.7). The

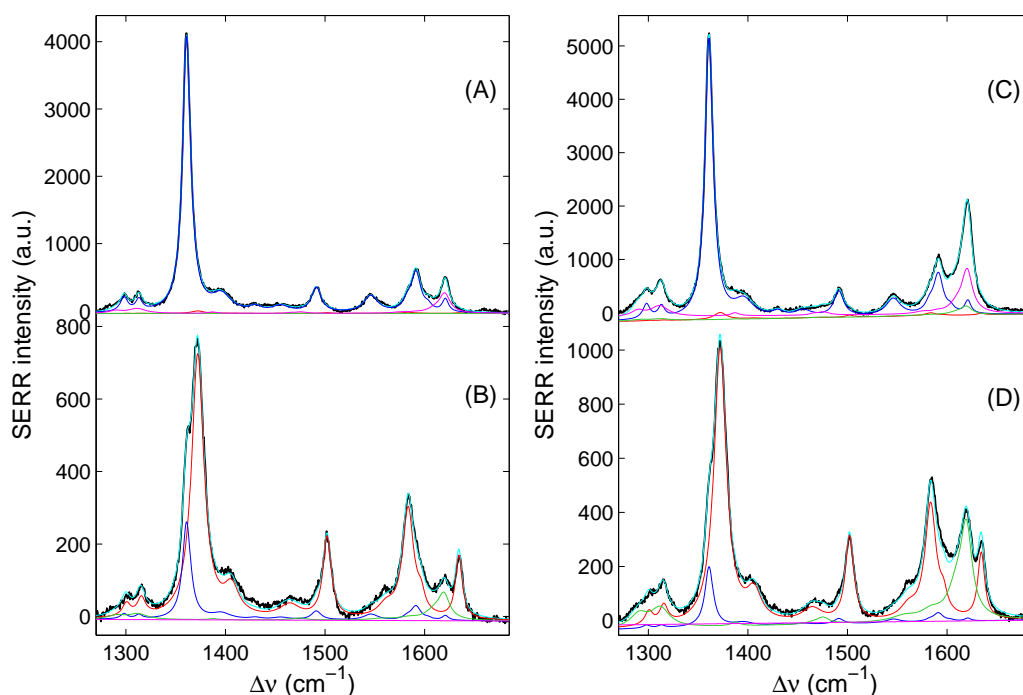


Figure 10.7: Measured SERR spectra and component analysis of the Ag-MUA/MU-Cyt-(PASA-Cyt)₃ preparation (left panel) at two different potentials: (A) -0.1 V and (B) +0.12 V and of the Ag-MUA/MU-Cyt-(PASA-Cyt)₃ preparation after thermal stabilization (right panel) at (C) -0.1 V and (D) +0.12 V. Black: experimental spectra, cyan: overall fit, red: Cyt *c* oxidized, blue: Cyt *c* reduced, magenta: PASA 1 and green: PASA 2.

definition of the two PASA components along with their spectral parameters will be detailed in the next section.

Heating the multilayer electrodes at 45°C for 30 minutes was found to stabilize the assembly.¹⁵⁴ SERR spectra of the thermally treated samples, shown in the right panel of Figure 10.7, did not show any changes in the Cyt *c* spectral components (compare left and right panel of Figure 10.7) and could be satisfactorily fitted with the two native Cyt *c* components and the two PASA components. The only difference, which was consistently observed, was a 2 to 4 fold higher relative contribution of the polyelectrolyte band (with respect to the Cyt *c* intensity) as compared to the non treated samples. During thermal treatment, the polyelectrolyte probably gets closer to the electrode surface and the whole structure gets more compact what would explain the higher stability of heated multilayers on Au electrodes.¹⁵⁴

As an example, the concentration profile and Nernst analysis of the Cyt *c* redox transition for a 3 layer assembly are plotted in Figure 10.8. For all

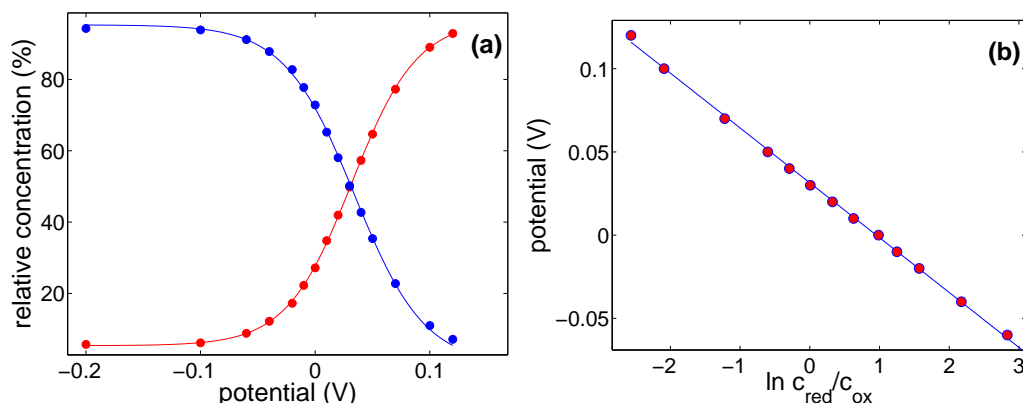


Figure 10.8: Potential dependent measurements for a Ag-MUA/MU-Cyt *c*-(PASA-Cyt *c*)₃ electrode: (a) concentration profile (Red: Cyt *c* oxidized, blue: Cyt *c* reduced) and (b) the corresponding Nernst plot.

Ag-MUA/MU-Cyt *c*-(PASA-Cyt *c*)_{*k*} assemblies (*k* = 1, 3, 6 and 10) including the thermally stabilized electrodes the Nernst plots are essentially identical and give an average value of Cyt *c* formal redox potential $E^0 = 28 \pm 6$ mV and the number of transferred electrons $n = 0.9 \pm 0.1$ for a total of 20 distinct electrodes. The value determined from cyclic voltammograms $E^0 = 23 \pm 6$ mV is in a very good agreement with the SERR analysis. The redox potential of Cyt *c* in the polyelectrolyte layer is within the experimental error the same as the value found for the electrostatically adsorbed Cyt *c*, in agreement with previous results.¹⁵² The native protein structure and the ideal electrochemical behavior are also maintained upon thermal treatment used to stabilize the assembly.

Interestingly, no pronounced Cyt *c* SERR absolute intensity changes were observed depending on the number of layers in the multilayer assembly. The 20 electrodes with different multilayer preparations yield an average absolute intensity of Cyt *c* at -0.1 V of $I = 4000 \pm 500$ counts for a 1 s accumulation time at a laser power of 1 mW. Surface-enhanced Raman (SER) absolute intensity is subject to large variations as the surface enhancement factor, the surface concentration and other instrumental parameters may vary from preparation to preparation; large amount of experimental data should nevertheless help to overcome this limitation. Moreover, the surface enhancement effect decays with the distance of the studied species to the electrode in an approximately exponential fashion. SERR spectra are therefore dominated by the contribution from molecules in the vicinity of the SAM interface. Despite these restrictions, it would have been reasonable to expect a Cyt *c* SERR absolute intensity increase when passing from one to ten PASA-Cyt *c* layers in

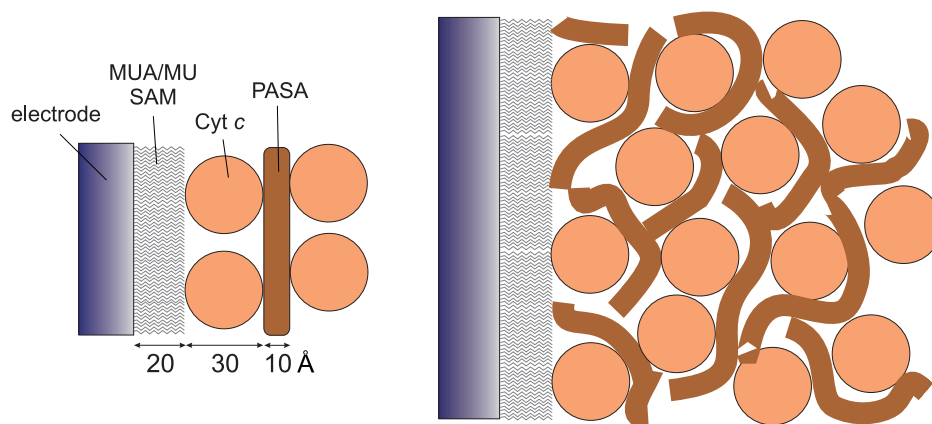


Figure 10.9: Geometrical considerations of an ideal PASA/Cyt *c* layer structure (left) and more realistic scheme of the multilayer assembly (right). The thickness of the mixed MUA/MU SAM was taken from literature data for a MUA SAM on Ag electrodes,¹¹² PASA was shown to have an effective diameter of ca. 10 Å.¹⁵⁸

the multilayer since the individual layers are not expected to be perfect and Cyt *c* molecules from the outer layers are likely to get closer to the electrode surface than the geometrical prediction. A scheme of the possible multilayer arrangement along with simple geometrical considerations are depicted in Figure 10.9. Furthermore, as will be shown in the next chapter, decent SERR signals can be obtained from heme sites placed as far as 50 Å from the electrode.

In order to quantify the protein loading, CV scans were acquired before and after SERR measurement from the same electrodes, only the rotation was stopped. As shown in the previous section, the formal potential values and the standard rate constants coming from the two different methods (SERR and CV) are in a very good agreement.

Figure 10.10(a) displays CV scans of the multilayer electrodes as a function of the number of (PASA-Cyt *c*) adlayers. In Figure 10.10(b), the electroactive protein coverage in the very first CVs recorded immediately after electrode insertion into the electrochemical cell is compared to those obtained ca. 10 minutes later, just before the SERR experiment. The latter values are essentially the same as those recorded after the SERR experiment about 1.5 hour later. The very first values show the expected increase of protein loading with increasing the number of layers, the amount of electrochemically adressable protein almost triplicates upon increasing the number of layers from 1 to 10. The multilayer construct is nevertheless not stable, the additional layers get lost. As observed in successive CV measurements (Fig-

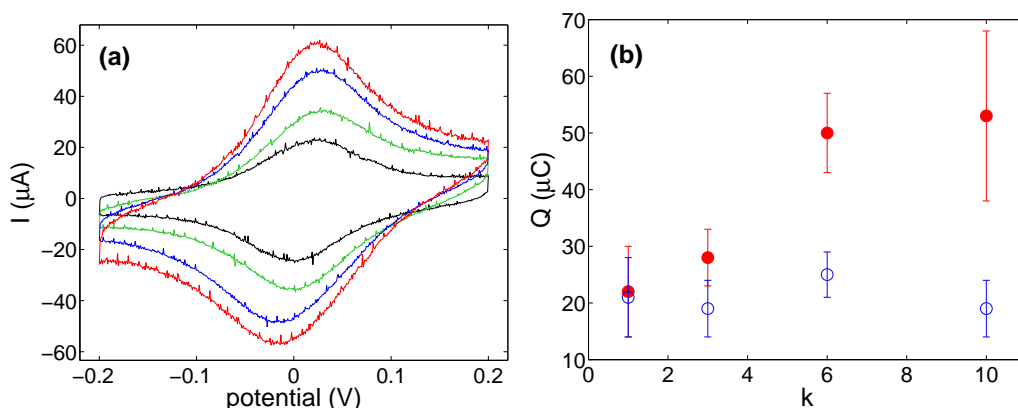


Figure 10.10: Increase of protein loading with the number of PASA-Cyt *c* layers: (a) CVs of the Ag-MUA/MU-Cyt *c*-(PASA-Cyt *c*)_k electrodes with *k* = 1 (black), 3 (green), 6 (blue) and 10 (red) measured immediately after preparation; (b) protein loading as a function of the number of (PASA-Cyt *c*) adlayers (*k*) immediately after insertion of the electrode to the electrochemical cell (red) and after ca. 10 minutes (blue) (except for the value at 10 layers all points correspond to an average of at least 4 measurements).

ure 10.11), the most important decrease occurs in a short time scale before the beginning of the SERR experiment. The protein loading decreases to the level of 1 PASA-Cyt *c* layer and remains stable for several hours.

Hence cyclic voltammetry measurements furnished an explanation for the apparent insensitivity of SERR intensity to the number of layers showing that the multilayer assembly is not stable on rough Ag electrodes used for SERR experiments. This observation is in a sharp contrast to experiments performed on Au electrodes.^{152,153,154} An increase of the redox active protein loading with the number of PASA-Cyt *c* layers is observed only in the very first CV measurements after electrode insertion into the electrochemical cell. The increase of electrochemically addressable protein amount is comparable to previous results on Au needle electrodes.¹⁵²

The layer loss occurs before the SERR measurement starts, it is thus related neither to the stress induced by the laser light nor to the rotation of the electrode. The CV signal decreases steeply within few CV scans to reach the level of one PASA-Cyt *c* layer, as suggested by the simultaneous presence of Cyt *c* and PASA contributions in the SERR spectra. Therefore, the electrodes investigated by SERR spectroelectrochemistry are better described as Ag-MUA/MU-Cyt *c*-PASA-Cyt *c* independently of the number of adsorption steps during the layer-by-layer assembly.

The layer-by-layer adsorption procedure is performed in a buffer of low

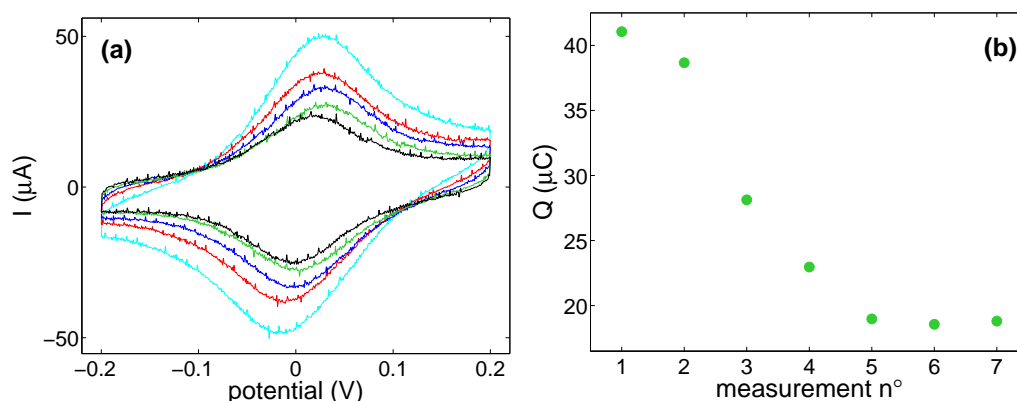


Figure 10.11: Instability of a Ag-MUA/MU-Cyt *c*-(PASA-Cyt *c*)₆ multilayer assembly: (a) successive CVs acquired under identical conditions before (cyan, red, blue, green) and after (black) SERR experiment and (b) the corresponding decrease of the protein loading as a function of measurement number: measurements 1-4 were performed before the SERR experiment, measurements 5-7 afterwards.

ionic strength (0.5 mM phosphate buffer) and pH 5.0, while for measurement a ten times more concentrated buffer of pH 7.0 was employed. Unlike multilayer assemblies on Au electrodes, which remain stable, multilayers on Ag electrodes are presumably more loosely bound so that buffer ions can easily penetrate into the structure, shield the charges and disrupt electrostatic interactions between the individual layers. The important roughness of SERR-active Ag electrodes could also play an unfavorable role by providing a rather irregular support for adsorption.

10.3.2 Apo containing multilayers

Apocytochrome *c* (Apo) lacks the heme moiety and is thus redox and RR inactive. Individual layers of Cyt *c* in the multilayer preparations were replaced by Apo in order to shed some light on the geometry of the construct.

In a first step, the 1-layer assembly with all Cyt *c* replaced by Apo (Ag-MUA/MU-Apo-PASA-Apo) was used to better resolve the polyelectrolyte bands and define the PASA spectral contributions. The potential window was extended as much as possible and spectra were measured at potentials down to -0.7 V and up to +0.25 V. The maximum positive potential is limited by the relatively low Ag oxidation potential. In fact spectra can be acquired up to +0.3 V but the spectral quality is decreasing accompanied by the apparition of non-native states of Cyt *c*.

As depicted in Figure 10.12, only the polyelectrolyte bands are present

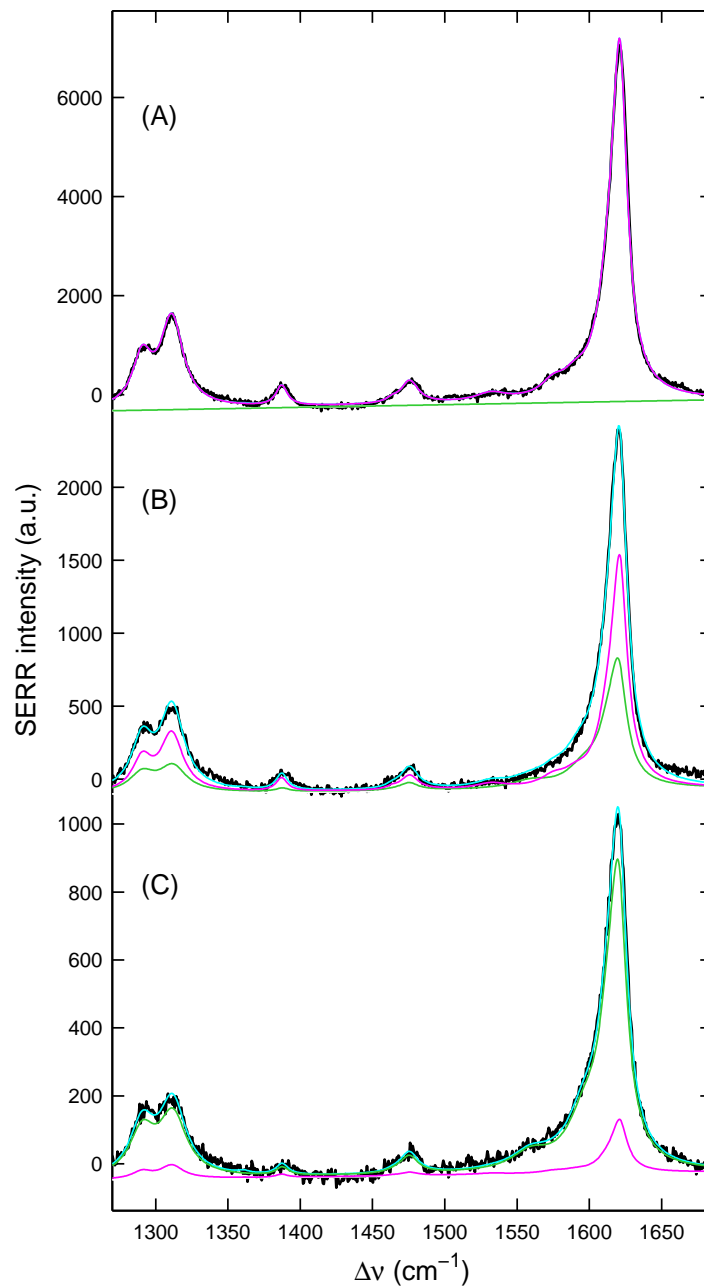


Figure 10.12: Measured SERR spectra and component analysis of the Ag-MUA/MU-Apo-PASA-Apo preparations at three different potentials: (A) -0.4 V, (B) +0.14 V and (C) +0.25 V. Black: experimental spectra, cyan: overall fit, magenta: PASA 1 and green: PASA 2.

Table 10.1: Spectral parameters of the PASA 1 and PASA 2 components.

PASA 1			PASA 2		
Peak position (cm ⁻¹)	Intensity ^a	FWHM (cm ⁻¹)	Peak position (cm ⁻¹)	Intensity ^a	FWHM (cm ⁻¹)
1290.6	0.16	16.3	1290.7	0.19	21.4
1311.1	0.30	19.3	1311.9	0.27	23.0
1387.1	0.07	9.6	1387.6	0.03	10.4
1475.6	0.08	14.8	1475.4	0.08	15.0
1575.1	0.05	20.1	1559.3	0.07	31.0
1590.0	0.05	20.0	1596.9	0.20	28.6
1614.3	0.33	19.7	1613.5	0.46	18.3
1621.2	1.00	12.0	1620.3	1.00	13.3

^anormalized with respect to the most intense band

in the Ag-MUA/MU-Apo-PASA-Apo preparation spectra. As well as in the multilayer assembly with Cyt *c*, the polyelectrolyte undergoes potential-dependent spectral changes. Upon raising the electrode potential from -0.4 V to +0.25 V the SERR intensity of the polyelectrolyte drops by a factor of ca. 7. The intensity drop is reversible within a 10% error margin and thus cannot be ascribed to a partial desorption of the polyelectrolyte.

The intensity drop is accompanied by relatively small but distinct spectral changes which are indicative of chemically different species. Namely, the most prominent PASA band which appears at 1621 cm⁻¹ at negative potentials downshifts by ca. 1 cm⁻¹ when the potential is increased. This band is also broader with a more pronounced shoulder on the low frequency side at positive potentials. Furthermore one can observe a potential-dependent change in relative intensities of the two bands at 1291 cm⁻¹ and 1311 cm⁻¹. The Ag-MUA/MU-Apo-PASA-Apo electrode spectra at -0.4 and +0.25 V served to define the PASA 1 and PASA 2 component spectra respectively. As shown in Figure 10.12, the SERR spectra at intermediate potentials were successfully simulated with these two components. Spectral parameters of the PASA 1 and PASA 2 components are listed in Table 10.1.

A tentative band assignment was performed on the basis of literature data for polyanilines and sulfonated polyanilines. The doublet at 1291 and 1311 cm⁻¹ can be ascribed to the C-H deformation mode of quinoid and benzenoid rings respectively.¹⁶⁷ The small band at 1387 cm⁻¹ presumably corresponds to the stretching of the C~N bond, i.e. intermediate bond be-

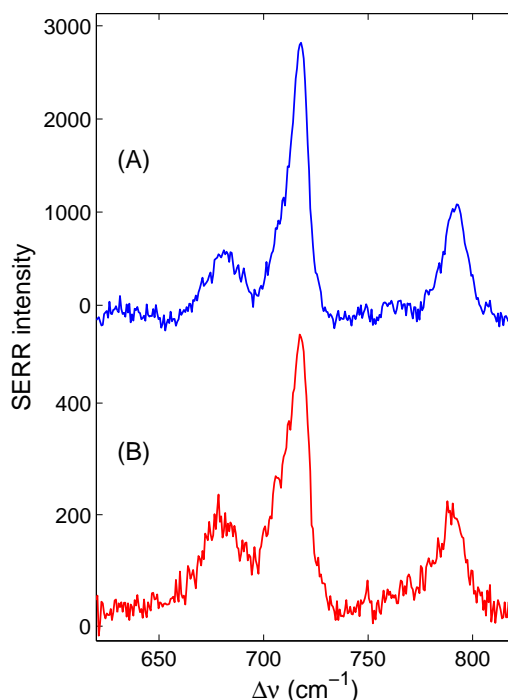


Figure 10.13: Measured SERR spectra Ag-MUA/MU-Apo-PASA-Apo preparations at two different potentials: (A) -0.4 V and (B) $+0.14$ V.

tween the single and double CN bonds.¹⁵⁶ Finally, bands at around 1590 cm^{-1} arise from the C=C stretching of the quinoid rings. C-C stretching of the benzenoid rings occur at around 1620 cm^{-1} .^{156,165,166,168} The changes detected between the PASA 1 and PASA 2 components thus correspond to an increase of the quinoid ring content in the polymer. This hypothesis is furthermore supported by an observation in the low frequency region of the spectra which was not routinely monitored (shown in Figure 10.13). Namely, the increasing quinoid amount is confirmed by the relative intensity change of a doublet that appears at 680 and 717 cm^{-1} and can be assigned to the out-of-plane deformation of the quinoid and benzenoid ring respectively.¹⁶⁹ The ratio I_{717}/I_{680} decreases from 3.5 to 2.5 upon raising the potential.

In the next step, several multilayer assemblies of the type Ag-MUA/MU-Apo-(PASA-Apo) $_{k-1}$ -PASA-Cyt *c* with $k = 1, 2, 3, 5$ and 7 were prepared, i.e. multilayers containing Apo in the inner layers and Cyt *c* in the outer layer. As can be inferred from SERR potential-dependent stationary spectra of a Ag-MUA/MU-Apo-PASA-Cyt *c* preparation in Figure 10.14, the polyelectrolyte undergoes the same type of potential-induced spectral changes as those described previously for the only Cyt *c* and only Apo layer system.

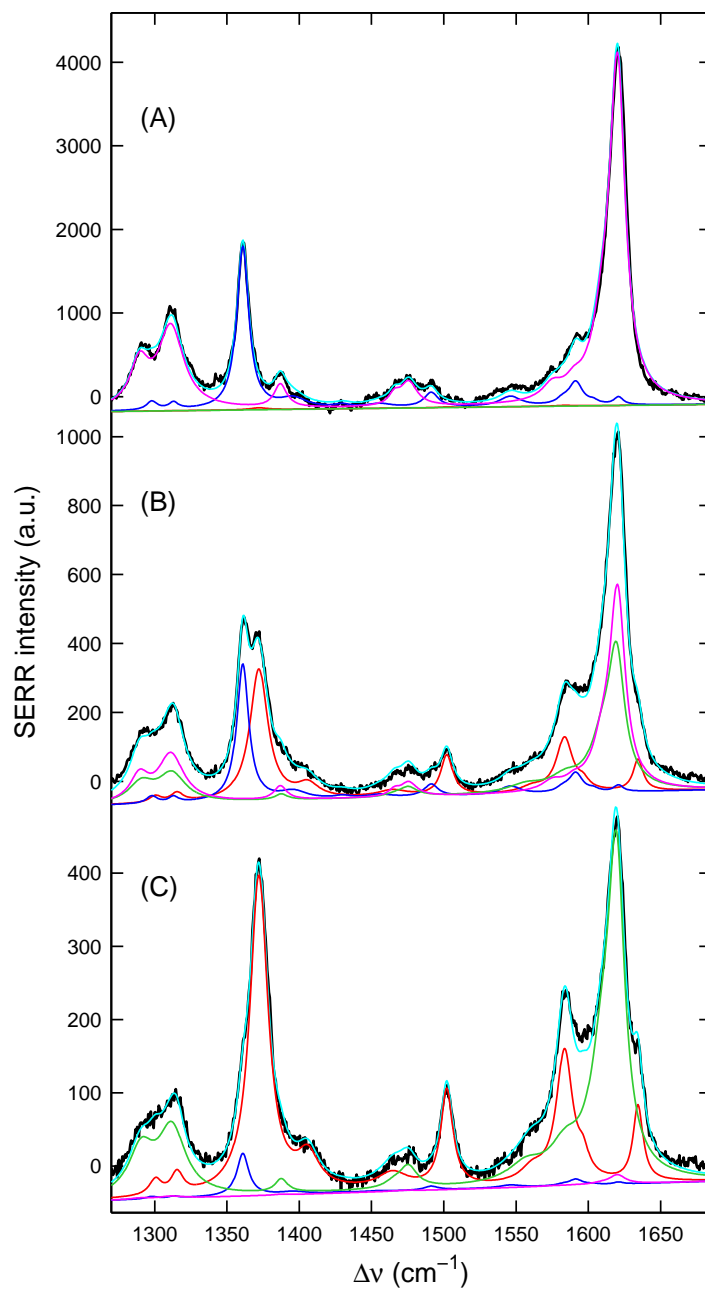


Figure 10.14: Measured SERR spectra and component analysis of the Ag-MUA/MU-Apo-PASA-Cyt preparations at three different potentials: (A) -0.2 V, (B) +0.06 V and (C) +0.14 V. Black: experimental spectra, cyan: overall fit, magenta: PASA 1 and green: PASA 2.

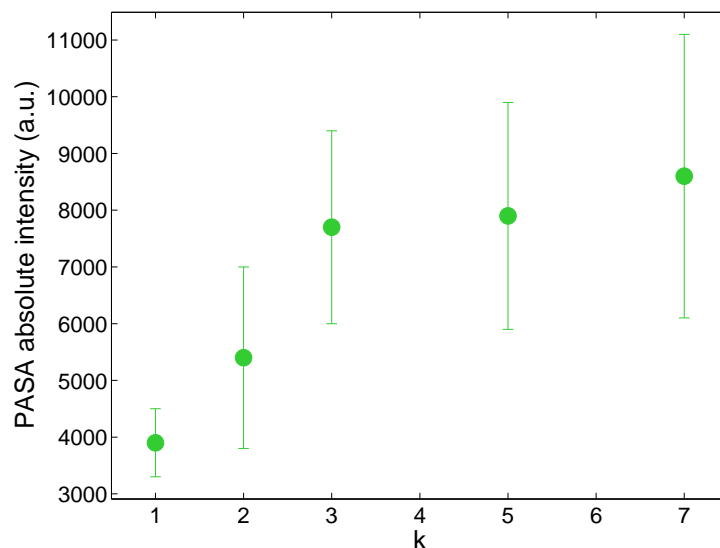


Figure 10.15: Thickness dependence of the SERR absolute intensity of the PASA band at 1620 cm^{-1} in a 1 s accumulation at a power of 1 mW and a potential of -0.1 V for Ag-MUA/MU-Apo-(PASA-Apo) $_{k-1}$ -PASA-Cyt *c* preparations.

The absolute intensity of Cyt *c* is within the experimental error independent of the number of layers yielding an average value of $I = 2400 \pm 400$ counts in a 1 s accumulation time at a power of 1 mW and a potential of -0.1 V for 11 distinct electrodes. Compared to the pure Cyt *c* system, this intensity is smaller by about a factor of 2. On the other hand, the polyelectrolyte contribution is significantly more important (compare Figure 10.7 and Figure 10.14) and exhibits an increasing tendency with the number of layers despite a large experimental error associated with the PASA intensity as depicted in Figure 10.15.

The Nernstian analyses of the different Apo-Cyt *c* multilayer systems (a total of 11 distinct electrodes) give the redox potential for Cyt *c* of $E^0 = 25 \pm 8$ mV and the number of transferred electrons $n = 0.9 \pm 0.1$.

CV measurements on the same electrodes result in $E^0 = 23 \pm 8$ mV, in perfect agreement with the SERR determination. As displayed in Figure 10.16, the voltammetric waves are significantly broader in comparison to the only Cyt *c* containing layers pointing to a substantial heterogeneity of the adsorbed layer. Interestingly, the peak currents are very high taken into account that only 1 layer of the electroactive protein should be present. Moreover, the integrated charge of the voltammetric waves exhibits a slightly increasing tendency with the number of PASA-Apo inner layers (see Fig-

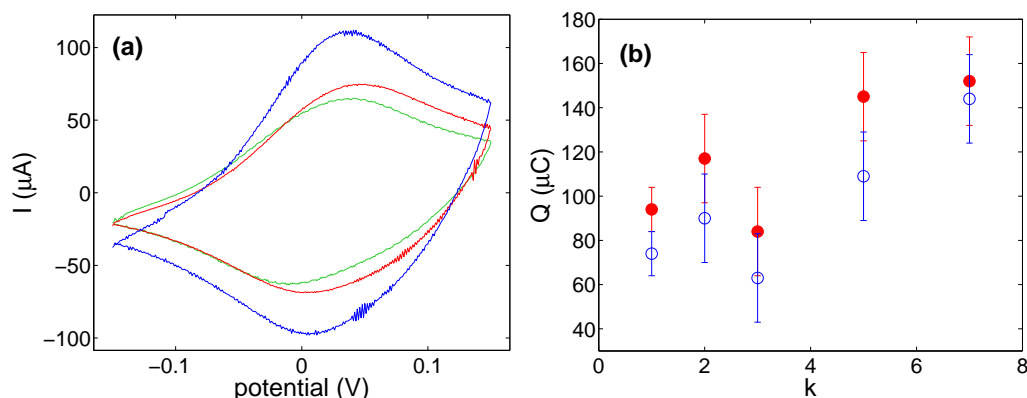


Figure 10.16: Electrochemical measurements on Ag-MUA/MU-Apo-(PASA-Apo) $_{k-1}$ -PASA-Cyt *c* preparations: (a) CV scans for $k = 1, 2$ and 7 ; (b) protein loading as a function of k before (red) and after (blue) the SERR experiment.

ure 10.16(b)). An important broadening of the CV scans and relatively high currents were observed also in previous experiments on Au needle electrodes, but the origin of this peculiar behavior was not addressed.¹⁵² A precise determination of the peak parameters is however aggravated by the broadening of the voltammograms together with the limited potential range available on Ag electrodes. The peak currents decrease with time. Unlike Ag-MUA/MU-Cyt *c*-(PASA-Cyt *c*) $_k$ multilayers, however, the signal loss occurs on the time scale of tens of minutes and does not exceed 20%.

The apparently diverging results of the SERR and CV measurements, i.e. a lower absolute intensity of Cyt *c* in SERR spectra and higher peak currents in CV scans of the Ag-MUA/MU-Apo-(PASA-Apo) $_{k-1}$ -PASA-Cyt *c* with respect to the Ag-MUA/MU-Cyt *c*-PASA-Cyt *c* system, can be explained by a different adsorption behavior of Cyt *c* and Apo during the layer formation. In fact, the apoprotein was shown to be highly unfolded; nevertheless, its structure is significantly compact in acidic buffers at low ionic strength.^{93,170,171} Therefore, the surface exposed residues are likely to be different for the two proteins. The polyelectrolyte exhibits a higher affinity for Apo as indicated by the significantly larger PASA contribution in the Apo containing preparations. The multilayers with Apo are more stable than those with Cyt *c*. Though a decrease of the CV signal is observed, it is less pronounced than for the Ag-MUA/MU-Cyt *c*-(PASA-Cyt *c*) $_k$ system. Moreover, an increase of the PASA SERR absolute intensity with the number of layers points to an increasing Apo loading of the electrode. Presumably, a larger amount of Cyt *c* is adsorbed in the last adsorption step of the Ag-MUA/MU-Apo-

(PASA-Apo) $_{k-1}$ -PASA-Cyt *c* multilayer preparation giving rise to higher CV currents and lower SER enhancement in the same time.

10.4 PASA potential-dependent changes

As described in the previous section, two spectrally distinct components were defined in order to render the potential dependence of the PASA contribution. The potential induced changes of the PASA 1 and PASA 2 absolute intensities are displayed in Figure 10.17 for a Ag-MUA/MU-Cyt *c*-PASA-Cyt *c* (only Cyt *c*) and a Ag-MUA/MU-Apo-PASA-Apo (only Apo) preparation. Qualitatively, the polyelectrolyte undergoes in both systems the same type of potential dependent changes. The overall PASA contribution is decreasing over the whole potential range. At -0.4 V only the PASA 1 component is present, its intensity decreases as the potential becomes more positive, later on appears the PASA 2 component, which dominates at +0.25 V. The intensity changes displayed in Figure 10.17 are reversible within a 10% error range, the role of potential-induced desorption can thus be excluded or at least minimized.

Nevertheless, quantitative differences can be observed between the two systems in Figure 10.17. The transition of the PASA 1 component seems to be better defined in the Cyt *c*-PASA-Cyt *c* layer, the PASA 2 intensity increase is monotonic in the Apo-PASA-Apo assembly in contrast to the Cyt *c*-PASA-Cyt *c* system. Unlike Cyt *c*, the relative cross sections for the two PASA spectral components are unknown and their intensities cannot thus be converted to relative concentrations. Alternatively, in order to compare results from different electrodes, normalized intensity was defined so that the absolute intensity at the most negative potential (-0.4 V) was considered as 1. Figure 10.18 compares the potential dependence of the normalized PASA 1 intensity for the only Cyt *c* and only Apo containing layer electrodes. For Ag-MUA/MU-Apo-PASA-Apo preparations, the intensity drop of the PASA 1 species is gradual over the whole potential range displayed. In contrast, Ag-MUA/MU-Cyt *c*-PASA-Cyt *c* electrodes display a better defined transition at about 15 mV, which is very close to the formal redox potential of immobilized Cyt *c*. This coincidence suggests that the polyelectrolyte is implied in the heterogeneous electron transfer through the PASA-Cyt *c* assembly.

In fact, polyanilines undergo redox transitions between the oxidized pernigraniline form through the emeraldine base to the reduced leucoemeraldine form, as schematized in Figure 10.19. Indeed, polyaniline films were shown to exhibit two redox transitions at approx. +0.2 and +0.8 V (vs. Ag/AgCl sat. KCl).¹⁷² Moreover, protonation of the emeraldine base leads to the

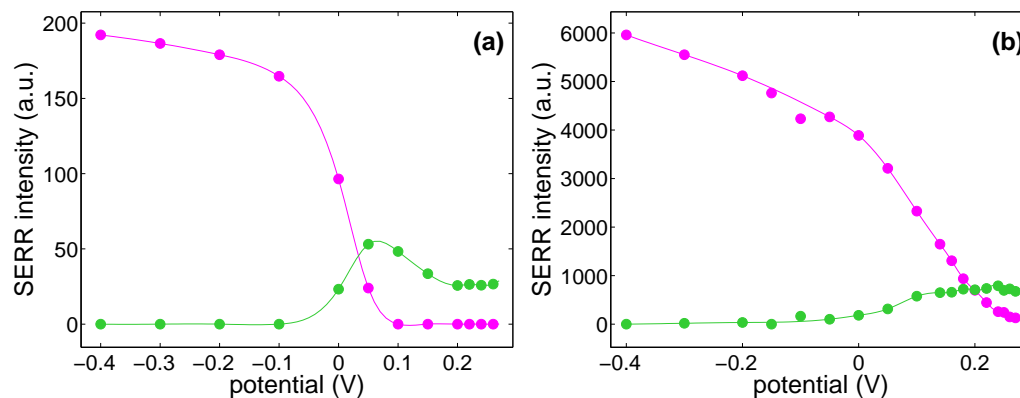


Figure 10.17: Absolute intensities of the two PASA spectral components (magenta: PASA 1 and green: PASA 2) as a function of the electrode potential for: (a) a Ag-MUA/MU-Cyt *c*-PASA-Cyt *c* electrode and (b) a Ag-MUA/MU-Apo-PASA-Apo electrode. The lines are intended to guide the eye only.

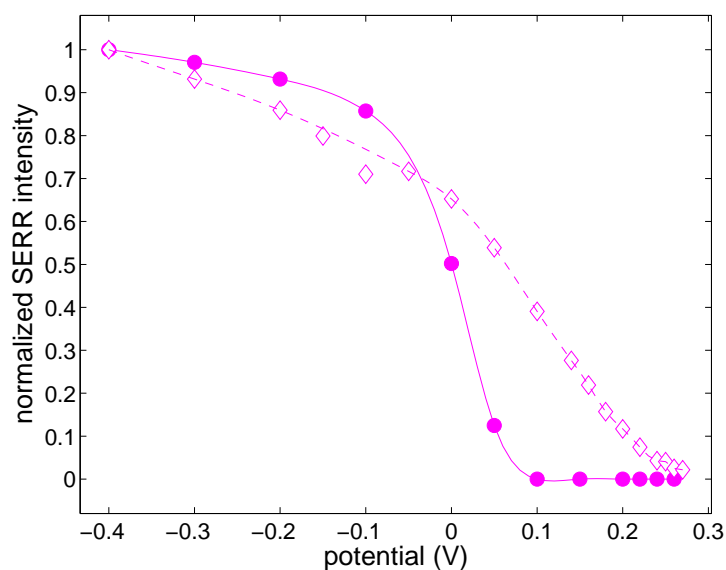


Figure 10.18: Normalized intensity of the PASA 1 intensity as a function of electrode potential for a Ag-MUA/MU-Cyt *c*-PASA-Cyt *c* (solid circles) and a Ag-MUA/MU-Apo-PASA-Apo (hollow diamonds) electrode. In order to normalize the intensities, the PASA intensity at -0.4 V is considered as 1.

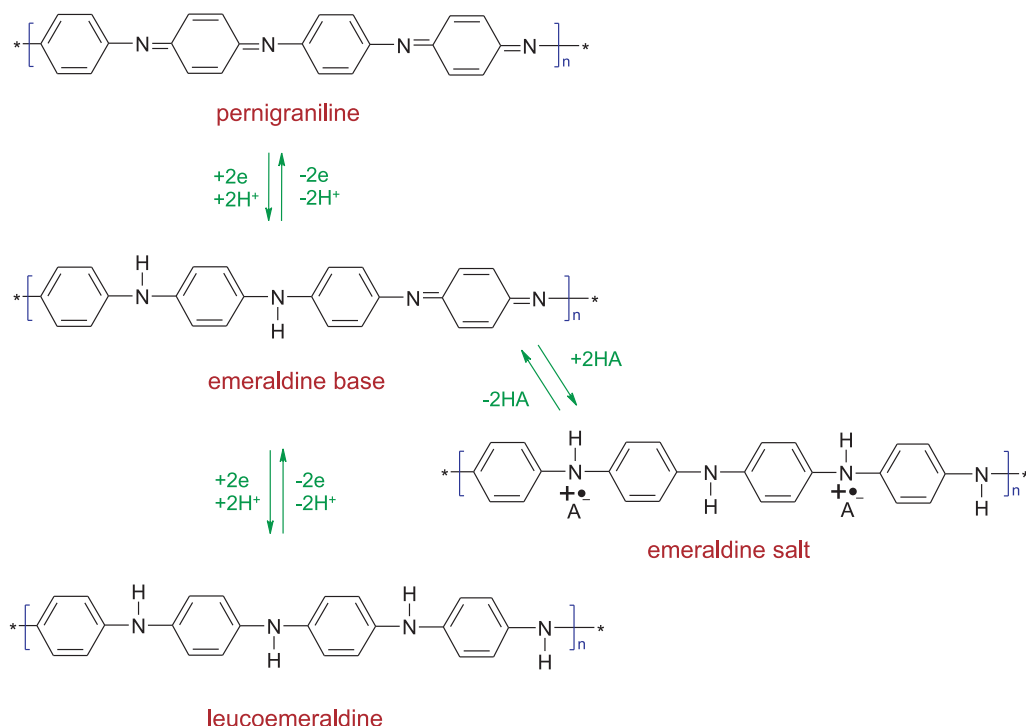


Figure 10.19: Redox and protonation transitions of polyanilines.^{167,174,175}

emeraldine salt, which can be conducting under certain conditions and thus a potential candidate for rechargeable battery production.¹⁷³ Applications of polyaniline are however limited by its low solubility in aqueous solvents and by the narrow pH range of conductivity, polyaniline is conducting only at $\text{pH} < 4$.¹⁵⁸ A self-doped conducting polymer, the so called sulfonated polyaniline (PASA in this work*), can be synthesized upon introducing a $-\text{SO}_3\text{H}$ group on the polyaniline chain.¹⁵⁸ The solubility of this polymer is greatly enhanced by the presence of the $-\text{SO}_3^-$ groups and its conductivity is independent of protonation in a broad pH range (up to pH 7.5) thanks to the self-doping properties. Two redox processes were reported also for PASA in aqueous solutions of strong acids at essentially identical potentials as found for polyanilines.^{155,158} The redox transitions were found to shift to lower potentials upon decreasing acidity both for polyanilines and sulfonated polyanilines.^{158,172}

The polyaniline redox/protonation states differ in color and thus in the absorption spectra.^{176,177,178} The very strong PASA intensity at negative po-

*Sulfonated polyaniline is more frequently abbreviated as SPAN, PASA is employed to keep continuity with previous work on PASA/Cyt *c* layers.^{152,153,154}

tentials can be explained in terms of a strong resonance enhancement at the excitation wavelength of 413 nm. For different kinds of sulfonated polyanilines, the absorption at ca. 420 nm was assigned to the radical cation (emeraldine salt) form of the polyelectrolyte, which is responsible for the conductivity. Thus, although the present results do not allow for an unambiguous determination, most likely the SERR spectra recorded at two extreme potentials represent different redox/protonation states of PASA having different SERR cross sections at the excitation wavelength. This conclusion is supported by the relatively small but distinct changes between the two PASA spectral components which are indicative of chemically different species. Moreover the spectral changes suggest an increase in the content of quinoid rings upon raising potential which is consistent with oxidation of the polyelectrolyte. Based on the SERR spectra, it can be thus concluded that at negative potentials PASA is present in the form of emeraldine salt and upon protonation and oxidation is at least partly transformed to the pernigraniline form at +0.25 V.

In the Ag-MUA/MU-Cyt *c*-PASA-Cyt *c* system, the reversible PASA redox/protonation transition is well defined and occurs in the same potential range as the redox reaction of immobilized Cyt *c* suggesting a PASA-Cyt *c* electron exchange. The PASA transition in the Ag-MUA/MU-Apo-PASA-Apo preparation is shifted to more positive potentials and clearly broader. This observation can be rationalized in terms of direct electron transfer between the electrode and the polyelectrolyte by electron tunneling. The broadness of the transition can be ascribed to a distribution of PASA redox centers.

10.5 Electron transfer dynamics

Electron transfer dynamics in the Ag-MUA/MU-Cyt *c*-PASA-Cyt *c* and Ag-MUA/MU-Apo-PASA-Apo systems was investigated by TR-SERR spectroelectrochemistry as described in Section 10.2.2 for the electrostatically adsorbed Cyt *c*. SERR spectra were acquired at variable delay times after a potential jump from an initial potential of -80 mV to a final potential of +25 mV or +140 mV, that correspond to zero driving force and an overpotential of ca. 115 mV for Cyt *c* oxidation respectively. For illustration, SERR spectra of the Ag-MUA/MU-Cyt *c*-PASA-Cyt *c* preparation at different delay times after a potential jump to the Cyt *c* redox potential are plotted in Figure 10.20. The polyelectrolyte signal at the initial potential is largely dominated by the intense PASA 1 contribution as the weaker PASA 2 usually starts to appear at around 0 mV. As illustrated in Figure 10.20, the TR-SERR spectra could be satisfactorily simulated by four components which are identical to

those employed in the analysis of the stationary potential-dependent SERR spectra, i.e. Cyt *c* reduced, Cyt *c* oxidized, PASA 1 and PASA 2.

TR-SERR measurements on 10 Ag-MUA/MU-Cyt *c*-PASA-Cyt *c* electrodes result in an average standard rate constant for Cyt *c* oxidation $k_{\text{ox}}^0 = 17 \pm 7 \text{ s}^{-1}$. Analysis of CV scans according to the Laviron method yields $k_{\text{ox}}^0 = 20 \pm 6 \text{ s}^{-1}$ for 4 Ag-MUA/MU-Cyt *c*-PASA-Cyt *c* electrodes, which is in perfect agreement with the TR-SERR determination. The rate constant increases to $k_{\text{ox}} = 120 \pm 30 \text{ s}^{-1}$ upon applying an overpotential of 115 mV for Cyt *c* oxidation. The electron transfer rates for Cyt *c* oxidation in the Ag-MUA/MU-Cyt *c*-PASA-Cyt *c* system are thus, within the experimental error, the same as the standard rate constant for electrostatically adsorbed Cyt *c*.

As can be inferred from Figure 10.20, the time-dependent spectral changes of Cyt *c* after a potential jump are accompanied by changes in the polyelectrolyte spectral contribution in the same time scale. The intensity decay of the PASA 1 component (shown in Figure 10.21), however, cannot be satisfactorily treated as a monoexponential function and instead a minimum of two exponentials is required to obtain reasonable results. The average values of the two decay constants for 10 Ag-MUA/MU-Cyt *c*-PASA-Cyt *c* electrodes are $k_1^{\text{app}} = 35 \pm 15 \text{ s}^{-1}$ and $k_2^{\text{app}} = 1 \pm 1 \text{ s}^{-1}$. Considering that PASA oxidation occurs at ca. +15 mV, the standard rate for PASA oxidation is somewhat lower than 35 s^{-1} , though an exact assessment of this value according to eq (10.7) is not possible since the reorganization energy of the polyelectrolyte is not known. Upon applying a potential jump to +140 mV, the first PASA decay constant increases to $k_1^{\text{app}} = 135 \pm 30 \text{ s}^{-1}$ while the second decay constant remains largely unaltered ($k_2^{\text{app}} = 3 \pm 2 \text{ s}^{-1}$). This potential jump corresponds to an overpotential for PASA oxidation of ca. 125 mV, i.e. very similar to the overpotential for Cyt *c* oxidation.

The kinetics of the PASA spectral contribution was investigated also for the Ag-MUA/MU-Apo-PASA-Apo electrodes. As in the previous case, the time-dependent PASA intensity decay can be satisfactorily fitted with a bi-exponential function. The decay parameters for potential jumps to +25 mV are $k_1^{\text{app}} = 2 \pm 1$ and $k_2^{\text{app}} = 0.01 \pm 0.01$. Note that these values are significantly smaller than those for Cyt *c* containing systems. Moreover, both k_1^{app} and k_2^{app} have similar values for potential jumps to +140 mV.

Investigations of Cyt *c* dynamics by means of TR-SERR spectroelectrochemistry yielded within the experimental error identical standard rate constants for oxidation of Cyt *c* electrostatically immobilized on the mixed MUA/MU SAM and Cyt *c* adsorbed within the polyelectrolyte layer. The time-dependent changes of Cyt *c* in the latter case are accompanied by intensity decrease of the PASA spectral contribution in the millisecond and

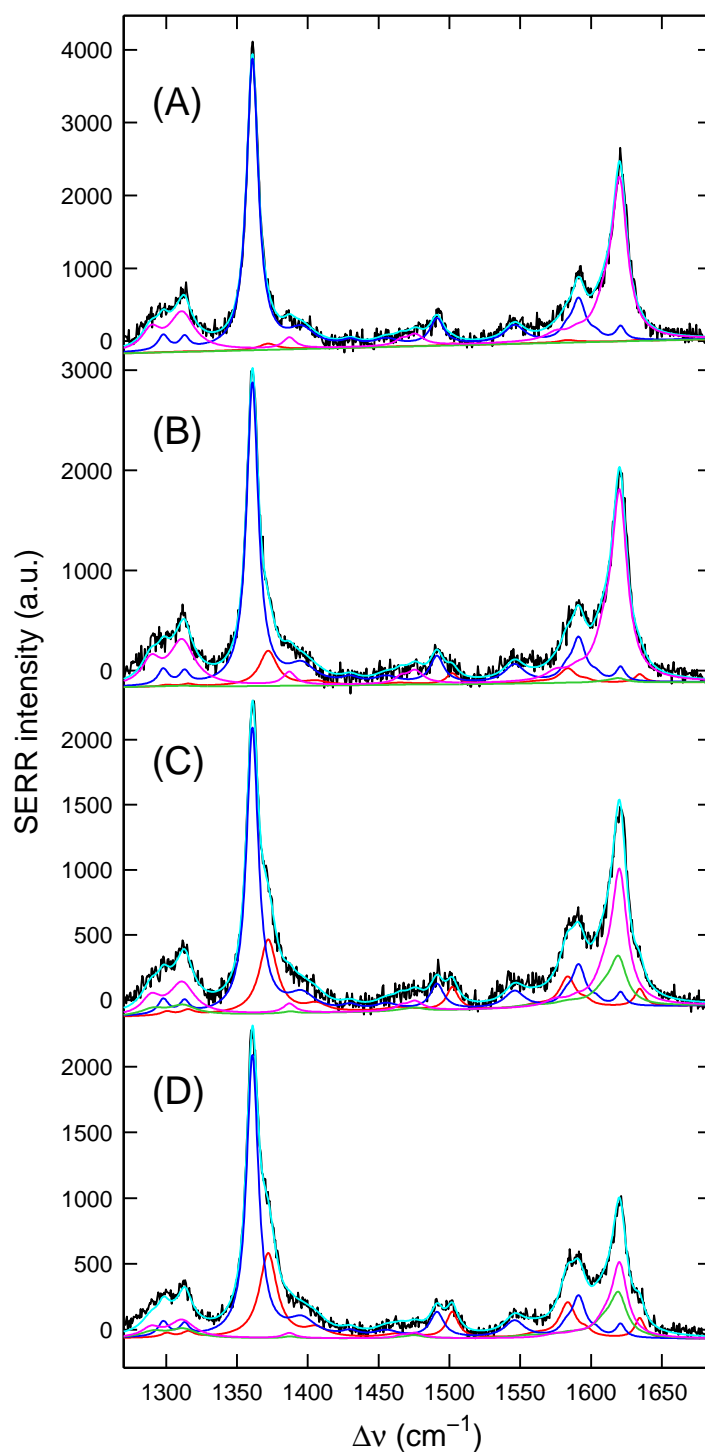


Figure 10.20: Measured TR-SERR spectra and component analysis for a Ag-MUA/MU-Cyt *c*-PASA-Cyt *c* electrode at different delay times δ' after a potential jump from -80 mV to +20 mV for the PASACyt *c* layer assembly. (A) $\delta' = 0$; (B) $\delta' = 21$ ms; (C) $\delta' = 210$ ms and (D) $\delta' = \infty$. Black: experimental spectra, cyan: overall fit, red: Cyt *c* oxidized, blue: Cyt *c* reduced, magenta: PASA 1 and green: PASA 2.

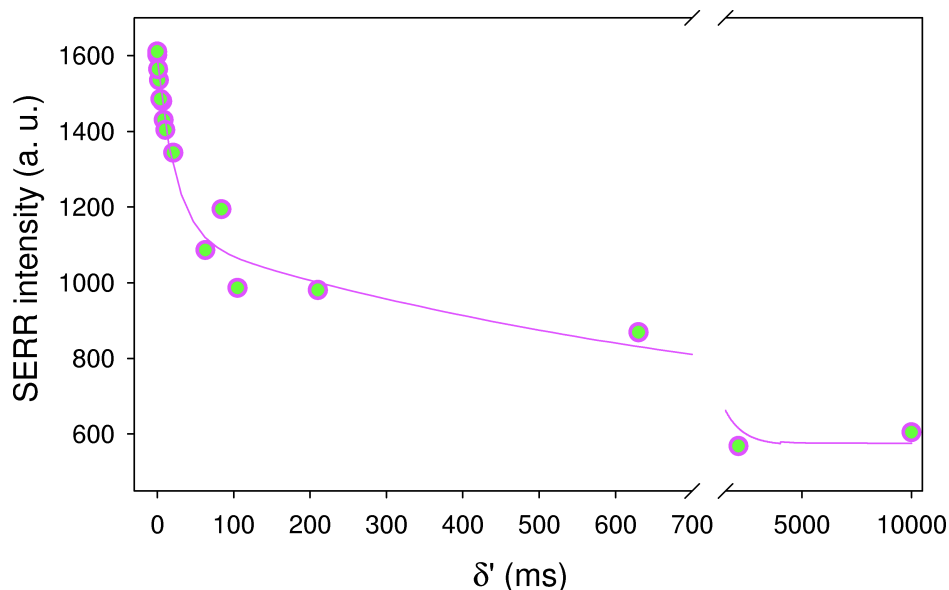


Figure 10.21: Absolute SERR intensity of the PASA 1 spectral contribution for a Ag-MUA/MU-Cyt *c*-PASA-Cyt *c* electrode as a function of the delay time δ' after a potential jump from -80 mV to +20mV.

further on in the second time range. The decay constant of the faster phase is very similar to the Cyt *c* oxidation rate constant both for potential jumps to +25 and +140 mV. No significant acceleration is detected in the slower phase upon applying an overpotential for oxidation. In contrast, TR-SERR investigations of the Ag-MUA/MU-Apo-PASA-Apo system reveal a significantly slower kinetics, which is insensitive to the applied overpotential. The PASA intensity decay in the Ag-MUA/MU-Apo-PASA-Apo assembly occurs on the same time scale as the slower phase of the polyelectrolyte kinetics in the Ag-MUA/MU-Cyt *c*-PASA-Cyt *c* system.

A fraction of PASA in the Ag-MUA/MU-Cyt *c*-PASA-Cyt *c* preparation thus clearly undergoes a redox transition at the rate of Cyt *c* oxidation. This observation is consistent with a mechanism in which the heterogeneous electron transfer is limited by electron tunneling between the electrode and Cyt *c* immobilized on the mixed MUA/MU SAM. The electrostatically adsorbed Cyt *c* molecules then rapidly exchange electrons with the nearby redox centers of the polyelectrolyte. The remaining fraction of PASA redox centers may be oxidized via direct electron transfer to the electrode as suggested by the slower phase in PASA kinetics. The significantly slower kinetics of PASA in the Ag-MUA/MU-Apo-PASA-Apo system is consistent with an increase of the effective electron tunneling distance from the electrode to the polyelec-

trolyte layer bound to the electrostatically adsorbed Apo. Based on SERR measurements of the one layer Ag-MUA/MU-Cyt *c*-PASA-Cyt *c* system, it can thus be argued that PASA facilitates the long range electron transfer through the Ag-MUA/MU-Cyt *c*-(PASA-Cyt *c*)_{*k*} multilayer by offering intermediate redox sites between the individual Cyt *c* molecules and thereby shortening the individual electron transfer steps.

10.6 Summary

Layer-by-layer deposition of the cationic Cyt *c* and anionic PASA produces multilayers of the type Ag-MUA/MU-Cyt *c*-(PASA-Cyt *c*)_{*k*} that are unstable on Ag rough electrodes even after thermal treatment. Desorption of the upper PASA-Cyt *c* adlayers is completed within a few minutes leading to stable Ag-MUA/MU-Cyt *c*-PASA-Cyt *c* electrodes as suggested by the CV response and SERR spectra. Cyt *c* immobilized within this assembly retains its native structure and exhibits a nearly ideal Nernstian behavior. Thermal treatment does not perturb the properties of the adsorbed protein. As inferred from SERR spectroelectrochemistry, the polyelectrolyte undergoes reversible potential-dependent changes, two spectrally different species were identified. Comparison of the redox equilibria and dynamics of Cyt *c* and PASA in Ag-MUA/MU-Cyt *c*-PASA-Cyt *c* and Ag-MUA/MU-Apo-PASA-Apo preparations provides compelling evidence for efficient electron exchange mechanism between the two components, in contrast to the previously proposed protein-protein redox reaction between face-to-face oriented Cyt *c* molecules.^{152,153,154} Therefore it can be concluded from SERR investigations that PASA plays an active role in mediating electronic communication through the different Cyt *c* layers in the PASA-Cyt *c* multilayer assemblies.

Chapter 11

Cytochrome *c* oxidase immobilized on metal electrodes

11.1 Introduction

Electrochemical studies of adsorbed proteins and enzymes afford the opportunity to thoroughly investigate the fundamental parameters which are typical for these biomolecules under controlled conditions.^{4,179} Moreover the complex processes taking place in redox-active proteins and more importantly enzymes provide a high potential for bionanotechnological applications.^{5,180} A key issue has been to attach proteins and enzymes to electrode surfaces without changing their structural integrity and functionality. Immobilization of soluble redox proteins on electrodes is well established and widely applied. Different surface modifications were proposed and successfully employed to examine the electrochemistry of proteins like Cyt *c*.³⁸ Some examples were also shown in the previous chapters of this work.

Far less reports have been published on electrochemistry of membrane proteins despite their central role in fundamental physiological processes. Immobilization of membrane proteins on electrodes remains a challenging task in what it requires the embedment of the protein into a biomimetic system of lipids or lipid analogues. Different strategies have been reported, such as direct adsorption of detergent solubilized protein on electrode surfaces¹⁸¹ or incorporation of enzymes in supported membranes^{182,183} or hybrid bilayers.^{184,185} More recently proteins were embedded in tethered bilayer lipid membranes developed to address the necessity of submembrane space.^{186,187} In tethered membranes, the lipid bilayer is attached to the electrode surface via special chemical anchors which contain a thiol group on one side and have an affinity for the bilayer on the other side. Cytochrome *c* oxidase, a structurally,

functionally and spectroscopically well characterized membrane-bound enzyme,^{39,41,43,50} has become an important test case for adapting electrode surfaces to membrane proteins.^{184,185,186,188}

A novel immobilization strategy based on the tethered bilayer lipid membrane method combined with the principle of metal ion affinity chromatography¹⁸⁹ was used in this work to immobilize CcO from *Rhodobacter sphaeroides*.⁹⁶ The anchoring group of the bilayer is the enzyme itself that is attached to the electrode via interaction of an engineered histidine-tag with a metal ion chelating surface coating. Various His-tagged proteins were shown to selectively adsorb to nitrilo-triacetic acid (NTA) modified electrodes by formation of chelate complexes with transition metal ions (typically Ni^{2+} , Zn^{2+} , Co^{2+} or Cu^{2+}).^{190,191,192,193,194,195,196} CcO is immobilized in the detergent solubilized form and the detergent is subsequently replaced by phospholipids to reconstitute a quasi-natural membrane environment.^{96,197}

Immobilization of CcO via interaction of a Ni-NTA modified Ag surface with histidines fused to subunit I or II of the protein allows to study the enzyme in two different orientations: one with the binding domain for the natural electron donor Cyt *c* pointing to the solution phase (CcO-I) and the other with the binding domain facing the electrode (CcO-II).

A major part of the results presented in this chapter was published in two papers; the conclusions of the first one are unfortunately distorted by the problem of photoreduction,⁹⁷ the second one provides a detailed description of the spectroelectrochemical behavior of the immobilized CcO under optimized experimental conditions.¹⁹⁸

11.2 Formation of the Ni-NTA SAM monitored by SEIRA

The complete immobilization procedure including the original two step preparation of the NTA SAM, activation with Ni^{2+} , protein attachment and replacement of the detergent by phospholipids to reconstitute a quasi-natural environment was closely followed by surface plasmon resonance and electrochemical impedance spectroscopy measurements⁹⁶, surface-enhanced infrared spectroscopy^{197,199} and scanning probe microscopy²⁰⁰.

The initially employed two step surface modification was simplified by a commercially available NTA terminated thiol compound. The functionality of this new SAM was first validated with the help of surface-enhanced infrared absorption (SEIRA) spectroscopy. As SEIRA was not the principal experimental method used within this work, its principle is not detailed here

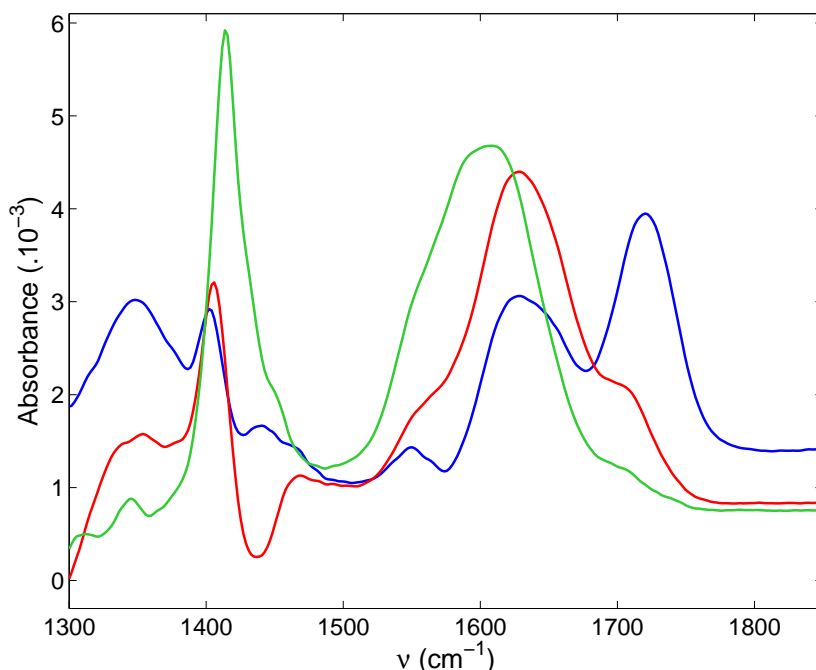


Figure 11.1: SEIRA spectra acquired at different steps of the formation of the Ni-NTA SAM. Blue: NTA after 2 hours of self-assembly from an aqueous solution of dithiobis(C2-NTA) (pH 3); red: NTA SAM in a buffer solution (10 mM phosphate) of pH 7.0; green: Ni-NTA SAM in a buffer solution (10 mM phosphate) of pH 7.0.

and can be found elsewhere.²⁰¹

The gold layer on the ATR silicon prism was formed by electroless deposition,²⁰² the preparation procedure is described elsewhere.⁶⁹ SEIRA spectra were recorded with a IFS66v/s Bruker spectrometer. The ATR crystal coated with the Au film was mounted in the measurement cell and covered with 1 mL of a buffer solution (10 mM phosphate buffer, pH 7.0). The sample chamber of the spectrometer was flushed with nitrogen to guarantee a stable atmosphere. After ca. 1 hour of stabilization, a background spectrum of the buffer was acquired. The buffer was then exchanged with a 1 mM aqueous solution of dithiobis(C2-NTA) and the self-assembly process of the thiol compound on the Au film was monitored. Dithiobis(C2-NTA) is delivered in a dihydrochloride form, self-assembly proceeds thus in a solution of pH 3.

Figure 11.1 (blue trace) shows a SEIRA spectrum of the NTA layer after 2 hours of self-assembly. The most prominent peak at 1720 cm^{-1} is assigned to the stretching mode of the protonated carboxyl groups (ν^{COOH}). The

high portion of protonated carboxyl groups is consistent with the pH 3 of the solution from which the self-assembly proceeds. The symmetric (ν_{sym}) and asymmetric (ν_{asym}) stretching vibrations of the carboxylate groups are observed at 1402 and 1630 cm^{-1} respectively. Moreover, the broad band at 1630 cm^{-1} contains the amide I contribution from the amide bond in the SAM chain. The small peak at 1550 cm^{-1} is ascribed to the amide II vibration.

No pronounced changes were detected in the SEIRA spectra after 2 hours of self-assembly, the process was therefore stopped and the acidic solution containing dithiobis(C2-NTA) was replaced by a buffer solution (10 mM phosphate) of pH 7.0. The changes observed in the spectra (Figure 11.1 red trace), namely the intensity increase of ν_{sym} and ν_{asym} , correspond to an important deprotonation of the carboxylic acid groups.

The measurement cell was subsequently filled with a 40 mM NiCl_2 solution (50 mM acetate buffer, pH 5.5) in order to form the Ni-NTA hexagonal complex on the Au surface. SEIRA spectra of NTA and Ni-NTA SAM are compared in Figure 11.1 (red trace and green trace). Ni^{2+} complexation is accompanied by a further broadening and a downshift of the band assigned originally to ν_{asym} , which can be interpreted by the appearance of a new mode at ca. 1595 cm^{-1} . This band has been attributed to the asymmetric stretching vibration of the nickel-complexed carboxylate group.²⁰³ Furthermore, a frequency upshift of the ν_{sym} mode to 1415 cm^{-1} is in agreement with the spectral changes of the uncomplexed carboxylate peak.²⁰³

The employed procedure results thus in the formation of a Ni-NTA monolayer on the electrode surface. Therefore it can be concluded that both surface modification protocols yield similar electrode coatings.

11.3 Photoreduction

The experimental work, which led to the first publication, was conducted on the immobilized CcO-II variant of the enzyme. The NTA surface modification was realized by the two step procedure as described in Section 6.2.3. The potential dependent measurements were performed in a prototype of the flat electrochemical cell similar to that shown in Figure 5.3. This cell was however not compatible with the immersion objective and did not allow for an efficient rotation of the electrode with respect to the incident laser beam. Fast electron transfer between CcO-II and Ag electrode was reported.⁹⁷

SERR spectra of CcO-II immobilized on disk Ag electrodes display relatively intense signals of hemes *a* and *a*₃ despite their large separation from the metal surface which are in the order of 50 Å (see Figure 11.2 and 6.6).

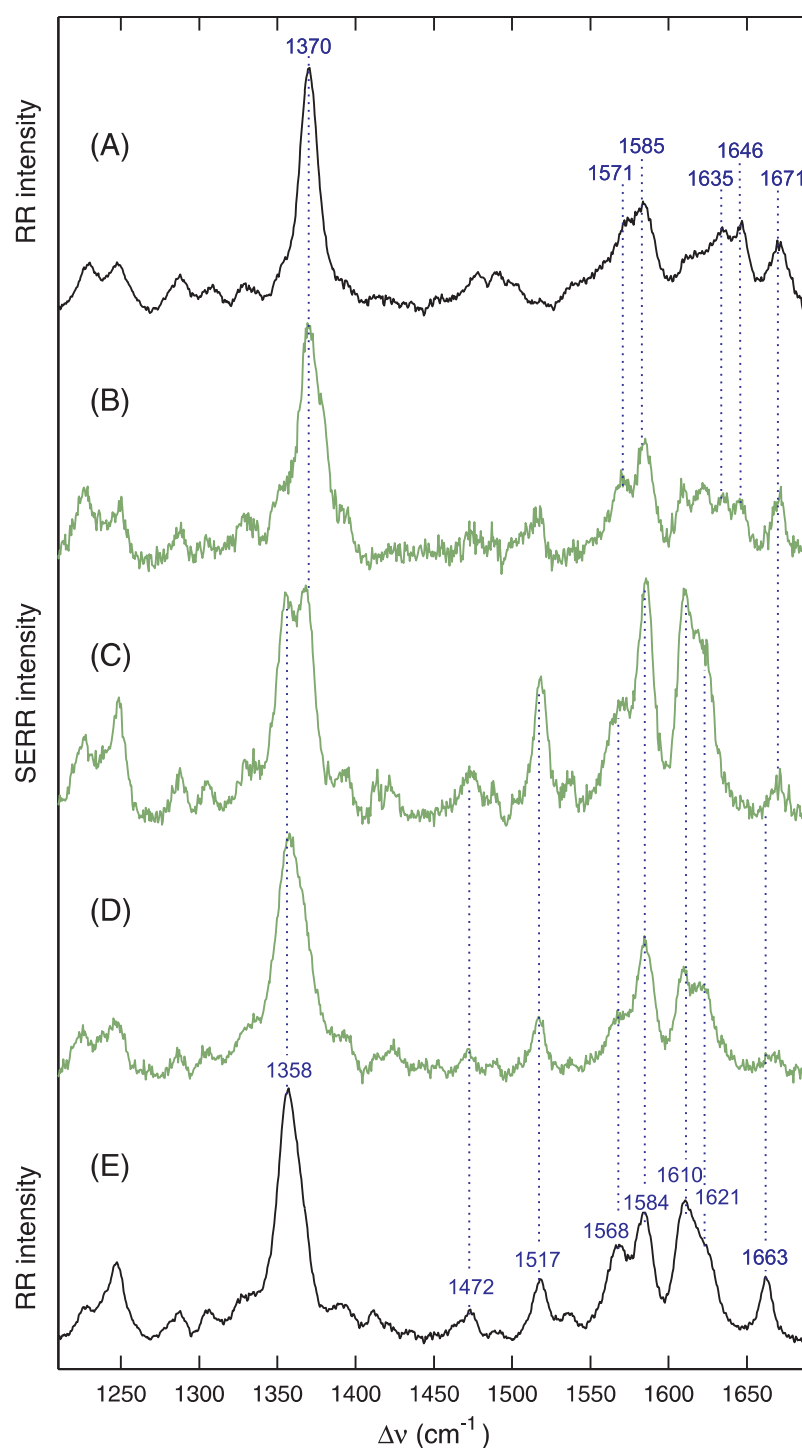


Figure 11.2: SERR spectra of CcO-II tethered to a Ni-NTA functionalized Ag disk electrode and reconstituted in a lipid membrane, measured at (B) open circuit, (C) -0.4 V and (D) -0.65 V, compared with the RR spectra of CcOin solution, (A) in the fully oxidized and (E) dithionite-reduced form.

A comparison of spectra (A), (B) and (C) in Figure 11.2 reveals that the spectrum recorded at open circuit is largely dominated by the characteristic bands of the oxidized enzyme but includes a minor contribution of ferrous heme *a*. Specifically, the shoulder at 1358 cm^{-1} on the low-frequency side of the prominent ν_4 band as well as the concomitant appearance of the 1517-cm^{-1} and 1611-cm^{-1} bands are representative for reduced heme *a*. Both hemes are gradually reduced upon lowering the electrode potential to reach full reduction at ca. -0.65 V . At this very negative potential, the SERR spectrum shows a good agreement with the RR vibrational pattern of fully reduced CcO in solution, although some differences can be identified. The most notable one refers to the extremely low intensity of the formyl stretching mode of heme *a*₃ at 1663 cm^{-1} (compare spectra (D) and (E) in Figure 11.2).

The immobilized CcO-II can be reduced and partly re-oxidized by varying the electrode potential, the heme *a* remains however largely reduced. In fact, Figure 11.2 (B) displays the highest degree of oxidation achieved; moreover, the amount of oxidized heme *a* at open circuit and potentials above -0.1 V was not well reproducible between different measurements. On the other hand, the reduction extent below ca. -0.1 V was comparable in all experiments. The enzyme responds very fast to the applied potential as the observed redox changes occur in the 1 minute equilibration time. This is a rather surprising observation if we take into account the considerable electron transfer distance from the electrode to the primary electron acceptor Cu_A, which is larger than 40 \AA .

With the new experimental setup, described in Section 5.1.2, it was possible to better control the extent of photoreduction. However, it was quite difficult to avoid photoreduction completely. The power was decreased to 0.1 mW , the electrochemical cell was rotated at ca. 2 Hz and the exposure of the immobilized enzyme to laser radiation was minimized by using short accumulation times. In order to improve the signal-to-noise ratio, several short spectra acquisitions (typically 20 s) were performed from different spots on the electrode and subsequently summed up.

In Figure 11.3, SERR spectra of immobilized CcO-I measured at open circuit under different irradiation conditions are compared to fully oxidized and fully reduced RR spectra. At a laser power of 0.1 mW focused onto the same spot of the electrode surface (no cell rotation, Figure 11.3 (B)), the population of reduced hemes is relatively high as indicated by the intensity ratio of the ν_4 modes. Moving the electrode with respect to the laser beam drastically lowers photoreduction, so that the spectrum acquired at a higher laser power (0.3 mW) but with a rotating cell reflects only a small amount of reduced hemes (Figure 11.3 (C)). Lowering the power to 0.1 mW while rotating the cell makes it possible to obtain spectra of fully oxidized

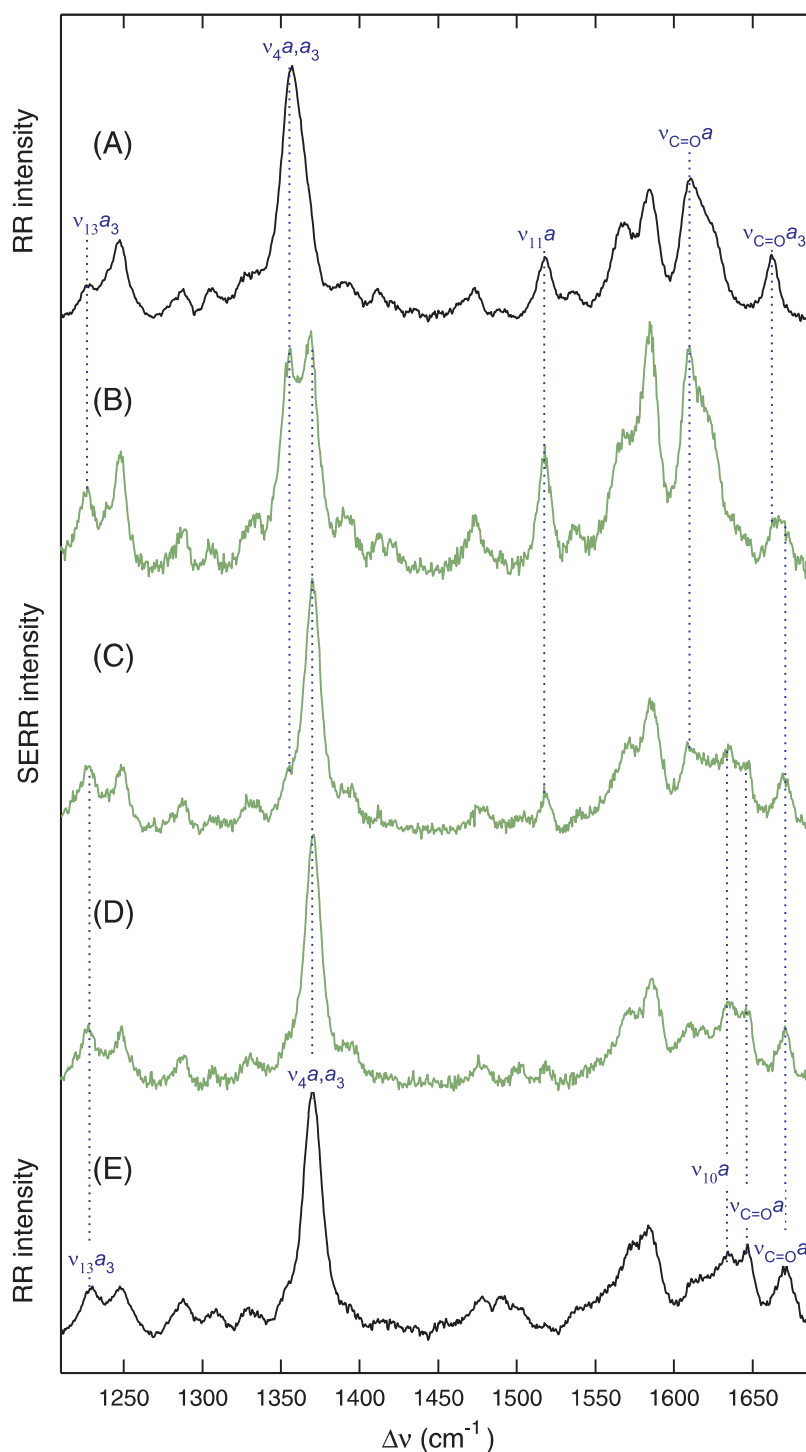


Figure 11.3: SERR spectra of CcO-I tethered to a Ni-NTA functionalized Ag disk electrode and reconstituted in a lipid membrane measured at open circuit (B, C, D), compared with the RR spectra of CcO in solution, (A) in the fully reduced and (E) fully oxidized form. The SERR spectra were acquired using different excitation conditions: (B) 0.1 mW, stationary electrode; (C) 0.3 mW, rotating electrode and (D) 0.1 mW, rotating electrode.

CcO (Figure 11.3 (D)).

The photoreduction occurs first at heme *a* as indicated by the appearance of the ν_{11} band at 1517 cm^{-1} and by the intensity increase of the C=O stretching mode at 1610 cm^{-1} in the slightly photoreduced spectrum (Figure 11.3 (C)), both modes are characteristic for the reduced heme *a*. Heme *a* seems to be fully reduced under strongly photoreductive conditions (Figure 11.3 (B)) as suggested by the intensity increase of the 1517 cm^{-1} band and the disappearance of the ν_{11} and $\nu_{\text{C=O}}$ modes at 1635 and 1646 cm^{-1} respectively which are attributed to the oxidized heme *a*. Furthermore, heme *a*₃ appears to be in a mixture of oxidized and reduced form since the C=O stretching region of heme *a*₃ displays the corresponding bands at 1671 and 1663 cm^{-1} with nearly equal intensity.

Photoreduction of the immobilized CcO occurs very easily. It was reported earlier that heme proteins can be photoreduced in the absence of external electron donors by irradiation with UV or visible light. Photoreduction was extensively investigated for example for metmyoglobin, cytochrome *c*, cytochrome *b*₅, heme octapeptide and cytochrome P450.²⁰⁴ The facile photoreduction of CcO complicated RR measurements of the enzyme in solution in the fully oxidized state throughout the first years of investigation.^{205,206,207,208} Finally, it could be avoided by using lower laser powers and moving the sample. Nowadays, photoreduction is positively employed as a very fast reduction technique in structural studies of heme-copper oxidases.²⁰⁹ Despite numerous studies, the exact mechanism of photoreduction, and above all the origin of the additional electron, is not known.

In the SERR experiment, the photoreduction process is likely to be more efficient than in solution since the interactions of the radiation field with the surface plasmons of the metal do not only enhance the RR scattering but also all other photophysical processes.²³ As shown in Figure 11.3, reliable indicators of fully oxidized enzyme are the absence of the 1517 cm^{-1} band and the relative intensity pattern of the modes in the region $1600 - 1650\text{ cm}^{-1}$. Photoreduction starts at heme *a* and proceeds to heme *a*₃ under higher laser power. Further increase of the power induces a chemical modification of heme *a*₃ as indicated by the disappearance of the $\nu_{\text{C=O}}$ mode. The initial observation of a fast reduction rate of the immobilized CcO was confirmed, rates faster than 1 min^{-1} were determined under only slightly photoreductive conditions (0.3 mW, rotating cell, photoreduction extent at open circuit corresponds to Figure 11.3 (C)).

11.4 Different modes of CcO immobilization

Immobilized CcO-I and CcO-II give rise to indistinguishable SERR spectra. Indeed, subtraction of SERR spectra corresponding to CcO-I and CcO-II measured at the same potential and under identical conditions yields a difference spectrum with no negative or positive peaks. Moreover, SERR absolute intensities are comparable for CcO binding via the His-tag attached to subunit I or II. This observation is in agreement with the fact that both modes of CcO immobilization correspond approximately to the same distance and orientation of the two hemes with respect to the electrode surface (see Figure 6.6).

The exchange of Ni^{2+} by Zn^{2+} as the coordination metal ion between His-tag and NTA does not affect CcO SERR spectra in the potential range from -0.65 to +0.0 V and has no detectable influence on the redox behavior. However, the Zn-NTA complex is electrochemically inert in a wider potential range than Ni-NTA.^{210,211} Zn^{2+} was therefore used for potential-dependent measurements of CcO below -0.65 V.

11.5 Redox equilibrium and reduction dynamics of immobilized CcO

The redox equilibrium and reduction dynamics of adsorbed CcO-I and CcO-II protein variants were investigated by potential-dependent SERR spectroscopy under different conditions, namely, under anaerobic conditions for CcO immobilized via Ni-NTA and Zn-NTA at extreme potentials, under aerobic conditions and finally for the CN inhibited enzyme. SERR spectra were acquired at low laser powers (0.1 mW) and high rotational frequency of the electrochemical cell (ca. 2 Hz) to minimize photoreduction. A minimum of three acquisitions of 20 s were performed at each potential and summed up in order to improve the signal-to-noise ratio.

Nevertheless, the present spectral quality did not allow for a complete component analysis as employed in the case of Cyt *c*. At least four component spectra (reduced and oxidized hemes *a* and *a*₃) would have to be considered in the band fitting procedure. Their determination is aggravated by the strong spectral overlap of the porphyrin modes, particularly in the region between 1530 and 1650 cm^{-1} . Therefore, the quantitative analysis was based only on the relative intensities of the two ν_4 bands (reduced and oxidized). This treatment systematically underestimates the relative concentration of the reduced hemes for which the resonance enhancement at 413 nm is lower than for the oxidized hemes. Relative cross section factors for the two hemes in the

oxidized and reduced state were determined on the basis of RR spectra of the enzyme in solution. The factors were calculated from the absolute intensities of the well separated formyl stretching modes yielding $f_{\text{ox}} = 1$, $f_{\text{red}} = 0.38$ for heme *a* and $f_{\text{ox}} = 1$, $f_{\text{red}} = 0.27$. For comparison, the cross section factors of heme *c* in Cyt *c* were found to be $f_{\text{ox}} = 1$, $f_{\text{red}} = 0.28$. However, the relative intensities of the ν_4 bands cannot be converted to relative concentrations in a straightforward manner since the two hemes are likely to contribute to the ν_4 envelope in an unequal way.

11.5.1 Anaerobic conditions

Potential induced changes in the CcO SERR spectra were followed after careful purging the solution with Ar for at least one hour and upon maintaining an Ar overpressure in the rotating electrochemical cell during the experiments. First observations revealed that potential-dependent changes in the CcO spectra occurred very slowly. Equilibration times of at least 20 minutes at a given potential were therefore required before the accumulation of a stationary SERR spectrum could be initiated. SERR spectra of adsorbed CcO-I acquired under these conditions are displayed in Figure 11.4 for three different potentials. At 0.0 V, the SERR spectrum displays the signature of a nearly fully oxidized CcO. A band fitting analysis of the ν_4 envelope reveals a spectral contribution of the reduced form of the enzyme lower than 5% at this potential. Decreasing the potential leads to an increase of the reduced form to 22% at -0.4 V and 39% at -0.65 V (Figure 11.5(a)). Data in Figure 11.5(a) represent the average values of several measurements from different electrodes. No differences could be identified between the two orientations of adsorbed CcO, data originating both from immobilized CcO-I and CcO-II are included in Figure 11.5(a).

The analysis of the ν_4 envelope only provides information about the total amount of reduced hemes, a closer inspection of the different marker bands indicates moreover that it is primarily heme *a* that is reduced with decreasing potential. As depicted in Figure 11.4, the $\nu_{\text{C=O}}$ mode of heme *a*₃ at 1671 cm⁻¹ remains largely unchanged at negative potentials whereas the same mode of heme *a* at 1646 cm⁻¹ gradually disappears. The absence of this latter band at -0.65 V implies that at this potential heme *a* is completely reduced. This conclusion goes in line with the intensity increase of the 1517-cm⁻¹ ν_{11} mode corresponding to ferrous heme *a*.

The very slow redox process enables to follow the reduction dynamics simply by monitoring the time evolution of the potential-induced changes after a change in potential in the time scale of minutes. To estimate the rate of electron transfer from the electrode to heme *a*, the electrode potential was

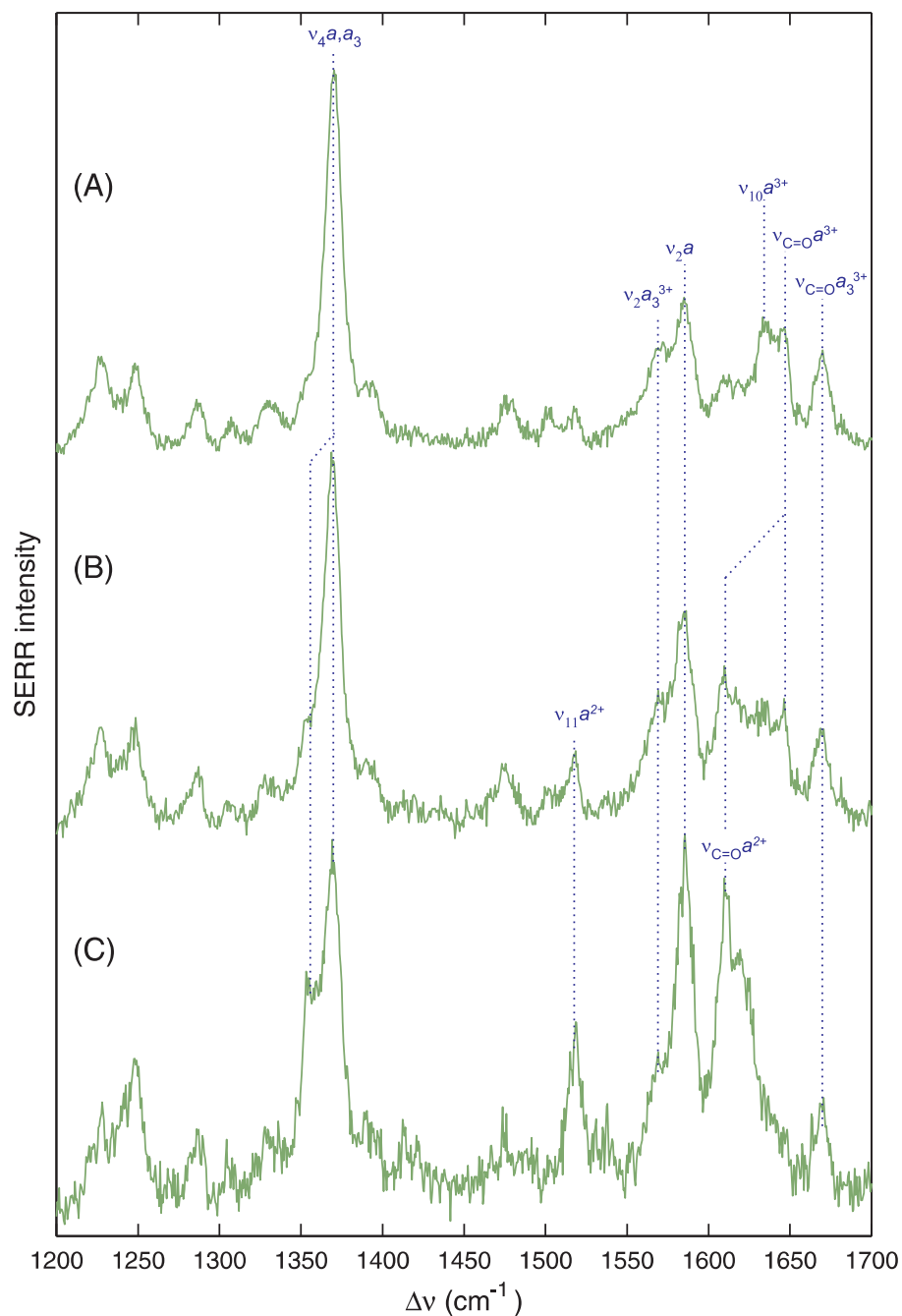


Figure 11.4: SERR spectra of immobilized CcO-I using a rotating electrochemical cell and a laser power of 0.1 mW under anaerobic conditions at different potentials: (A) 0.0 V, (B) -0.2 V and (C) -0.65 V.

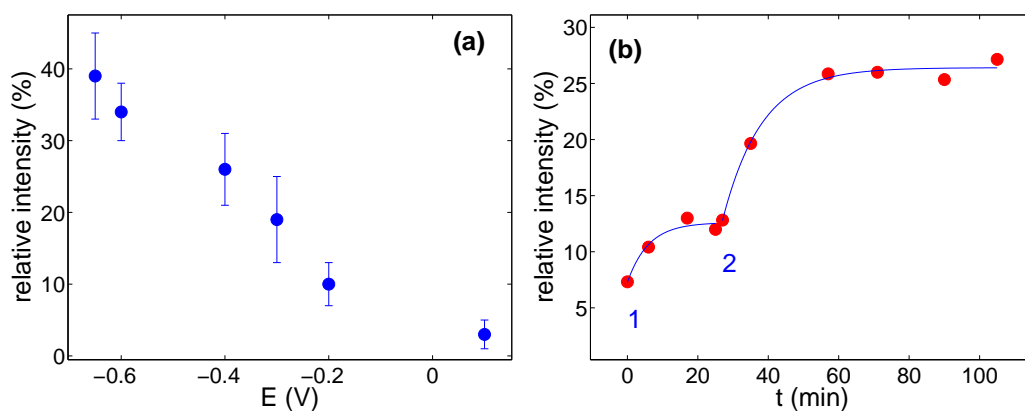


Figure 11.5: Redox equilibria and kinetics of immobilized CcO under anaerobic conditions determined from the ν_4 band intensities of the SERR spectra: (a) equilibrium relative spectral contributions of the reduced species as a function of electrode potential (each point corresponds to an average of at least two independent measurements); (b) changes of the spectral contributions of the reduced hemes following a potential jump (1) from open circuit (ca. +0.1 V) to -0.2 V and (2) from -0.2 V to -0.4 V.

changed from open circuit (ca. +0.1 V) to -0.2 V and SERR spectra were acquired at different delay times after potential jump. Quantitative analysis of the measured spectra reveals a time-dependent reduction which can be approximated by a single exponential function yielding a rate constant of $0.0020 \pm 0.0005 \text{ s}^{-1}$ for heme *a* reduction (Figure 11.5(b)). The subsequent potential jump to -0.4 V leads to a further increase of the reduced species albeit with the same rate (0.002 s^{-1}). Several potential jumps with different initial and final potentials were performed resulting within the experimental error in the same rate constant for reduction. Moreover, experiments with CcO-I and CcO-II show essentially the same picture both with respect to the degree and rate of reduction.

As full reduction of the enzyme was not possible even at -0.65 V, Ni-NTA was thus exchanged by Zn-NTA in the immobilization procedure in order to extend the accessible potential range to more negative potential values. While down to -0.65 V, reduction appears to be largely restricted to heme *a*, a further decrease of electrode potential leads to an increase of the contribution of the ferrous heme *a*₃. The underlying spectral changes, however, point to other chemical processes in addition to the reduction of this cofactor, as suggested by the comparison of SERR spectra at two extremely negative potentials with the RR spectrum of the native enzyme in the fully reduced state in Figure 11.6. Specifically, we note a substantial intensity

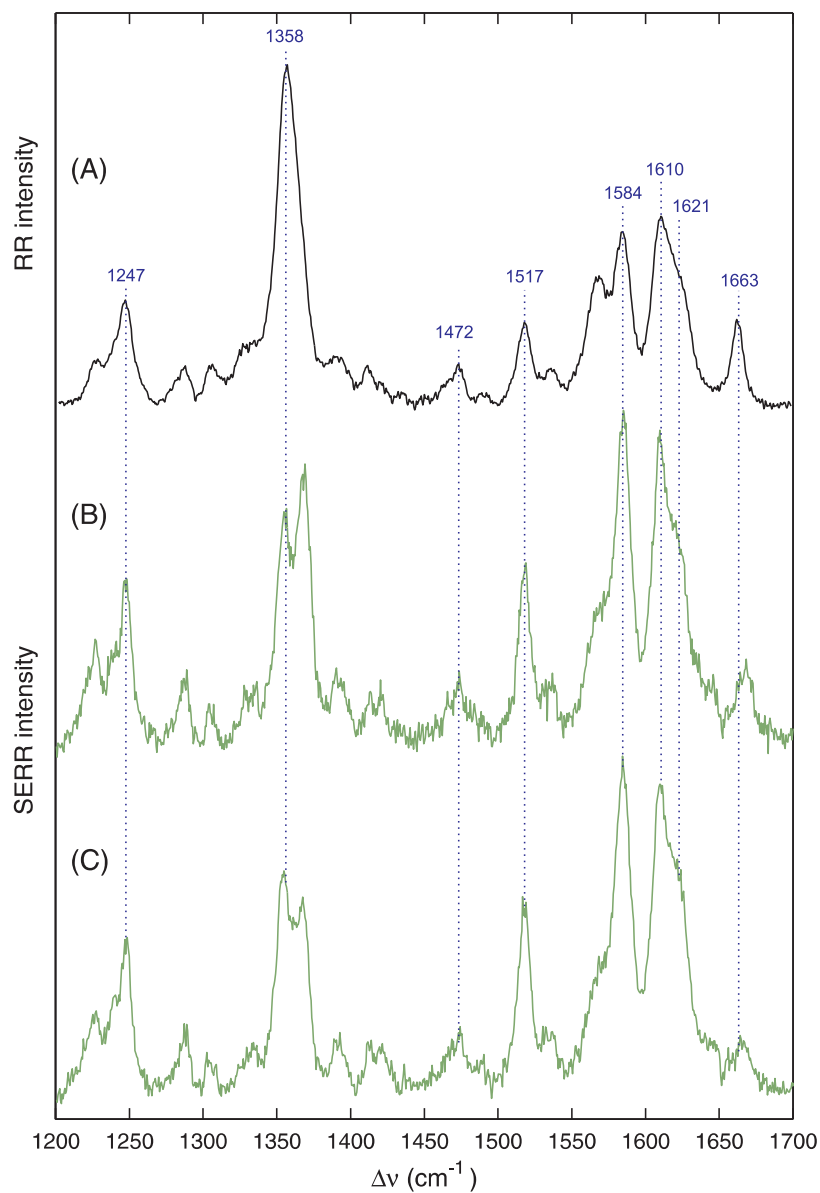


Figure 11.6: SERR spectra of immobilized CcO using a rotating electrochemical cell and a laser power of 0.1 mW under anaerobic conditions at different potentials: (B) -0.8 V, (C) -1.1 V; compared to (A) the RR spectrum of fully reduced CcO in solution.

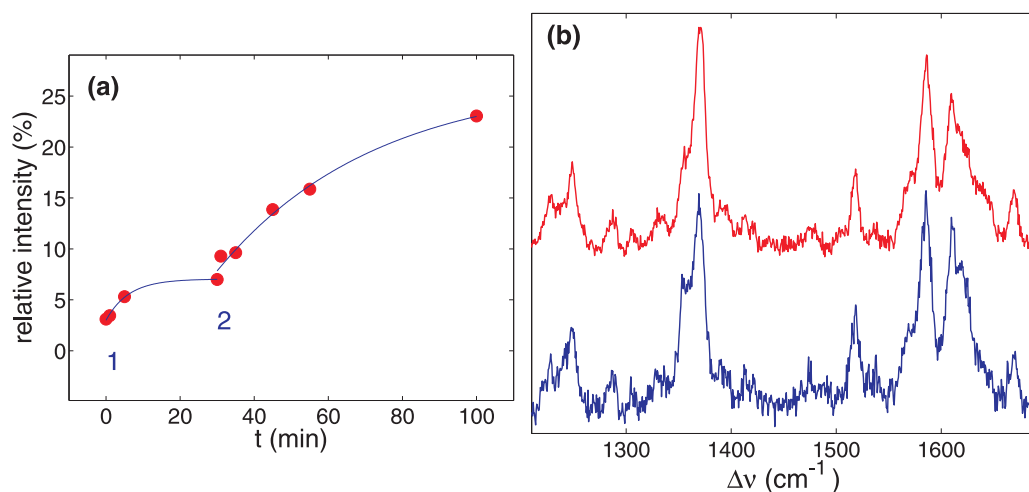


Figure 11.7: Redox equilibria and kinetics of immobilized CcO under aerobic conditions: (a) changes of the spectral contributions of the reduced hemes as determined from the ν_4 band intensities in the SERR spectra following a potential jump (1) from open circuit (ca. +0.1 V) to -0.4 V and (2) from -0.4 V to -0.6 V; (b) stationary SERR spectra at -0.65 V under aerobic (red) and anaerobic (blue) conditions.

decrease of the ν_4 bands and of the heme a_3 formyl stretching mode relative to the bands at 1247, 1517, 1584 and 1610 cm^{-1} . The CcO signal vanishes at -1.5 V presumably due to the reductive desorption of the SAM.

11.5.2 Aerobic conditions

Control potential-dependent measurements of immobilized CcO were performed in normal air atmosphere. The experiments reveal a qualitatively similar picture as under anaerobic conditions since formation of the ferrous heme a is observed. Reduction of heme a following a potential jump from open circuit to -0.4 V and subsequently to -0.6 V occurs at similar rate constants as under anaerobic conditions (Figure 11.7(a)). The extent of reduction under aerobic conditions is however significantly lower than in the anaerobic case. Whereas under anaerobic conditions, the amount of reduced hemes attains 22% and 39% at -0.4 V and -0.65 V respectively, in the presence of oxygen the respective spectral contributions do not exceed 10% and 25% (compare the reduction extent in the SERR spectra at -0.65 V for aerobic and anaerobic conditions in Figure 11.7(b)).

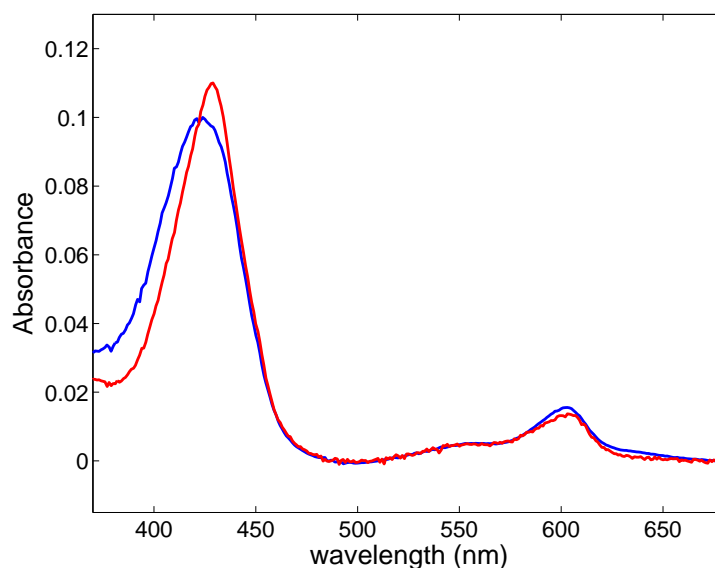


Figure 11.8: UV-vis absorption spectra of the fully oxidized CcO (blue) and $CcO(CN)$ (red) ($5\ \mu M$ CcO in a 50 mM phosphate buffer of pH 8.0 with 0.1% DDM, 1 mM NaCN).

11.5.3 CN inhibited CcO

Cyanide binding to solubilized CcO has been extensively studied previously using UV-vis absorption as well as FTIR and RR spectroscopy.^{208,212,213,214,215,216,217,218,219} Cyanide was shown to occupy the position of the sixth axial ligand in heme a_3 and block it in the ferric form. The turn-over of the enzyme is thereby inhibited. The transition from a 6cHS to a 6cLS species upon cyanide binding is accompanied by a blue shift of the Soret absorption peak^{213,215} and by minor changes in vibrational heme modes especially in the low frequency spectral region.^{214,217} FTIR investigations revealed a $C\equiv N$ stretching vibration at 2150 cm^{-1} which indicates that the cyanide ligand is coordinated as an $Fe^{3+}-C\equiv N-Cu_B^{2+}$ species.^{220,221}

To immobilize the fully oxidized cyanide complex of CcO ($CcO(CN)$), the enzyme was incubated with a 200-fold excess of NaCN for 1 hour prior to immobilization. Formation of the $CcO(CN)$ adduct under these conditions was confirmed by UV-vis absorption spectroscopy. As shown in Figure 11.8, the Soret maximum of the fully oxidized enzyme shifts from 421 to 428 nm after CN addition in agreement with literature data.^{213,215} Excess of cyanide was maintained in all solutions during the individual steps of the immobilization procedure as well as during the experiments. Open circuit potential of the modified electrode decreases by almost 0.2 V to -0.1 V.

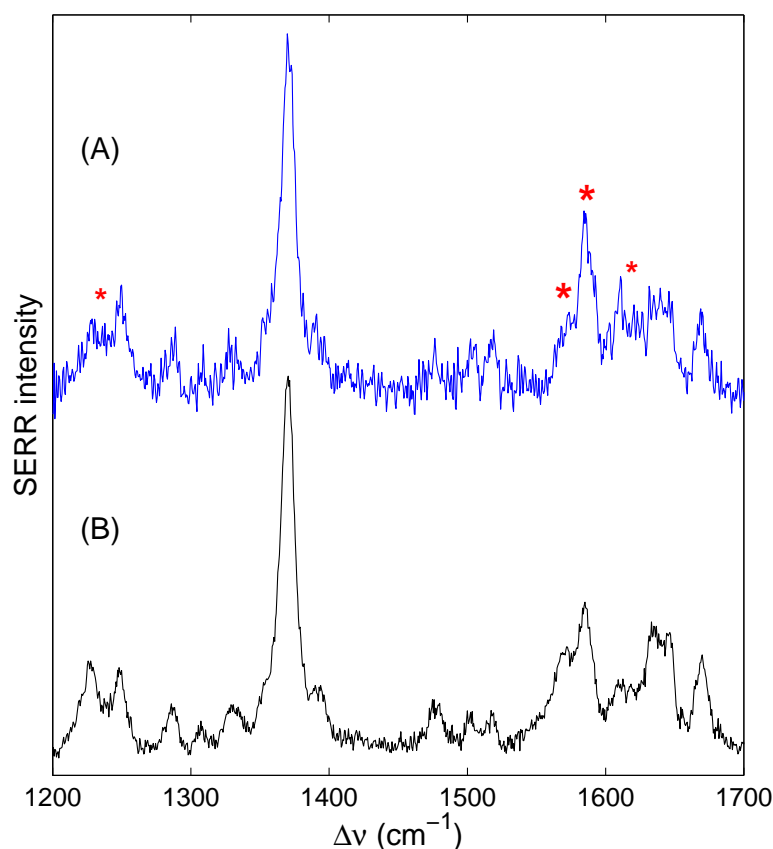


Figure 11.9: SERR spectra of immobilized CcO-I using a rotating electrochemical cell and a laser power of 0.1 mW at +0.1 V: (A) CN inhibited enzyme compared to (B) the fully oxidized CcO under anaerobic conditions. The spectral changes in CcO(CN) are marked by a red asterisk.

SERR spectra of the immobilized CcO(CN) were carefully examined in order to confirm cyanide ligation also in the immobilized enzyme. Cyanide binding to the Fe atom of heme a_3 gives rise to characteristic stretching and bending isotope-sensitive modes Raman active below 500 cm^{-1} .^{214,217} These bands are however too weak to be resolved in the measured SERR spectra due to unfavorable signal-to-noise ratio.

Other spectral changes, although relatively small, are readily observable in the high frequency region as can be inferred from Figure 11.9. They are characteristic for the transition of heme a_3 from the 6cHS to the 6cLS configuration and are in perfect agreement with previous findings for solubilized bovine CcO.²¹⁵ Specifically, the spectral changes refer mainly to the intensity increase at 1585 cm^{-1} at the expense of the 1571 cm^{-1} band, reflecting the

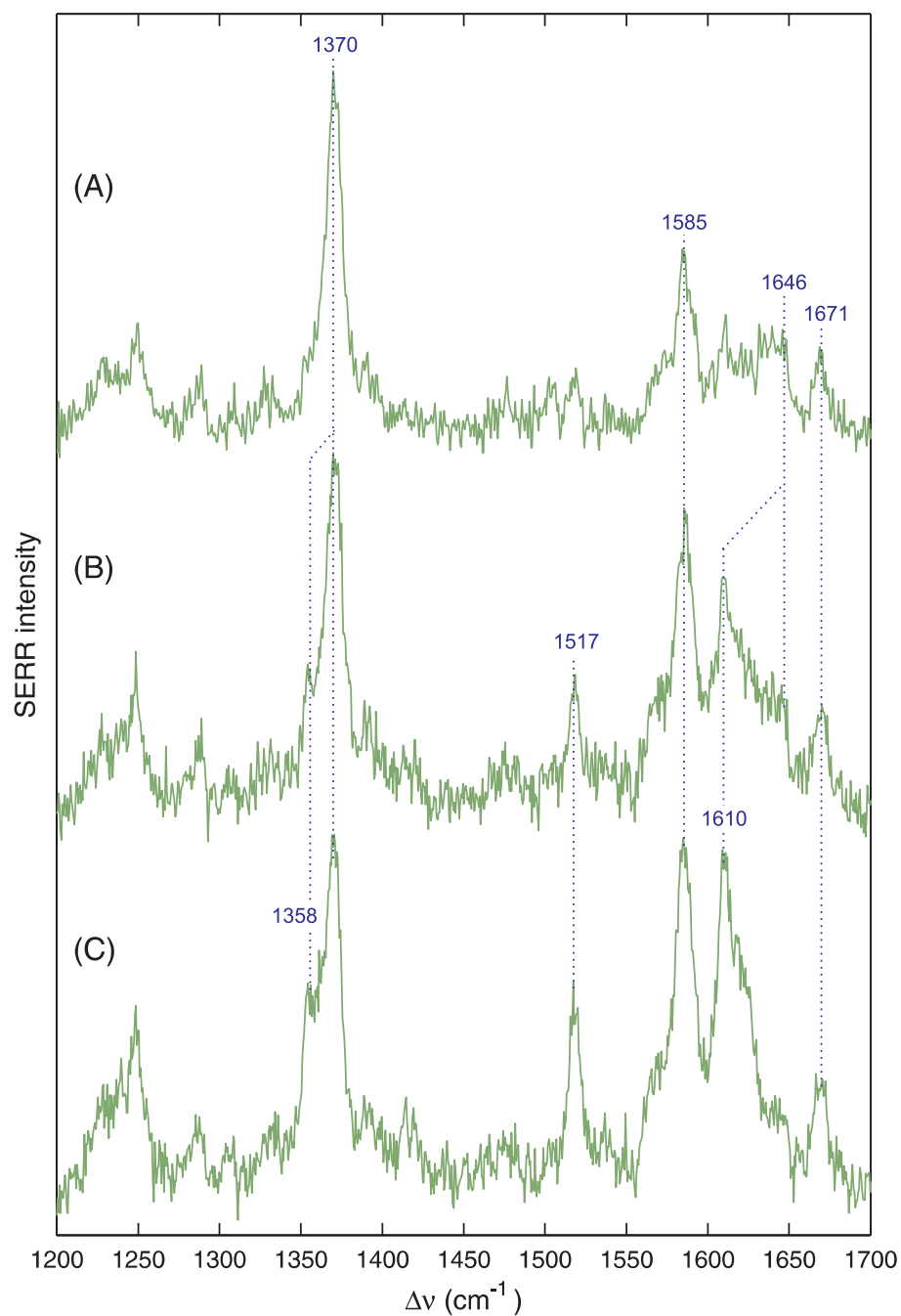


Figure 11.10: SERR spectra of immobilized CcO(CN) using a rotating electrochemical cell and a laser power of 0.1 mW at different potentials: (A) -0.1 V, (B) -0.3 V and (C) -0.6 V.

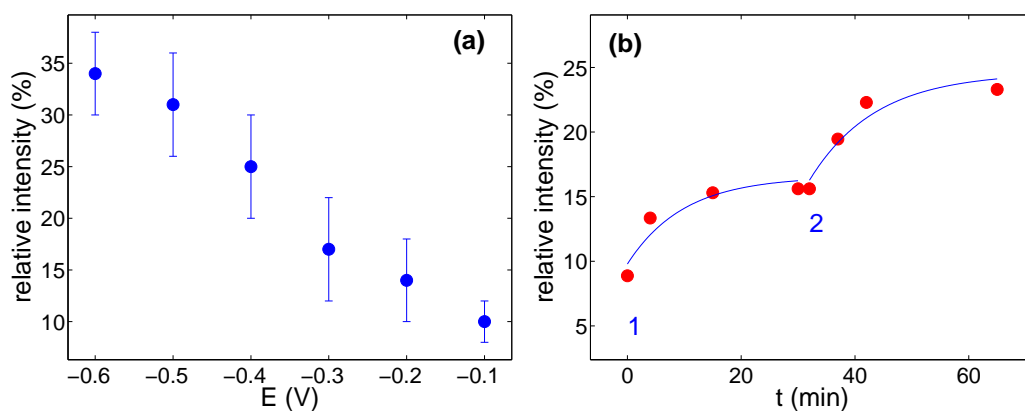


Figure 11.11: Redox equilibria and kinetics of immobilized CN inhibited CcO under aerobic conditions determined from the ν_4 band intensities of the SERR spectra: (a) equilibrium relative spectral contributions of the reduced species as a function of electrode potential (each point corresponds to an average of at least two independent measurements); (b) changes of the spectral contributions of the reduced hemes following a potential jump (1) from open circuit (ca. -0.1 V) to -0.3 V and (2) from -0.3 V to -0.4 V.

expected ca. 15 cm^{-1} frequency upshift of the ν_2 band of heme a_3 associated with the spin state change. Minor changes concern the additional intensity at 1614 cm^{-1} and changes in the doublet at 1226 and 1248 cm^{-1} . On the other hand, the formyl stretching and the ν_4 modes as well as heme a spectral contribution remain unaffected, the same marker bands can be thus used for analyzing the redox transition as in the case of the cyanide-free enzyme.

The SERR spectra of CcO(CN) acquired under non-photoreductive conditions reflect an increasing spectral contribution of the reduced species upon lowering the potential as indicated by the intensity redistribution of the ν_4 envelope (Figure 11.10). The concomitant intensity increase of the 1517 cm^{-1} and the preservation of the formyl stretching at 1671 cm^{-1} imply that reduction is restricted to heme a . At -0.6 V, the total amount of reduced hemes, expressed in terms of the ν_4 relative intensities, appears to reach a maximum value of ca. 35% (see Figure 11.11(a)). The potential-dependent intensity profile displays the same tendency as that found for immobilized CcO under anaerobic conditions. The rate constant of reduction (0.002 s^{-1}) also coincides with the value determined in the anaerobic case, as illustrated in Figure 11.11(b) for a potential jump from open circuit to -0.3 V and subsequently to -0.4 V. Again no differences were found for cyanide complexes of CcO-I and CcO-II.

11.6 Discussion

11.6.1 Long distance electron transfer

Fast electron transfer between the immobilized CcO was observed only under photoreductive conditions. At potentials below -0.4 V, heme *a*₃ can be reduced even in the presence of oxygen. However, SERR spectral changes induced by strong photoreduction, mainly the disappearance of the formyl stretching mode, point to an associated chemical modification of the hemes. Similar spectral changes were observed under non-photoreductive conditions at very negative potentials (below -0.7 V). In this case, the tetrapyrrole macrocycles may be attacked by reactive oxygen species that are intermediary formed after direct electrochemical reduction of molecular oxygen, which is presumably present in traces even under anaerobic conditions. Also photoreduction may be associated with the formation of reactive intermediates that are capable to attack the porphyrins.

Photoreduction of immobilized CcO, which severely distorted the initial investigations, could be effectively avoided with the new experimental setup. Using low laser powers, short accumulation times and a rotating electrode, a fully oxidized SERR spectrum of the enzyme could be obtained at open circuit.

A notable reduction of the immobilized CcO requires electrode potentials fairly negative with respect to the redox potentials of the cofactors. However, the true potential at the cofactor sites of the immobilized enzyme is likely to be substantially different from that poised at the working electrode due to the relatively large separation of the redox sites from the electrode and particularly due to the solution phase between the NTA SAM and the tethered protein.⁶⁴

The maximum extent of reduction achieved amounts to 40% of heme groups in terms of relative intensities. Examination of potential-dependent SERR spectra provides a strong evidence that only heme *a* is reduced upon lowering the potential. Hence, relative intensities of the ν_4 band can be converted to relative concentrations of the hemes resulting in a maximum reduction extent of 55% which is in a good agreement with the exclusive reduction of one heme group.

At electrode potentials between -0.2 and -0.65 V, heterogeneous electron transfer from the electrode to heme *a* occurs with a rate constant of 0.002 s⁻¹ under anaerobic conditions as well as in the presence of cyanide. Moreover, the rate constant of reduction is within the experimental error identical irrespective of the orientations of tethered CcO. This implies that immobilization of the enzyme with the natural electron entry domain close to

the electrode (CcO-II) does not facilitate the heterogeneous electron transfer. Consequently, it can be concluded that the primary electron acceptor, the Cu_A homonuclear site, which is not detectable by SERR spectroscopy, is not required for the reduction of the heme cofactors in the immobilized CcO. Electron transfer occurs thus via an alternative pathway through the protein.

Heme *a* and heme *a*₃ are located in the center of the transmembrane helices with similar distances to both sides of the membrane. The through space distances from the electrode to the heme groups are therefore identical for both orientations of the enzyme (CcO-I and CcO-II), namely ca. 50 Å. For such a large distance, electron tunneling cannot account for the experimentally determined rate constants for the reduction of heme *a*.¹ Assuming the exponential decay of the rate constant with the distance (see eq (9.1)), electron tunneling would correspond to an electron transfer rate lower than 10⁻¹⁰ s⁻¹.

Instead, electron hopping is proposed as the electron transfer mechanism since it can effectively compete with the superexchange mechanism at electron transfer distances longer than 30 Å.²²² Electron hopping through helical peptides self-assembled on Au electrodes was demonstrated and rate constants of ca. 1 s⁻¹ were determined for an electron transfer distance of more than 40 Å which is 3 orders of magnitude faster than electron tunneling.²²³ Furthermore, no distinct dependence of the electron transfer rate on the driving force was observed which also favors an electron hopping mechanism according to theoretical predictions,²²⁴ and experimental results for immobilized peptides.²²³ Amide groups of the peptide chain were suggested as the most plausible hopping sites,²²³ a conclusion which may be valid also for the immobilized CcO, supported by the presence of one amide group in the SAM.

11.6.2 Selective reduction of heme *a*

Although the electron transfer distances to heme *a* and heme *a*₃ are nearly the same, only heme *a* is electrochemically reduced in the immobilized CcO. This is a rather surprising result as the intramolecular electron transfer from heme *a* to heme *a*₃ occurs in the nanosecond time range in the solubilized enzyme.²²⁵

In the fully oxidized state of the most thoroughly studied CcO from beef heart and *Paracoccus denitrificans*, the midpoint redox potential of heme *a* is higher than that of heme *a*₃, the concrete values found in the literature are however considerably scattered.⁴¹ The most recurrent values appear to be 0.16 V for the reduction of heme *a* and 0.08 V for the reduction of heme *a*₃

at pH 7.3.^{213,226} If one of the hemes is reduced, the redox potential of the other is lowered because of the interaction between the cofactors, which was termed negative cooperativity. Consequently, the redox titration curve of each heme is split into two components: a high- and a low-potential transition. To interpret the data, the so called "neoclassical model"²²⁷ is used which describes a system of two redox centers with a redox interaction between them. Recently, identical midpoint redox potentials were determined for heme *a* and *a*₃, namely 0.17 and 0.02 V for the high- and low-potential transition respectively.²²⁸

As we do not observe any reduction of heme *a*₃ under non-photoreductive conditions, we conclude that the anticooperativity between the heme *a* and *a*₃ redox sites is efficiently blocked in the immobilized enzyme. A partial reduction of heme *a*₃ cannot be excluded because a trace amount of oxygen is presumably present in the cell also under anaerobic conditions. Oxygen would immediately bind to the reduced heme *a*₃ and reoxidize it. However, as oxygen does not inhibit the heme *a*₃ reduction under strongly photoreductive conditions, it can be concluded, that the electron transfer from heme *a* to heme *a*₃ in the immobilized CcO is very slow, even slower than the heterogeneous electron transfer from the electrode to heme *a*. Moreover, the CN inhibited CcO shows a very similar behavior as the immobilized enzyme under anaerobic conditions, namely the same rate constant for reduction and the same reduction extent. This finding implies that eventual traces of oxygen are not responsible for the slow electron transfer to heme *a*.

The immobilized enzyme appears to lack an essential feature, the redox interaction between the cofactors, which under physiological conditions guarantees the energy transduction in CcO. However, SERR spectroscopy, which probes the structure of the heme *a* and *a*₃ sites, does not reveal any structural changes that would account for the perturbation of the electron flow between the hemes. Specifically, we note that the native hydrogen bond interactions of the formyl substituents of both heme groups with the protein environment seem to be preserved as indicated by the characteristic vibrational frequencies. There is also no change of the ligation state to a 5cHS configuration form which frequently occurs in heme proteins immobilized on electrodes.^{10,11} In particular, the bridging ligand of the binuclear center in oxidases is only weakly bound so that in some cases a partial transition to the 5cHS form has been observed even in solution.⁴⁹ None of these structural changes has been detected for immobilized CcO, the loss of anticooperativity cannot be therefore related to a distortion of the heme sites structures.

Unlike in solution, electron and proton translocation in the immobilized CcO occurs in an electric field which may affect the mechanism and dynamics of charge translocation as well as protonation equilibria in proteins.^{10,11} Only

subtle pK_A changes of those protonable sites that are involved in the redox-linked proton translocation may substantially alter the network of cooperativities which ensures the functioning of the enzyme.^{229,230,231} In this respect, it is tempting to relate the present findings to the data obtained for CcO incorporated in phospholipid vesicles in a unidirectional manner,^{232,233,234} since local electric field strengths at electrodes and phospholipid bilayers may be comparable.³ It has been shown, that by increasing the transmembrane potentials the enzyme turnover can be efficiently blocked due to a drastic slowdown of proton and/or electron transfer, which in view of the present data may be understood in terms of electric field induced pK_A changes.

Influence of the electric field on the CcO cooperativity network was indirectly confirmed by SERR investigations of the aa_3 quinol oxidase from *Acidianus ambivalens*.¹⁸¹ In contrast to CcO, the primary electron acceptor is believed to be a loosely bound benzothiophene quinone, which is lost during purification.²³⁵ Moreover, a reversed order of the apparent reduction potentials of the two hemes is observed, the reduction potential of heme a is lower than that of heme a_3 ²³⁵ suggesting that redox interactions are not required in order to observe a fast intraprotein electron transfer. In the SERR experiment, the detergent solubilized quinol oxidase was adsorbed directly on bare Ag surface and a reversible electrochemical behavior was observed for both hemes.¹⁸¹ The apparent redox potentials were determined to be +0.12 and +0.19 V for heme a and a_3 respectively. Furthermore, the hemes display an ideal Nernstian behavior pointing to rather weak Coulombic interactions between the redox centers in the quinol oxidase.

11.7 Summary

The present results have shown that membrane bound CcO can be immobilized on a specifically functionalized Ag electrode under preservation of the native active site structure in the potential range between +0.1 and -0.65 V. The His-tagged enzyme was specifically attached to the surface via interaction with Ni-NTA or Zn-NTA and a quasi-natural lipid bilayer environment was formed subsequently.

The rate constant for the heterogeneous electron transfer to heme a was determined to be 0.002 s^{-1} independent of the enzyme orientation and applied driving force. Taking into account that the through space distance from the electrode to heme a site exceeds 50 Å, these findings suggest a multi-step electron tunneling or an electron hopping mechanism in which the Cu_A center is not involved. Electrochemical reduction is restricted to heme a implying that the complex network of cooperativities that links in-

tramolecular electron transfer and proton translocation in the native enzyme is severely perturbed upon immobilization, presumably due to the influence of the interfacial electric field.

Part V

Conclusions and Outlook

Conclusion

SERR spectroelectrochemistry has been employed in the present work to probe structural and dynamical properties of immobilized soluble and membrane-bound redox proteins. Investigations focused on two heme proteins that transfer electrons in aerobic respiration - cytochrome *c* and cytochrome *c* oxidase. By exciting the samples in the Soret absorption band advantage was taken from the resonance enhancement of the Raman spectra thanks to the π - π^* electronic transition of the heme group. Electrochemically roughened Ag electrodes were used throughout since they provide a very good surface enhancement at the excitation wavelength with respect to other metals like Au. The electrodes were modified with different coatings containing specific functional groups. Three different systems have been investigated.

First part of this thesis is dedicated to elucidate the mechanism of heterogeneous electron transfer of Cyt *c* at short distances from the electrode. Cyt *c* was attached to Ag electrodes via direct coordination of the heme iron to a pyridine terminal group of the modified electrode thereby lowering the rotational freedom of the immobilized protein. Electron transfer dynamics was followed by time-resolved SERR spectroelectrochemistry. The electron transfer rate constant was found to sensitively respond to the applied overpotential unambiguously discarding a gating mechanism as the rate-limiting step at short distances from the electrode. Analysis of the data in terms of a solvent friction model allowed for the determination of the reorganization energy. SERR results in our group were complemented by cyclic voltammetry measurements in Pittsburgh yielding a uniform picture of the electron transfer mechanism. All results converge to a reorganization energy value of 0.5 eV and indicate a change of mechanism from a tunneling controlled reaction at long distances to a solvent/protein friction controlled reaction at smaller distances from the electrode.

The second part focuses on a possible application of Cyt *c* in biosensing. The layer-by-layer technique was employed to form PASA-Cyt *c* multilayers on the top of a layer of Cyt *c* electrostatically adsorbed to a mixed carboxyl/hydroxyl-terminated biocompatible film. The multilayer assemblies

were investigated by SERR spectroelectrochemistry and cyclic voltammetry leading to the conclusion that the multilayers were unstable on rough Ag electrodes. Cyt *c* in the resulting one PASA-Cyt *c* adlayer system was shown to retain its native structure and to exhibit a nearly ideal Nernst behavior; moreover, the native-like properties of the immobilized protein are not perturbed after thermal treatment. PASA gives rise to a relatively pronounced SER spectral pattern which indicates reversible potential-dependent changes of the polyelectrolyte. Hence the redox process of Cyt *c* is coupled to a reversible oxidation-reduction of PASA as revealed by the comparative SERR analysis of layer systems including Cyt *c* and the redox-inactive apocytochrome *c*. Investigations of the electron transfer dynamics in these two systems points to an efficient electron exchange between PASA and Cyt *c*. The tight coupling of redox equilibria and dynamics in the PASA-Cyt *c* layer system indicates that PASA plays a crucial role in the electronic communication of Cyt *c* in multilayer systems.

Finally, a novel immobilization approach based on the affinity of a histidine-tag to the nickel nitrilo-triacetic acid has been employed for the membrane-bound enzyme CcO. The solubilized recombinant protein was attached to a functionalized Ag electrode and subsequently reconstituted into the lipid environment by detergent substitution. Depending on the His-tag position (C-terminus of subunit I or II) two different types of monolayers of uniformly oriented protein embedded in a phospholipid bilayer have been obtained. Despite the relatively large distance of the heme cofactors from the electrode surface, SERR spectra of decent quality could be obtained supporting thereby the rather long range effect of the surface enhancement. Minimizing the easily occurring photoreduction required a substantial improvement of the experimental setup. SERR spectra of heme *a* and heme *a*₃ cofactors displayed a native-like structure in both enzyme orientations. Rate constant for reduction of heme *a* was determined to be 0.002 s⁻¹ independent of protein orientation and overpotential pointing to a multi-step electron tunneling or hopping mechanism of heterogeneous electron transfer. Moreover the impediment of intramolecular electron transfer to heme *a*₃ provides a strong evidence for a perturbation of the native cooperativity of electron transfer and proton translocation, presumably induced by the interfacial electric field experienced by the immobilized enzyme.

Electric field effects are also likely to be responsible for the higher amount of five-coordinated species and slower relaxation dynamics when Cyt *c* is attached to pyridine-coated Ag electrodes as compared to Au electrodes. Larger electric field strengths on Ag electrodes could account for the generally observed lower rate constants of Cyt *c* adsorbed to short-spacer-coated Ag electrodes with respect to Au electrodes. The encountered instability of

polyelectrolyte-Cyt *c* multilayers might be at least partially ascribed to the different electric fields on Ag and Au electrodes. These observations point to the crucial importance of electric field effects in investigations of potential-dependent processes of immobilized proteins.

The present work confirms the general applicability of SERR spectroelectrochemistry to gain insight into the reaction mechanism and dynamics of immobilized redox proteins. Furthermore, an excellent agreement was achieved between SERR spectroelectrochemistry and cyclic voltammetry in the determination of redox potentials and standard rate constants.

Outlook

Proteins adsorbed to electrodes represent an important model system for investigations of heterogeneous electron transfer. Upon proper choice of electrode coating, electrochemical interfaces can mimic naturally occurring membrane/solution interfaces. However, the potential-dependent processes of immobilized redox proteins include not only heterogeneous electron transfer reactions but also non-faradaic processes taking place at the interface. At this point, vibrational spectroelectrochemistry can substantially contribute to the understanding as it provides a detailed information about the structure of the redox site. SERR spectroelectrochemical measurements may be complemented by surface-enhanced infrared absorption (SEIRA) spectroelectrochemical investigations that can bring additional information about the protein environment.

A very promising SERR approach to study protein reorientation has been recently developed in our group. It consists in monitoring relative intensities of differently polarized heme modes upon excitation in the absorption Q-band. This method has provided a compelling evidence for distance-dependent reorientation of Cyt *c* electrostatically adsorbed to carboxyl-terminated modified electrodes.¹⁶³ Extending this novel approach to other systems is certainly of a great interest.

Immobilization of membrane-bound redox proteins on electrodes stills represents a challenge. The serious drawback of the method employed within this work lies in the too large distance of the immobilized CcO from the electrode. The excessive separation of the enzyme from the electrode does not allow for an efficient control of the electron transfer reaction. In this situation, experiments aiming to investigate interprotein electron transfer between CcO and Cyt *c* under controlled-potential conditions are practically impossible. An auspicious strategy seems to be the direct adsorption of Cyt *c* on electrodes via a cysteine residue.²³⁶ In yeast iso-1-cytochrome *c* a native cysteine residue is located at the protein surface opposite to the heme crevice what enables to immobilize Cyt *c* in an advantageous position for complexation with CcO. In this arrangement, Cyt *c* was shown to adsorb

in the native state and to display fast electron transfer kinetics what is a prerequisite to study interprotein electron transfer.²³⁶

It would be even more interesting to examine structural changes of CcO in a physiological-like environment upon controlling the transmembrane potential. This can be achieved by reconstituting the membrane enzyme in liposomes that are adsorbed to black lipid membranes^{237,238} and combining this electrophysiological technique with Raman detection. The presumably extremely weak Raman signals might be increased with the help of a method that has gained increasing attention of researchers in the last years - the tip-enhanced Raman spectroscopy (TERS).²³⁹

Bibliography

- [1] MOSER, C.C.; KESKE, J.M.; WARNCKE, K.; FARID, R.S.; and DUTTON, P.L. Nature of Biological Electron-Transfer. *Nature* **355**(6363), 796–802 (1992).
- [2] LOVE, J.C.; ESTROFF, L.A.; KRIEBEL, J.K.; NUZZO, R.G.; and WHITESIDES, G.M. Self-assembled monolayers of thiolates on metals as a form of nanotechnology. *Chemical Reviews* **105**(4), 1103–1169 (2005).
- [3] CLARKE, R.J. The dipole potential of phospholipid membranes and methods for its detection. *Adv. Coll. Int. Sci.* **89**, 263–281 (2001).
- [4] ARMSTRONG, F.A. Recent developments in dynamic electrochemical studies of adsorbed enzymes and their active sites. *Current Opinion in Chemical Biology* **9**(2), 110–117 (2005).
- [5] WILLNER, I. and KATZ, E. Integration of layered redox proteins and conductive supports for bioelectronic applications. *Angew. Chem. Int. Ed.* **39**(7), 1180–1218 (2000).
- [6] ZHANG, J.D.; CHI, Q.J.; ALBRECHT, T.; KUZNETSOV, A.M.; GRUBB, M.; HANSEN, A.G.; WACKERBARTH, H.; WELINDER, A.C.; and ULSTRUP, J. Electrochemistry and bioelectrochemistry towards the single-molecule level: Theoretical notions and systems. *Electrochim. Acta* **50**(15), 3143–3159 (2005).
- [7] HEERING, H.A.; MEIJER, S.; HOEBEN, F.J.M.; DEKKER, C.; and LEMAY, S. From protein-film to single-enzyme voltammetry: hydrogenase nano-electrochemistry. In *Eurobic8, Conference Book*, (2006).
- [8] HELLER, I.; KONG, J.; HEERING, H.A.; WILLIAMS, K.A.; LEMAY, S.G.; and DEKKER, C. Individual single-walled carbon nanotubes as nanoelectrodes for electrochemistry. *Nano Letters* **5**(1), 137–142 (2005).

- [9] MURGIDA, D. and HILDEBRANDT, P. *Surface-enhanced vibrational spectroelectrochemistry: Electric-field effects on redox and redox-coupled processes of heme proteins*. Springer-Verlag Berlin, Berlin, (2006).
- [10] MURGIDA, D.H. and HILDEBRANDT, P. Redox and redox-coupled processes of heme proteins and enzymes at electrochemical interfaces. *PCCP* **7**(22), 3773–3784 (2005).
- [11] MURGIDA, D.H. and HILDEBRANDT, P. Electron-transfer processes of cytochrome c at interfaces. New insights by surface-enhanced resonance Raman spectroscopy. *Acc. Chem. Res.* **37**(11), 854–861 (2004).
- [12] COTTON, T.M.; SCHULTZ, S.G.; and VAN DUYNE, R.P. Surface-Enhanced Resonance Raman-Scattering from Cytochrome-C and Myoglobin Adsorbed on A Silver Electrode. *J. Am. Chem. Soc.* **102**(27), 7960–7962 (1980).
- [13] SMEKAL, A. Zur Quantentheorie der Dispersion. *Die Naturwissenschaften* **43**, 873–875 (1923).
- [14] RAMAN, C.V. and KRISHNAN, K.S. A New Type of Secondary Radiation. *Nature* **121**, 501–502 (1928).
- [15] ALBRECHT, A.C. Theory of Raman Intensities. *J. Chem. Phys.* **34**(5), 1476–1484 (1961).
- [16] ALBRECHT, A.C. Forbidden Character in Allowed Electronic Transitions. *J. Chem. Phys.* **33**(1), 156–169 (1960).
- [17] TANG, J. and ALBRECHT, A.C. Studies in Raman Intensity Theory. *J. Chem. Phys.* **49**(3), 1144–& (1968).
- [18] FLEISCHMANN, M.; HENDRA, P.J.; and MCQUILLAN, A.J. Raman-Spectra of Pyridine Adsorbed at A Silver Electrode. *Chemical Physics Letters* **26**(2), 163–166 (1974).
- [19] ALBRECHT, M.G. and CREIGHTON, J.A. Anomalously Intense Raman-Spectra of Pyridine at A Silver Electrode. *J. Am. Chem. Soc.* **99**(15), 5215–5217 (1977).
- [20] JEANMAIRE, D.L. and VAN DUYNE, R.P. Surface Raman Spectroelectrochemistry .1. Heterocyclic, Aromatic, and Aliphatic-Amines Adsorbed on Anodized Silver Electrode. *Journal of Electroanalytical Chemistry* **84**(1), 1–20 (1977).

-
- [21] MOSKOVITS, M. Surface-enhanced Raman spectroscopy: a brief retrospective. *J. Raman Spectrosc.* **36**(6-7), 485–496 (2005).
- [22] CAMPION, A. and KAMBHAMPATI, P. Surface-enhanced Raman scattering. *Chemical Society Reviews* **27**(4), 241–250 (1998).
- [23] MOSKOVITS, M. Surface-Enhanced Spectroscopy. *Reviews of Modern Physics* **57**(3), 783–826 (1985).
- [24] DANIELS, J.K. and CHUMANOV, G. Nanoparticle-mirror sandwich substrates for surface-enhanced Raman scattering. *J. Phys. Chem. B* **109**(38), 17936–17942 (2005).
- [25] COTTON, T.M; KIM, J.-H.; and HOLT, R.E. *Advances in Biophysical Chemistry*, volume 2, chapter Surface-enhanced resonance Raman scattering (SERRS) spectroscopy: A probe of biomolecular structure and bonding at surfaces, pages 115–147. JAI Press, (1992).
- [26] GREEN, D.R. and REED, J.C. Mitochondria and apoptosis. *Science* **281**(5381), 1309–1312 (1998).
- [27] MAUK, A. GRANT and SCOTT, ROBERT A., editors. *Cytochrome C: A Multidisciplinary Approach*. University Science Books, (1996).
- [28] MOORE, GEOFFREY R. and PETTIGREW, GRAHAM W., editors. *Cytochromes C: Evolutionary, Structural and Physicochemical Aspects (Springer Series in Molecular Biology)*. Springer, (1991).
- [29] BUSHNELL, G.W.; LOUIE, G.V.; and BRAYER, G.D. High-Resolution 3-Dimensional Structure of Horse Heart Cytochrome-C. *J. Mol. Biol.* **214**(2), 585–595 (1990).
- [30] HUMPHREY, W.; DALKE, A.; and SCHULTEN, K. VMD – Visual Molecular Dynamics. *Journal of Molecular Graphics* **14**, 33–38 (1996).
- [31] TAKANO, T. and DICKERSON, R.E. Conformation Change of Cytochrome-C .2. Ferricytochrome-C Refinement at 1.8 Å and Comparison with the Ferrocycytochrome Structure. *J. Mol. Biol.* **153**(1), 95–115 (1981).
- [32] TAKANO, T. and DICKERSON, R.E. Conformation Change of Cytochrome-C .1. Ferrocycytochrome-C Structure Refined at 1.5 Å Resolution. *J. Mol. Biol.* **153**(1), 79–94 (1981).

- [33] BANCHI, L.; BERTINI, I.; ROSATO, A.; and VARANI, G. Mitochondrial cytochromes c: a comparative analysis. *Journal of Biological Inorganic Chemistry* **4**(6), 824–837 (1999).
- [34] DOPNER, S.; HILDEBRANDT, P.; ROSELL, F.I.; MAUK, A.G.; VON WALTER, M.; BUSE, G.; and SOULIMANE, T. The structural and functional role of lysine residues in the binding domain of cytochrome c in the electron transfer to cytochrome c oxidase. *European Journal of Biochemistry* **261**(2), 379–391 (1999).
- [35] KOPPENOL, W.H. and MARGOLIAS, E. The Asymmetric Distribution of Charges on the Surface of Horse Cytochrome-C - Functional Implications. *J. Biol. Chem.* **257**(8), 4426–4437 (1982).
- [36] GOLDKORN, T. and SCHEJTER, A. Electrostatic Effects on the Kinetics of Oxidation-Reduction Reactions of C-Type Cytochromes. *J. Biol. Chem.* **254**(24), 2562–2566 (1979).
- [37] MARGALIT, R. and SCHEJTER, A. Cytochrome-C - Thermodynamic Study of Relationships Among Oxidation State, Ion-Binding and Structural Parameters .1. Effects of Temperature, Ph and Electrostatic Media on Standard Redox Potential of Cytochrome-C. *European Journal of Biochemistry* **32**(3), 492–499 (1973).
- [38] FEDURCO, M. Redox reactions of heme-containing metalloproteins: dynamic effects of self-assembled monolayers on thermodynamics and kinetics of cytochrome c electron-transfer reactions. *Coordination Chemistry Reviews* **209**, 263–331 (2000).
- [39] FERGUSON-MILLER, S. and BABCOCK, G.T. Heme/copper terminal oxidases. *Chemical Reviews* **96**(7), 2889–2907 (1996).
- [40] MOODY, A.J. 'As prepared' forms of fully oxidised haem/Cu terminal oxidases. *Biochim. Biophys. Acta-Bioenerg.* **1276**(1), 6–20 (1996).
- [41] MALATESTA, F.; ANTONINI, G.; SARTI, P.; and BRUNORI, M. Structure and Function of A Molecular Machine - Cytochrome-C-Oxidase. *Biophysical Chemistry* **54**(1), 1–33 (1995).
- [42] MILLS, D.A. and HOSLER, J.P. Slow proton transfer through the pathways for pumped protons in cytochrome c oxidase induces suicide inactivation of the enzyme. *Biochemistry* **44**(12), 4656–4666 (2005).

- [43] MICHEL, H.; BEHR, J.; HARRENGA, A.; and KANNT, A. Cytochrome C oxidase: Structure and spectroscopy. *Annual Review of Biophysics and Biomolecular Structure* **27**, 329–356 (1998).
- [44] SVENSSON-EK, M.; ABRAMSON, J.; LARSSON, G.; TORNROTH, S.; BRZEZINSKI, P.; IWATA, S.; and BIOLOGY, DISCIPLINE: BIO-CHEMISTRY & MOLECULAR. The X-ray crystal structures of wild-type and EQ(I-286) mutant cytochrome c oxidases from *Rhodobacter sphaeroides*. *J. Mol. Biol.* **321**(2), 329–339 (2002).
- [45] TSUKIHARA, T.; AOYAMA, H.; YAMASHITA, E.; TOMIZAKI, T.; YAMAGUCHI, H.; SHINZAWA-ITO, K.; NAKASHIMA, R.; YAONO, R.; and YOSHIKAWA, S. The whole structure of the 13-subunit oxidized cytochrome c oxidase at 2.8 angstrom. *Science* **272**(5265), 1136–1144 (1996).
- [46] IWATA, S.; OSTERMEIER, C.; LUDWIG, B.; and MICHEL, H. Structure at 2.8-Angstrom Resolution of Cytochrome-C-Oxidase from *Paracoccus-Denitrificans*. *Nature* **376**(6542), 660–669 (1995).
- [47] HOSLER, J.P.; FETTER, J.; TECKLENBURG, M.M.J.; ESPE, M.; LERMA, C.; and FERGUSON-MILLER, S. Cytochrome-Aa3 of *Rhodobacter-Sphaeroides* As A Model for Mitochondrial Cytochrome-C-Oxidase - Purification, Kinetics, Proton Pumping, and Spectral-Analysis. *J. Biol. Chem.* **267**(34), 24264–24272 (1992).
- [48] ABE, M.; KITAGAWA, T.; and KYOGOKU, Y. Resonance Raman-Spectra of Octaethylporphyrinato-Ni(II) and Meso-Deuterated and N-15 Substituted Derivatives. 2. Normal Coordinate Analysis. *J. Chem. Phys.* **69**(10), 4526–4534 (1978).
- [49] GERSCHER, S.; HILDEBRANDT, P.; BUSE, G.; and SOULIMANE, T. The active site structure of ba(3) oxidase from *Thermus thermophilus* studied by resonance Raman spectroscopy. *Biospectroscopy* **5**(5), S53–S63 (1999).
- [50] HEIBEL, G.E.; HILDEBRANDT, P.; LUDWIG, B.; STEINRUCKE, P.; SOULIMANE, T.; and BUSE, G. Comparative Resonance Raman-Study of Cytochrome-C-Oxidase from Beef-Heart and *Paracoccus-Denitrificans*. *Biochemistry* **32**(40), 10866–10877 (1993).
- [51] LEE, H.M.; DAS, T.K.; ROUSSEAU, D.L.; MILLS, D.; FERGUSON-MILLER, S.; and GENNIS, R.B. Mutations in the putative H-channel in

- the cytochrome c oxidase from *Rhodobacter sphaeroides* show that this channel is not important for proton conduction but reveal modulation of the properties of heme a. *Biochemistry* **39**(11), 2989–2996 (2000).
- [52] ATKINS, P. and DE PAULA, J. *Physical Chemistry*. Oxford University Press, 8th edition, (2006).
- [53] SMULEVICH, G. and SPIRO, T.G. Surface Enhanced Raman-Spectroscopic Evidence That Adsorption on Silver Particles Can Denature Heme-Proteins. *J. Phys. Chem.* **89**(24), 5168–5173 (1985).
- [54] AZZARONI, O.; VELA, M.E.; ANDREASEN, G.; CARRO, P.; and SALVAREZZA, R.C. Electrodesorption potentials of self-assembled alkanethiolate monolayers on Ag(111) and Au(111). An electrochemical, scanning tunneling microscopy and density functional theory. *J. Phys. Chem. B* **106**(47), 12267–12273 (2002).
- [55] KAKIUCHI, T.; USUI, H.; HOBARA, D.; and YAMAMOTO, M. Voltammetric properties of the reductive desorption of alkanethiol self-assembled monolayers from a metal surface. *Langmuir* **18**(13), 5231–5238 (2002).
- [56] MURGIDA, D.H. and HILDEBRANDT, P. Active-site structure and dynamics of cytochrome c immobilized on self-assembled monolayers - A time-resolved surface enhanced resonance Raman spectroscopic study. *Angew. Chem. Int. Ed.* **40**(4), 728–731 (2001).
- [57] ALBRECHT, T. *Dynamik und Mechanismen der heterogenen Elektronentransferprozesse von synthetischen und natürlichen Hämproteinen*. PhD thesis, TU Berlin, (2003).
- [58] CHI, Q.J.; ZHANG, J.D.; ANDERSEN, J.E.T.; and ULSTRUP, J. Ordered assembly and controlled electron transfer of the blue copper protein azurin at gold (111) single-crystal substrates. *J. Phys. Chem. B* **105**(20), 4669–4679 (2001).
- [59] RIVAS, L.; MURGIDA, D.H.; and HILDEBRANDT, P. Conformational and redox equilibria and dynamics of cytochrome c immobilized on electrodes via hydrophobic interactions. *J. Phys. Chem. B* **106**(18), 4823–4830 (2002).
- [60] MURGIDA, D.H. and HILDEBRANDT, P. The heterogeneous electron transfer of cytochrome c adsorbed on Ag electrodes coated with omega-carboxyl alkanethiols. A surface enhanced resonance Raman spectroscopic study. *Journal of Molecular Structure* **565**, 97–100 (2001).

-
- [61] PARDO-YISSAR, V.; KATZ, E.; WILLNER, I.; KOTLYAR, A.B.; SANDERS, C.; and LILL, H. Biomaterial engineered electrodes for bioelectronics. *Faraday Discussions* (116), 119–134 (2000).
- [62] SMITH, C.P. and WHITE, H.S. Theory of the Interfacial Potential Distribution and Reversible Voltammetric Response of Electrodes Coated with Electroactive Molecular Films. *Analytical Chemistry* **64**(20), 2398–2405 (1992).
- [63] LECOMTE, S.; HILDEBRANDT, P.; and SOULIMANE, T. Dynamics of the heterogeneous electron-transfer reaction of cytochrome c(552) from *Thermus thermophilus*. A time-resolved surface-enhanced resonance Raman spectroscopic study. *J. Phys. Chem. B* **103**(45), 10053–10064 (1999).
- [64] MURGIDA, D.H. and HILDEBRANDT, P. Heterogeneous electron transfer of cytochrome c on coated silver electrodes. Electric field effects on structure and redox potential. *J. Phys. Chem. B* **105**(8), 1578–1586 (2001).
- [65] PARK, E.S. and BOXER, S.G. Origins of the sensitivity of molecular vibrations to electric fields: Carbonyl and nitrosyl stretches in model compounds and proteins. *J. Phys. Chem. B* **106**(22), 5800–5806 (2002).
- [66] CAO, P.; YAO, J.L.; REN, B.; GU, R.; and TIAN, Z.Q. Potential dependence of the orientation of thiocyanate adsorbed on an iron electrode as probed by surface-enhanced Raman Spectroscopy. *J. Phys. Chem. B* **106**(29), 7283–7285 (2002).
- [67] OKLEJAS, V.; SJOSTROM, C.; HARRIS, J.M.; and DISCIPLINE: CHEMISTRY, PHYSICAL. Surface-enhanced Raman scattering based vibrational stark effect as a spatial probe of interfacial electric fields in the diffuse double layer. *J. Phys. Chem. B* **107**(31), 7788–7794 (2003).
- [68] OKLEJAS, V. and HARRIS, J.M. In-situ investigation of binary-component self-assembled monolayers: A SERS-based spectroelectrochemical study of the effects of monolayer composition on interfacial structure. *Langmuir* **19**(14), 5794–5801 (2003).
- [69] LORENZ, LISA. Schwingungsspektroskopische Untersuchung von selbstorganisierten Monoschichten aus bifunktionellen Thiolen. Master's thesis, TU Berlin, (2004).

-
- [70] MARCUS, R.A. Theory of Oxidation-Reduction Reactions Involving Electron Transfer .1. *J. Chem. Phys.* **24**(5), 966–978 (1956).
- [71] MARCUS, R.A. and SUTIN, N. Electron Transfers in Chemistry and Biology. *Biochim. Biophys. Acta* **811**(3), 265–322 (1985).
- [72] BOLTON, J.R.; MATAGA, N.; and MCLENDON, G. Introduction to Electron-Transfer in Inorganic, Organic, and Biological-Systems. *Advances in Chemistry Series* (228), 1–6 (1991).
- [73] MARCUS, R.A. Electron transfer reactions in chemistry - Theory and experiment. *Journal of Electroanalytical Chemistry* **438**(1-2), 251–259 (1997).
- [74] MILLER, J.R.; BEITZ, J.V.; and HUDDLESTON, R.K. Effect of Free-Energy on Rates of Electron-Transfer Between Molecules. *J. Am. Chem. Soc.* **106**(18), 5057–5068 (1984).
- [75] CLOSS, G.L.; CALCATERRA, L.T.; GREEN, N.J.; PENFIELD, K.W.; and MILLER, J.R. Distance, Stereoelectronic Effects, and the Marcus Inverted Region in Intramolecular Electron-Transfer in Organic Radical-Anions. *J. Phys. Chem.* **90**(16), 3673–3683 (1986).
- [76] JORTNER, J. Temperature-Dependent Activation-Energy for Electron-Transfer Between Biological Molecules. *J. Chem. Phys.* **64**(12), 4860–4867 (1976).
- [77] KESTNER, N.R.; LOGAN, J.; and JORTNER, J. Thermal Electron-Transfer Reactions in Polar-Solvents. *J. Phys. Chem.* **78**(21), 2148–2166 (1974).
- [78] ULSTRUP, J. and JORTNER, J. Effect of Intramolecular Quantum Modes on Free-Energy Relationships for Electron-Transfer Reactions. *J. Chem. Phys.* **63**(10), 4358–4368 (1975).
- [79] LEVICH, V.G. and DOGONADZE, R.R. Theory of Non-Radiation Electron Transitions from Ion to Ion in Solutions. *Doklady Akademii Nauk Sssr* **124**(1), 123–126 (1959).
- [80] MARCUS, R.A. On Theory of Electron-Transfer Reactions .6. Unified Treatment for Homogeneous and Electrode Reactions. *J. Chem. Phys.* **43**(2), 679–& (1965).
- [81] GOSAVI, S. and MARCUS, R.A. Nonadiabatic electron-transfer at metal surfaces. *J. Phys. Chem. B* **104**(9), 2067–2072 (2000).

- [82] CHIDSEY, C.E.D. Free-Energy and Temperature-Dependence of Electron-Transfer at the Metal-Electrolyte Interface. *Science* **251**(4996), 919–922 (1991).
- [83] NAHIR, T.M. and BOWDEN, E.F. The distribution of standard rate constants for electron transfer between thiol-modified gold electrodes and adsorbed cytochrome c. *Journal of Electroanalytical Chemistry* **410**(1), 9–13 (1996).
- [84] NAHIR, T.M.; CLARK, R.A.; and BOWDEN, E.F. Linear-Sweep Voltammetry of Irreversible Electron-Transfer in Surface-Confined Species Using the Marcus Theory. *Analytical Chemistry* **66**(15), 2595–2598 (1994).
- [85] ZUSMAN, L.D. Outer-Sphere Electron-Transfer in Polar-Solvents. *Chemical Physics* **49**(2), 295–304 (1980).
- [86] ZUSMAN, L.D. Dynamical Solvent Effects in Electron-Transfer Reactions. *Zeitschrift für Physikalische Chemie-International Journal of Research in Physical Chemistry & Chemical Physics* **186**, 1–29 (1994).
- [87] ZUSMAN, L.D. Solvent Dynamic Effects of Polarization Diffusion in the Rate-Constant of Electron-Transfer. *Electrochim. Acta* **36**(3-4), 395–399 (1991).
- [88] GARG, A.; ONUCHIC, J.N.; and AMBEGAOKAR, V. Effect of Friction on Electron-Transfer in Biomolecules. *J. Chem. Phys.* **83**(9), 4491–4503 (1985).
- [89] ZUSMAN, L.D. Outer-Sphere Electron-Transfer Reactions at An Electrode. *Chemical Physics* **112**(1), 53–59 (1987).
- [90] WACKERBARTH, H.; KLAR, U.; GUNTHER, W.; and HILDEBRANDT, P. Novel time-resolved surface-enhanced (resonance) Raman spectroscopic technique for studying the dynamics of interfacial processes: Application to the electron transfer reaction of cytochrome c at a silver electrode. *Applied Spectroscopy* **53**(3), 283–291 (1999).
- [91] KHOSHTARIYA, D.E.; WEI, J.J.; LIU, H.Y.; YUE, H.J.; and WALDECK, D.H. Charge-transfer mechanism for cytochrome c adsorbed on nanometer thick films. Distinguishing frictional control from conformational gating. *J. Am. Chem. Soc.* **125**(25), 7704–7714 (2003).

- [92] BRAUTIGAN, D.L.; FERGUSON-MILLER, S.; and E., MARGOLIASH. Mitochondrial cytochrome c: preparation and activity of native and chemically modified cytochromes c. *Methods in Enzymology* **53**, 128–164 (1978).
- [93] STELLWAGEN, E.; RYSAVY, R.; and BABUL, G. Conformation of Horse Heart Apocytochrome-C. *J. Biol. Chem.* **247**(24), 8074–8077 (1972).
- [94] MITCHELL, D.M. and GENNIS, R.B. Rapid Purification of Wildtype and Mutant Cytochrome-C-Oxidase from Rhodobacter-Sphaeroides by Ni²⁺-NTA Affinity-Chromatography. *FEBS Lett.* **368**(1), 148–150 (1995).
- [95] HISER, C.; MILLS, D.A.; SCHALL, M.; and FERGUSON-MILLER, S. C-terminal truncation and histidine-tagging of cytochrome c oxidase subunit II reveals the native processing site, shows involvement of the C-terminus in cytochrome c binding, and improves the assay for proton pumping. *Biochemistry* **40**(6), 1606–1615 (2001).
- [96] GIESS, F.; FRIEDRICH, M.G.; HEBERLE, J.; NAUMANN, R.L.; and KNOLL, W. The protein-tethered lipid bilayer: A novel mimic of the biological membrane. *Biophys. J.* **87**(5), 3213–3220 (2004).
- [97] FRIEDRICH, M.G.; GIESS, F.; NAUMANN, R.; KNOLL, W.; ATAKA, K.; HEBERLE, J.; HRABAKOVA, J.; MURGIDA, D.H.; and HILDEBRANDT, P. Active site structure and redox processes of cytochrome c oxidase immobilised in a novel biomimetic lipid membrane on an electrode. *Chem. Commun.* (21), 2376–2377 (2004).
- [98] RIGAUD, J.L.; MOSSER, G.; LACAPERE, J.J.; OLOFSSON, A.; LEVY, D.; and RANCK, J.L. Bio-beads: An efficient strategy for two-dimensional crystallization of membrane proteins. *Journal of Structural Biology* **118**(3), 226–235 (1997).
- [99] RIGAUD, J.L.; LEVY, D.; MOSSER, G.; and LAMBERT, O. Detergent removal by non-polar polystyrene beads - Applications to membrane protein reconstitution and two-dimensional crystallization. *European Biophysics Journal with Biophysics Letters* **27**(4), 305–319 (1998).
- [100] SCHOENFISCH, M.H.; ROSS, A.M.; and PEMBERTON, J.E. Electrochemical cleaning of surface-confined carbon contamination in self-assembled monolayers on polycrystalline Ag and Au. *Langmuir* **16**(6), 2907–2914 (2000).

- [101] TAYLOR, C.E.; GARVEY, S.D.; and PEMBERTON, J.E. Carbon contamination at silver surfaces: Surface preparation procedures evaluated by Raman spectroscopy and X-ray photoelectron spectroscopy. *Analytical Chemistry* **68**(14), 2401–2408 (1996).
- [102] TAYLOR, C.E.; SCHOENFISCH, M.H.; and PEMBERTON, J.E. Sequestration of carbonaceous species within alkanethiol self-assembled monolayers on Ag by Raman spectroscopy. *Langmuir* **16**(6), 2902–2906 (2000).
- [103] MALINOWSKI, E. R. *Factor Analysis in Chemistry*. Wiley, 3rd edition, (2002).
- [104] GEORGIADIS, K.E.; JHON, N.I.; EINARSDOTTIR, O.; and BIOLOGY, DISCIPLINE: BIOCHEMISTRY & MOLECULAR. Time-Resolved Optical-Absorption Studies of Intramolecular Electron-Transfer in Cytochrome-C-Oxidase. *Biochemistry* **33**(31), 9245–9256 (1994).
- [105] HANZLIKOVÁ, J.; PROCHÁZKA, M.; STEPANEK, J.; BOK, J.; BAUMRUK, V.; and ANZENBACHER, P. Metalation of 5,10,15,20-tetrakis(1-methyl-4-pyridyl)porphyrin in silver colloids studied via time dependence of surface-enhanced resonance Raman spectra. *J. Raman Spectrosc.* **29**(7), 575–584 (1998).
- [106] ZIMANYI, L. Analysis of the bacteriorhodopsin photocycle by singular value decomposition with self-modeling: A critical evaluation using realistic simulated data. *J. Phys. Chem. B* **108**(13), 4199–4209 (2004).
- [107] UZUNBAJAKAVA, N.; LENFERINK, A.; KRAAN, Y.; VOLOKHINA, E.; VRENSSEN, G.; GREVE, J.; and OTTO, C. Nonresonant confocal Raman imaging of DNA and protein distribution in apoptotic cells. *Biophys. J.* **84**(6), 3968–3981 (2003).
- [108] VAN MANEN, H.J.; KRAAN, Y.M.; ROOS, D.; and OTTO, C. Intracellular chemical imaging of heme-containing enzymes involved in innate immunity using resonance Raman microscopy. *J. Phys. Chem. B* **108**(48), 18762–18771 (2004).
- [109] DOPNER, S.; HILDEBRANDT, P.; MAUK, A.G.; LENK, H.; and STEMPFLE, W. Analysis of vibrational spectra of multicomponent systems. Application to pH-dependent resonance Raman spectra of ferri-cytochrome c. *Spectrochimica Acta Part A-Molecular and Biomolecular Spectroscopy* **52**(5), 573–584 (1996).

- [110] SONG, S.; CLARK, R.A.; BOWDEN, E.F.; and TARLOV, M.J. Characterization of Cytochrome-C Alkanethiolate Structures Prepared by Self-Assembly on Gold. *J. Phys. Chem.* **97**(24), 6564–6572 (1993).
- [111] AVILA, A.; GREGORY, B.W.; NIKI, K.; and COTTON, T.M. An electrochemical approach to investigate gated electron transfer using a physiological model system: Cytochrome c immobilized on carboxylic acid-terminated alkanethiol self-assembled monolayers on gold electrodes. *J. Phys. Chem. B* **104**(12), 2759–2766 (2000).
- [112] MURGIDA, D.H. and HILDEBRANDT, P. Proton-coupled electron transfer of cytochrome c. *J. Am. Chem. Soc.* **123**(17), 4062–4068 (2001).
- [113] DEGROOT, M.T.; EVERS, T.H.; MERKX, M.; and KOPER, M.T.M. Electron Transfer and Ligand Binding to Cytochrome c' Immobilized on Self-Assembled Monolayers. *Langmuir* **23**(2), 729–736 (2007).
- [114] HILDEBRANDT, P. and MURGIDA, D.H. Electron transfer dynamics of cytochrome c bound to self-assembled monolayers on silver electrodes. *Bioelectrochemistry* **55**(1-2), 139–143 (2002).
- [115] FUJITA, K.; NAKAMURA, N.; OHNO, H.; LEIGH, B.S.; NIKI, K.; GRAY, H.B.; and RICHARDS, J.H. Mimicking protein-protein electron transfer: Voltammetry of *Pseudomonas aeruginosa* azurin and the *Thermus thermophilus* Cu-A domain at omega-derivatized self-assembled-monolayer gold electrodes. *J. Am. Chem. Soc.* **126**(43), 13954–13961 (2004).
- [116] KRANICH, A.; DE LA ROSA, M. A.; MURGIDA, D. H.; and HILDEBRANDT, P. Unpublished results.
- [117] WEI, J.J.; LIU, H.Y.; DICK, A.R.; YAMAMOTO, H.; HE, Y.F.; and WALDECK, D.H. Direct wiring of cytochrome c's heme unit to an electrode: Electrochemical studies. *J. Am. Chem. Soc.* **124**(32), 9591–9599 (2002).
- [118] YAMAMOTO, H.; LIU, H.Y.; and WALDECK, D.H. Immobilization of cytochrome c at Au electrodes by association of a pyridine terminated SAM and the heme of cytochrome. *Chem. Commun.* (11), 1032–1033 (2001).
- [119] WEI, J.J.; LIU, H.Y.; KHOSHTARIYA, D.E.; YAMAMOTO, H.; DICK, A.; and WALDECK, D.H. Electron-transfer dynamics of cytochrome

- C: A change in the reaction mechanism with distance. *Angew. Chem. Int. Ed.* **41**(24), 4700–4703 (2002).
- [120] WEI, J.J.; LIU, H.Y.; NIKI, K.; MARGOLIASH, E.; and WALDECK, D.H. Probing electron tunneling pathways: Electrochemical study of rat heart cytochrome c and its mutant on pyridine-terminated SAMs. *J. Phys. Chem. B* **108**(43), 16912–16917 (2004).
- [121] MURGIDA, D.H.; HILDEBRANDT, P.; WEI, J.; HE, Y.F.; LIU, H.Y.; and WALDECK, D.H. Surface-enhanced resonance Raman spectroscopic and electrochemical study of cytochrome c bound on electrodes through coordination with pyridinyl-terminated self-assembled monolayers. *J. Phys. Chem. B* **108**(7), 2261–2269 (2004).
- [122] DOLIDZE, T.D.; KHOSHTARIYA, D.E.; WALDECK, D.H.; MACYK, J.; and VANELDIK, R. Positive Activation Volume for a Cytochrome C Electrode Process: Evidence for a "Protein Friction" Mechanism from High-Pressure Studies. *J. Phys. Chem. B* **107**(29), 7172–7179 (2003).
- [123] JEUKEN, LARS J. C. Conformational reorganisation in interfacial protein electron transfer. *Biochim. Biophys. Acta-Bioenerg.* **1604**(2), 67–76 (2003).
- [124] MURGIDA, D.H. and HILDEBRANDT, P. Electrostatic-field dependent activation energies modulate electron transfer of cytochrome c. *J. Phys. Chem. B* **106**(49), 12814–12819 (2002).
- [125] NAPPER, A.M.; LIU, H.; and WALDECK, D.H. The Nature of Electronic Coupling between Ferrocene and Gold through Alkanethiolate Monolayers on Electrodes: The Importance of Chain Composition, Interchain Coupling, and Quantum Interference. *J. Phys. Chem. B* **105**(32), 7699–7707 (2001).
- [126] YUE, H.J.; KHOSHTARIYA, D.; WALDECK, D.H.; GROCHOL, J.; HILDEBRANDT, P.; and MURGIDA, D.H. On the electron transfer mechanism between cytochrome c and metal electrodes. Evidence for dynamic control at short distances. *J. Phys. Chem. B* **110**(40), 19906–19913 (2006).
- [127] BOUBOUR, E. and LENNOX, R.B. Potential-induced defects in n-alkanethiol self-assembled monolayers monitored by impedance spectroscopy. *J. Phys. Chem. B* **104**(38), 9004–9010 (2000).

- [128] OELLERICH, S. *Spektroskopische Charakterisierung von Konformationsübergängen des Cytochrom c*. PhD thesis, Max Planck Institut für Strahlenchemie, (2001).
- [129] MUEGGE, I.; QI, P.X.; WAND, A.J.; CHU, Z.T.; and WARSHEL, A. The reorganization energy of cytochrome c revisited. *J. Phys. Chem. B* **101**(5), 825–836 (1997).
- [130] BASU, G.; KITAO, A.; KUKI, A.; and GO, N. Protein electron transfer reorganization energy spectrum from normal mode analysis. 2. Application to Ru-modified cytochrome c. *J. Phys. Chem. B* **102**(11), 2085–2094 (1998).
- [131] LIU, Y.P. and NEWTON, M.D. Reorganization Energy for Electron-Transfer at Film-Modified Electrode Surfaces - A Dielectric Continuum Model. *J. Phys. Chem.* **98**(29), 7162–7169 (1994).
- [132] PHELPS, D.K.; KORNYSHEV, A.A.; and WEAVER, M.J. Nonlocal Electrostatic Effects on Electron-Transfer Activation-Energies - Some Consequences for and Comparisons with Electrochemical and Homogeneous-Phase Kinetics. *J. Phys. Chem.* **94**(4), 1454–1463 (1990).
- [133] ZUSMAN, L.D. The Theory of Electron-Transfer Reactions in Solvents with 2 Characteristic Relaxation-Times. *Chemical Physics* **119**(1), 51–61 (1988).
- [134] FROHLICH, H. *Theory of Dielectrics: Dielectric Constant and Dielectric Loss*. Oxford University Press, 2nd edition, (1987).
- [135] KHOSHTARIYA, D.E.; DOLIDZE, T.D.; SEIFERT, S.; SARAULI, D.; LEE, G.; and VAN ELDIK, R. Kinetic, thermodynamic, and mechanistic patterns for free (unbound) cytochrome c at Au/SAM junctions: Impact of electronic coupling, hydrostatic pressure, and stabilizing/denaturing additives. *Chemistry-A European Journal* **12**(27), 7041–7056 (2006).
- [136] LIDE, D.R. and FREDERIKSE, H.P.R. *CRC Handbook of Chemistry and Physics*. CRC Press, Boca Raton, FL, 75th edition, (1995).
- [137] KHOSHTARIYA, D.E.; DOLIDZE, T.D.; ZUSMAN, L.D.; and WALDECK, D.H. Observation of the turnover between the solvent friction (overdamped) and tunneling (nonadiabatic) charge-transfer mechanisms for a Au/Fe(CN)(6)(3-/4-) electrode process and evidence for

- a freezing out of the Marcus barrier. *Journal of Physical Chemistry A* **105**(10), 1818–1829 (2001).
- [138] WEAVER, M.J.; PHELPS, D.K.; NIELSON, R.M.; GOLOVIN, M.N.; and MCMANIS, G.E. Solvent Dynamic Effects in Electron-Transfer - Electrochemical Versus Self-Exchange Kinetics of Tris(Hexafluoroacetylacetonato)Ruthenium(III/II) and Comparison with Other Probe Reactants. *J. Phys. Chem.* **94**(7), 2949–2954 (1990).
- [139] BEECE, D.; EISENSTEIN, L.; FRAUENFELDER, H.; GOOD, D.; MARDEN, M.C.; REINISCH, L.; REYNOLDS, A.H.; SORENSEN, L.B.; and YUE, K.T. Solvent Viscosity and Protein Dynamics. *Biochemistry* **19**(23), 5147–5157 (1980).
- [140] NIKI, K. Interprotein electron transfer: An electrochemical approach. *Electrochemistry* **70**(2), 82–90 (2002).
- [141] PAPACONSTANTOPOULOS, D.A. *Handbook of Band Structure of Elemental Solids*. Plenum Press, New York, (1986).
- [142] FINKLEA, H.O.; YOON, K.; CHAMBERLAIN, E.; ALLEN, J.; and HADDOX, R. Effect of the metal on electron transfer across self-assembled monolayers. *J. Phys. Chem. B* **105**(15), 3088–3092 (2001).
- [143] VALETTE, G. and HAMELIN, A. Structure and Properties of Electrochemical Double Film on Interphase of Aqueous Sodium-Fluoride Solutions and Silver. *Journal of Electroanalytical Chemistry* **45**(2), 301–319 (1973).
- [144] VALINCIUS, G. Elastic electrocapillary properties of polycrystalline gold. *Langmuir* **14**(21), 6307–6319 (1998).
- [145] DE BIASE, PABLO M.; DOCTOROVICH, FABIO; MURGIDA, DANIEL H.; and ESTRIN, DARIO A. Electric field effects on the reactivity of heme model systems. *Chemical Physics Letters* **434**(1-3), 121–126 (2007).
- [146] OELLERICH, S.; WACKERBARTH, H.; and HILDEBRANDT, P. Spectroscopic characterization of nonnative conformational states of cytochrome c. *J. Phys. Chem. B* **106**(25), 6566–6580 (2002).
- [147] GE, B. and LISDAT, F. Superoxide sensor based on cytochrome c immobilized on mixed-thiol SAM with a new calibration method. *Analytica Chimica Acta* **454**(1), 53–64 (2002).

- [148] DECHER, G. Fuzzy nanoassemblies: Toward layered polymeric multicomposites. *Science* **277**(5330), 1232–1237 (1997).
- [149] LVOV, Y.M.; LU, Z.Q.; SCHENKMAN, J.B.; ZU, X.L.; and RUSLING, J.F. Direct electrochemistry of myoglobin and cytochrome p450(cam) in alternate layer-by-layer films with DNA and other polyions. *J. Am. Chem. Soc.* **120**(17), 4073–4080 (1998).
- [150] WANG, L.W. and HU, N.F. Direct electrochemistry of hemoglobin in layer-by-layer films with poly(vinyl sulfonate) grown on pyrolytic graphite electrodes. *Bioelectrochemistry* **53**(2), 205–212 (2001).
- [151] LI, Z. and HU, N.F. Assembly of electroactive layer-by-layer films of myoglobin and ionomer poly(ester sulfonic acid). *Journal of Colloid and Interface Science* **254**(2), 257–265 (2002).
- [152] BEISSENHIRTZ, M.K.; SCHELLER, F.W.; STOCKLEIN, W.F.M.; KURTH, D.G.; MOHWALD, H.; and LISDAT, F. Electroactive cytochrome c multilayers within a polyelectrolyte assembly. *Angew. Chem. Int. Ed.* **43**(33), 4357–4360 (2004).
- [153] BEISSENHIRTZ, M.K.; KAFKA, B.; SCHAFER, D.; WOLNY, M.; and LISDAT, F. Electrochemical quartz crystal microbalance studies on cytochrome c/polyelectrolyte multilayer assemblies on gold electrodes. *Electroanalysis* **17**(21), 1931–1937 (2005).
- [154] BEISSENHIRTZ, M.K.; SCHELLER, F.W.; and LISDAT, F. A superoxide sensor based on a multilayer cytochrome c electrode. *Analytical Chemistry* **76**(16), 4665–4671 (2004).
- [155] BARBERO, C.; MIRAS, M.C.; SCHNYDER, B.; HAAS, O.; and KOTZ, R. Sulfonated Polyaniline Films As Cation Insertion Electrodes for Battery Applications .1. Structural and Electrochemical Characterization. *Journal of Materials Chemistry* **4**(12), 1775–1783 (1994).
- [156] NIAURA, G.; MAZEIKIENE, R.; and MALINAUSKAS, A. Structural changes in conducting form of polyaniline upon ring sulfonation as deduced by near infrared resonance Raman spectroscopy. *Synthetic Metals* **145**(2-3), 105–112 (2004).
- [157] WEI, X.L.; WANG, Y.Z.; LONG, S.M.; BOBECZKO, C.; and EPSTEIN, A.J. Synthesis and physical properties of highly sulfonated polyaniline. *J. Am. Chem. Soc.* **118**(11), 2545–2555 (1996).

- [158] YUE, J.; WANG, Z.H.; CROMACK, K.R.; EPSTEIN, A.J.; and MACDIARMID, A.G. Effect of Sulfonic-Acid Group on Polyaniline Backbone. *J. Am. Chem. Soc.* **113**(7), 2665–2671 (1991).
- [159] WEIDINGER, I.M.; MURGIDA, D.H.; DONG, W.F.; MOHWALD, H.; and HILDEBRANDT, P. Redox processes of cytochrome c immobilized on solid supported polyelectrolyte multilayers. *J. Phys. Chem. B* **110**(1), 522–529 (2006).
- [160] LECOMTE, S. Unpublished results.
- [161] LIU, Z.; YANG, Z.-L.; CUI, L.; REN, B.; and TIAN, Z.-Q. Electrochemically Roughened Palladium Electrodes for Surface-Enhanced Raman Spectroscopy: Methodology, Mechanism, and Application. *J. Phys. Chem. C* **111**(4), 1770–1775 (2007).
- [162] CLARK, R.A. and BOWDEN, E.F. Voltammetric peak broadening for cytochrome c/alkanethiolate monolayer structures: Dispersion of formal potentials. *Langmuir* **13**(3), 559–565 (1997).
- [163] KRANICH, A.; HILDEBRANDT, P.; and MURGIDA, D.H. Unpublished results.
- [164] LAVIRON, E. General Expression of the Linear Potential Sweep Voltammogram in the Case of Diffusionless Electrochemical Systems. *Journal of Electroanalytical Chemistry* **101**(1), 19–28 (1979).
- [165] GRUGER, A.; NOVAK, A.; REGIS, A.; and COLOMBAN, P. Infrared and Raman-Study of Polyaniline .2. Influence of Ortho Substituents on Hydrogen-Bonding and Uv/Vis Near-Ir Electron Charge-Transfer. *Journal of Molecular Structure* **328**, 153–167 (1994).
- [166] BOYER, M.; QUILLARD, S.; LOUARN, G.; LEFRANT, S.; REBOURT, E.; and MONKMAN, A.P. Oxidized model compounds of polyaniline studied by resonance Raman spectroscopy. *Synthetic Metals* **84**(1-3), 787–788 (1997).
- [167] BOYER, M.I.; QUILLARD, S.; LOUARN, G.; FROYER, G.; and LEFRANT, S. Vibrational study of the FeCl₃-doped dimer of polyaniline; A good model compound of emeraldine salt. *J. Phys. Chem. B* **104**(38), 8952–8961 (2000).
- [168] BAIBARAC, M.; COCHET, M.; LAPKOWSKI, M.; MIHUT, L.; LEFRANT, S.; and BALTOG, I. SERS spectra of polyaniline thin films

- deposited on rough Ag, Au and Cu. Polymer film thickness and roughness parameter dependence of SERS spectra. *Synthetic Metals* **96**(1), 63–70 (1998).
- [169] SHREEPATHI, S. and HOLZE, R. Spectroelectrochemistry and preresonance Raman spectroscopy of polyaniline-dodecylbenzenesulfonic acid colloidal dispersions. *Langmuir* **22**(11), 5196–5204 (2006).
- [170] COHEN, J.S.; FISHER, W.R.; and SCHECHTE, A.N. Spectroscopic Studies on Conformation of Cytochrome-C and Apocytochrome C. *J. Biol. Chem.* **249**(4), 1113–1118 (1974).
- [171] HAMADA, D.; HOSHINO, M.; KATAOKA, M.; FINK, A.L.; and GOTO, Y. Intermediate Conformational States of Apocytochrome-C. *Biochemistry* **32**(39), 10351–10358 (1993).
- [172] HUANG, W.S.; HUMPHREY, B.D.; and MACDIARMID, A.G. Polyaniline, A Novel Conducting Polymer - Morphology and Chemistry of Its Oxidation and Reduction in Aqueous-Electrolytes. *Journal of the Chemical Society-Faraday Transactions I* **82**, 2385–& (1986).
- [173] MACDIARMID, A.G.; YANG, L.S.; HUANG, W.S.; and HUMPHREY, B.D. Polyaniline - Electrochemistry and Application to Rechargeable Batteries. *Synthetic Metals* **18**(1-3), 393–398 (1987).
- [174] KILMARTIN, P.A. and WRIGHT, G.A. Photoelectrochemical and spectroscopic studies of sulfonated polyanilines .1. Copolymers of orthanilic acid and aniline. *Synthetic Metals* **88**(2), 153–162 (1997).
- [175] LOUARN, G.; LAPKOWSKI, M.; QUILLARD, S.; PRON, A.; BUISSON, J.P.; and LEFRANT, S. Vibrational properties of polyaniline - Isotope effects. *J. Phys. Chem.* **100**(17), 6998–7006 (1996).
- [176] SARICIFTCI, N.S. and KUZMANY, H. Optical Spectroscopy and Resonance Raman-Scattering of Polyaniline During Electrochemical Oxidation and Reduction. *Synthetic Metals* **21**(2), 157–162 (1987).
- [177] FOLCH, S.; GRUGER, A.; REGIS, A.; and COLOMBAN, P. Optical and vibrational spectra of sols/solutions of polyaniline: Water as secondary dopant. *Synthetic Metals* **81**(2-3), 221–225 (1996).
- [178] HUGOTLEGOFF, A. and BERNARD, M.C. Protonation and Oxidation Processes in Polyaniline Thin-Films Studied by Optical Multichannel Analysis and In-Situ Raman-Spectroscopy. *Synthetic Metals* **60**(2), 115–131 (1993).

- [179] WILLNER, I. and WILLNER, B. Vectorial photoinduced electron-transfer in tailored redox-active proteins and supramolecular nanoparticle arrays. *Coordination Chemistry Reviews* **245**(1-2), 139–151 (2003).
- [180] VINCENT, K.A.; CRACKNELL, J.A.; PARKIN, A.; and ARMSTRONG, F.A. Hydrogen cycling by enzymes: electrocatalysis and implications for future energy technology. *Dalton Transactions* (21), 3397–3403 (2005).
- [181] TODOROVIC, S.; PEREIRA, M.M.; BANDEIRAS, T.M.; TEIXEIRA, M.; HILDEBRANDT, P.; and MURGIDA, D.H. Midpoint potentials of hemes a and a(3) in the quinol oxidase from *Acidianus ambivalens* are inverted. *J. Am. Chem. Soc.* **127**(39), 13561–13566 (2005).
- [182] SALAMON, Z.; HAZZARD, J.T.; and TOLLIN, G. Direct Measurement of Cyclic Current-Voltage Responses of Integral Membrane-Proteins at A Self-Assembled Lipid-Bilayer-Modified Electrode - Cytochrome-F and Cytochrome-C-Oxidase. *Proc. Natl. Acad. Sci. U. S. A.* **90**(14), 6420–6423 (1993).
- [183] SACKMANN, E. Supported membranes: Scientific and practical applications. *Science* **271**(5245), 43–48 (1996).
- [184] BURGESS, J.D.; RHOTEN, M.C.; and HAWKRIDGE, F.M. Cytochrome c oxidase immobilized in stable supported lipid bilayer membranes. *Langmuir* **14**(9), 2467–2475 (1998).
- [185] SU, L.Y.; HAWKRIDGE, F.M.; and RHOTEN, M.C. Electroreduction of oxygen by cytochrome c oxidase immobilized in electrode-supported lipid bilayer membranes. *Chemistry & Biodiversity* **1**(9), 1281–1288 (2004).
- [186] NAUMANN, R.; SCHMIDT, E.K.; JONCZYK, A.; FENDLER, K.; KADENBACH, B.; LIEBERMANN, T.; OFFENHAUSSER, A.; and KNOLL, W. The peptide-tethered lipid membrane as a biomimetic system to incorporate cytochrome c oxidase in a functionally active form. *Biosens. Bioelectron.* **14**(7), 651–662 (1999).
- [187] JEUKEN, L.J.C.; CONNELL, S.D.; HENDERSON, P.J.F.; GENNIS, R.B.; EVANS, S.D.; and BUSHBY, R.J. Redox enzymes in tethered membranes. *J. Am. Chem. Soc.* **128**(5), 1711–1716 (2006).

- [188] HAAS, A.S.; PILLOUD, D.L.; REDDY, K.S.; BABCOCK, G.T.; MOSER, C.C.; BLASIE, J.K.; and DUTTON, P.L. Cytochrome c and cytochrome c oxidase: Monolayer assemblies and catalysis. *J. Phys. Chem. B* **105**(45), 11351–11362 (2001).
- [189] SCHMITT, J.; HESS, H.; and STUNNENBERG, H.G. Affinity Purification of Histidine-Tagged Proteins. *Molecular Biology Reports* **18**(3), 223–230 (1993).
- [190] NIEBA, L.; NIEBAAXMANN, S.E.; PERSSON, A.; HAMALAINEN, M.; EDEBRATT, F.; HANSSON, A.; LIDHOLM, J.; MAGNUSSON, K.; KARLSSON, A.F.; and PLUCKTHUN, A. BIACORE analysis of histidine-tagged proteins using a chelating NTA sensor chip. *Analytical Biochemistry* **252**(2), 217–228 (1997).
- [191] RIGLER, P.; ULRICH, W.P.; HOFFMANN, P.; MAYER, M.; and VOGEL, H. Reversible immobilization of peptides: Surface modification and in situ detection by attenuated total reflection FTIR Spectroscopy. *ChemPhysChem* **4**(3), 268–275 (2003).
- [192] MURATA, M.; YANO, K.; KUROKI, S.; SUZUTANI, T.; and KATAYAMA, Y. Protein-immobilized electrode for rapid and convenient sensing of thyroid hormone receptor-ligand interaction. *Analytical Sciences* **19**(12), 1569–1573 (2003).
- [193] CHEN, H.M.; WANG, W.C.; and CHEN, S.H. A metal-chelating piezoelectric sensor chip for direct detection and oriented immobilization of polyHis-tagged proteins. *Biotechnology Progress* **20**(4), 1237–1244 (2004).
- [194] DAS, R.; KILEY, P.J.; SEGAL, M.; NORVILLE, J.; YU, A.A.; WANG, L.Y.; TRAMMELL, S.A.; REDDICK, L.E.; KUMAR, R.; STELLACCI, F.; LEBEDEV, N.; SCHNUR, J.; BRUCE, B.D.; ZHANG, S.G.; and BALDO, M. Integration of photosynthetic protein molecular complexes in solid-state electronic devices. *Nano Letters* **4**(6), 1079–1083 (2004).
- [195] MALY, J.; DI MEO, C.; DE FRANCESCO, M.; MASCI, A.; MASOJIDEK, J.; SUGIURA, M.; VOLPE, A.; and PILLOTON, R. Reversible immobilization of engineered molecules by Ni-NTA chelators. *Bioelectrochemistry* **63**(1-2), 271–275 (2004).
- [196] TRAMMELL, S.A.; WANG, L.Y.; ZULLO, J.M.; SHASHIDHAR, R.; and LEBEDEV, N. Orientated binding of photosynthetic reaction centers

- on gold using Ni-NTA self-assembled monolayers. *Biosens. Bioelectron.* **19**(12), 1649–1655 (2004).
- [197] ATAKA, K.; GIESS, F.; KNOLL, W.; NAUMANN, R.; HABER-POHLMEIER, S.; RICHTER, B.; and HEBERLE, J. Oriented attachment and membrane reconstitution of his-tagged cytochrome c oxidase to a gold electrode: In situ monitoring by surface-enhanced infrared absorption spectroscopy. *J. Am. Chem. Soc.* **126**(49), 16199–16206 (2004).
- [198] HRABAKOVA, J.; ATAKA, K.; HEBERLE, J.; HILDEBRANDT, P.; and MURGIDA, D.H. Long distance electron transfer in cytochrome c oxidase immobilised on electrodes. A surface enhanced resonance Raman spectroscopic study. *PCCP* **8**(6), 759–766 (2006).
- [199] ATAKA, K.; RICHTER, B.; and HEBERLE, J. Orientational control of the physiological reaction of cytochrome c oxidase tethered to a gold electrode. *J. Phys. Chem. B* **110**(18), 9339–9347 (2006).
- [200] MAYER, D.; ATAKA, K.; HEBERLE, J.; and OFFENHAUSSER, A. Scanning probe microscopic studies of the oriented attachment and membrane reconstitution of cytochrome c oxidase to a gold electrode. *Langmuir* **21**(19), 8580–8583 (2005).
- [201] OSAWA, M. *Surface-enhanced infrared absorption*. Springer-Verlag Berlin, Berlin, (2001).
- [202] MIYAKE, H.; YE, S.; and OSAWA, M. Electroless deposition of gold thin films on silicon for surface-enhanced infrared spectroelectrochemistry. *Electrochemistry Communications* **4**(12), 973–977 (2002).
- [203] LILEY, M.; KELLER, T.A.; DUSCHL, C.; and VOGEL, H. Direct observation of self-assembled monolayers, ion complexation, and protein conformation at the gold/water interface: An FTIR spectroscopic approach. *Langmuir* **13**(16), 4190–4192 (1997).
- [204] GU, Y.G.; LI, P.S.; SAGE, J.T.; and CHAMPION, P.M. Photoreduction of Heme-Proteins - Spectroscopic Studies and Cross-Section Measurements. *J. Am. Chem. Soc.* **115**(12), 4993–5004 (1993).
- [205] ADAR, F. and ERECINSKA, M. Photoreductive Titration of the Resonance Raman-Spectra of Cytochrome-Oxidase in Whole Mitochondria. *Biochemistry* **18**(9), 1825–1829 (1979).

- [206] BABCOCK, G.T. and SALMEEN, I. Resonance Raman-Spectra and Optical-Properties of Oxidized Cytochrome-Oxidase. *Biochemistry* **18**(12), 2493–2498 (1979).
- [207] BOCIAN, D.F.; LEMLEY, A.T.; PETERSEN, N.O.; BRUDVIG, G.W.; and CHAN, S.I. Resonance Raman-Spectra of Cytochrome-C Oxidase - Excitation in the 600-Nm Region. *Biochemistry* **18**(20), 4396–4402 (1979).
- [208] OGURA, T.; YOSHIKAWA, S.; and KITAGAWA, T. Resonance Raman-Study on Photoreduction of Cytochrome-C-Oxidase - Distinction of Cytochrome-A and Cytochrome-A3 in the Intermediate Oxidation-States. *Biochemistry* **24**(26), 7746–7752 (1985).
- [209] BETTINGER, K.; PRUTSCH, A.; VOGTT, K.; and LUBBEN, M. Non-invasive auto-photoreduction used as a tool for studying structural changes in heme-copper oxidases by FTIR spectroscopy. *Biophys. J.* **86**(5), 3230–3240 (2004).
- [210] JOHNSON, D.L.; POLYAK, S.W.; WALLACE, J.C.; and MARTIN, L.L. Probing the stability of the disulfide radical intermediate of thioredoxin using direct electrochemistry. *Letters in Peptide Science* **10**(5-6), 495–500 (2003).
- [211] JOHNSON, D.L. and MARTIN, L.L. Controlling protein orientation at interfaces using histidine tags: An alternative to Ni/NTA. *J. Am. Chem. Soc.* **127**(7), 2018–2019 (2005).
- [212] OGURA, T.; SONE, N.; TAGAWA, K.; and KITAGAWA, T. Resonance Raman-Study of the Aa3-Type Cytochrome-Oxidase of Thermophilic Bacterium Ps3. *Biochemistry* **23**(12), 2826–2831 (1984).
- [213] HARMON, P.A.; HENDLER, R.W.; and LEVIN, I.W. Resonance Raman and Optical Spectroscopic Monitoring of Heme-A Redox States in Cytochrome-C-Oxidase During Potentiometric Titrations. *Biochemistry* **33**(3), 699–707 (1994).
- [214] HIROTA, S.; OGURA, T.; SHINZAWA-ITO, K.; YOSHIKAWA, S.; and KITAGAWA, T. Observation of multiple CN-isotope-sensitive Raman bands for CN- adducts of hemoglobin, myoglobin, and cytochrome c oxidase: Evidence for vibrational coupling between the Fe-C-N bending and porphyrin in-plane modes. *J. Phys. Chem.* **100**(37), 15274–15279 (1996).

- [215] CHING, Y.C.; ARGADE, P.V.; and ROUSSEAU, D.L. Resonance Raman-Spectra of CN-Bound Cytochrome-Oxidase - Spectral Isolation of Cytochrome-A2+, Cytochrome-A3(2+), and Cytochrome-A3(2+)(CN-). *Biochemistry* **24**(18), 4938–4946 (1985).
- [216] PINAKOULAKI, E.; VAMVOUKA, M.; and VAROTSIS, C. Resonance Raman detection of the Fe2+-C-N modes in heme-copper oxidases: A probe of the active site. *Inorg. Chem.* **43**(16), 4907–4910 (2004).
- [217] PINAKOULAKI, E.; VAMVOUKA, M.; and VAROTSIS, C. The active site structure of heme a(3)(3+)-C N-Cu-B(2+) of cytochrome aa(3) oxidase as revealed from resonance Raman scattering. *J. Phys. Chem. B* **107**(36), 9865–9868 (2003).
- [218] DAS, T.K.; GOMES, C.M.; BANDEIRAS, T.M.; PEREIRA, M.M.; TEIXEIRA, M.; and ROUSSEAU, D.L. Active site structure of the aa(3) quinol oxidase of *Acidianus ambivalens*. *Biochim. Biophys. Acta-Bioenerg.* **1655**(1-3), 306–320 (2004).
- [219] LYNCH, S.R.; CARTER, R.H.; and COPELAND, R.A. Resonance Raman-Spectroscopy of the Cytochrome-C-Oxidase from *Paracoccus Denitrificans*. *Biochemistry* **32**(27), 6923–6927 (1993).
- [220] YOSHIKAWA, S. and CAUGHEY, W.S. Infrared Evidence of Cyanide Binding to Iron and Copper Sites in Bovine Heart Cytochrome-C-Oxidase - Implications Regarding Oxygen Reduction. *J. Biol. Chem.* **265**(14), 7945–7958 (1990).
- [221] CAUGHEY, W.S.; DONG, A.; SAMPATH, V.; YOSHIKAWA, S.; and ZHAO, X.J. Probing Heart Cytochrome-C-Oxidase Structure and Function by Infrared-Spectroscopy. *J. Bioenerg. Biomembr.* **25**(2), 81–91 (1993).
- [222] DAVIS, W.B.; SVEC, W.A.; RATNER, M.A.; and WASIELEWSKI, M.R. Molecular-wire behaviour in p-phenylenevinylene oligomers. *Nature* **396**(6706), 60–63 (1998).
- [223] MORITA, T. and KIMURA, S. Long-range electron transfer over 4 nm governed by an inelastic hopping mechanism in self-assembled monolayers of helical peptides. *J. Am. Chem. Soc.* **125**(29), 8732–8733 (2003).
- [224] PETROV, E.G.; SHEVCHENKO, Y.V.; TESLENKO, V.I.; and MAY, V. Nonadiabatic donor-acceptor electron transfer mediated by a molecular bridge: A unified theoretical description of the superexchange and hopping mechanism. *J. Chem. Phys.* **115**(15), 7107–7122 (2001).

- [225] JASAITIS, A.; RAPPAPORT, F.; PILET, E.; LIEBL, U.; and VOS, M.H. Activationless electron transfer through the hydrophobic core of cytochrome c oxidase. *Proc. Natl. Acad. Sci. U. S. A.* **102**(31), 10882–10886 (2005).
- [226] BLAIR, D.F.; ELLIS, W.R.; WANG, H.; GRAY, H.B.; and CHAN, S.I. Spectroelectrochemical Study of Cytochrome-C-Oxidase - Ph and Temperature Dependences of the Cytochrome Potentials - Characterization of Site-Site Interactions. *J. Biol. Chem.* **261**(25), 1524–1537 (1986).
- [227] NICHOLLS, P. and PETERSEN, L.C. Haem-Haem Interactions in Cytochrome Alpha Alpha3 During Anaerobic-Aerobic Transition. *Biochim. Biophys. Acta* **357**(3), 462–467 (1974).
- [228] GORBIKOVA, E.A.; VUORILEHTO, K.; WIKSTROM, M.; and VERKHOVSKY, M.I. Redox titration of all electron carriers of cytochrome c oxidase by Fourier transform infrared spectroscopy. *Biochemistry* **45**(17), 5641–5649 (2006).
- [229] XAVIER, A.V. Thermodynamic and choreographic constraints for energy transduction by cytochrome c oxidase. *Biochim. Biophys. Acta-Bioenerg.* **1658**(1-2), 23–30 (2004).
- [230] XAVIER, A.V. A mechano-chemical model for energy transduction in cytochrome c oxidase: the work of a Maxwell's god. *FEBS Lett.* **532**(3), 261–266 (2002).
- [231] NEUMANN, E. Chemical Electric-Field Effects in Biological Macromolecules. *Prog. Biophys. Mol. Biol.* **47**(3), 197–231 (1986).
- [232] GREGORY, L. and FERGUSON-MILLER, S. Independent Control of Respiration in Cytochrome-C Oxidase Vesicles by Ph and Electrical Gradients. *Biochemistry* **28**(6), 2655–2662 (1989).
- [233] MORONEY, P.M.; SCHOLLES, T.A.; and HINKLE, P.C. Effect of Membrane-Potential and Ph Gradient on Electron-Transfer in Cytochrome-Oxidase. *Biochemistry* **23**(21), 4991–4997 (1984).
- [234] SARTI, P.; ANTONINI, G.; MALATESTA, F.; and BRUNORI, M. Respiratory Control in Cytochrome-Oxidase Vesicles Is Correlated with the Rate of Internal Electron-Transfer. *Biochem. J.* **284**, 123–127 (1992).

- [235] GIUFFRÉ, A.; GOMES, C.M.; ANTONINI, G.; DITRI, E.; TEIXEIRA, M.; and BRUNORI, M. Functional properties of the quinol oxidase from *Acidianus ambivalens* and the possible catalytic role of its electron donor - Studies on the membrane-integrated and purified enzyme. *European Journal of Biochemistry* **250**(2), 383–388 (1997).
- [236] HEERING, H.A.; WIERTZ, F.G.M.; DEKKER, C.; and DE VRIES, S. Direct immobilization of native yeast Iso-1 cytochrome c on bare gold: Fast electron relay to redox enzymes and zeptomole protein-film voltammetry. *J. Am. Chem. Soc.* **126**(35), 11103–11112 (2004).
- [237] RUITENBERG, M.; KANNT, A.; BAMBERG, E.; FENDLER, K.; and MICHEL, H. Reduction of cytochrome c oxidase by a second electron leads to proton translocation. *Nature* **417**(6884), 99–102 (2002).
- [238] RUITENBERG, M.; KANNT, A.; BAMBERG, E.; LUDWIG, B.; MICHEL, H.; and FENDLER, K. Single-electron reduction of the oxidized state is coupled to proton uptake via the K pathway in *Paracoccus denitrificans* cytochrome c oxidase. *Proc. Natl. Acad. Sci. U. S. A.* **97**(9), 4632–4636 (2000).
- [239] PETTINGER, B.; REN, B.; PICARDI, G.; SCHUSTER, R.; and ERTL, G. Nanoscale probing of adsorbed species by tip-enhanced Raman spectroscopy. *Phys. Rev. Lett.* **92**(9), 096101–1 (2004).

Aufstellung der wissenschaftlichen Veröffentlichungen

Teile der vorliegenden Arbeit sind bisher in folgenden Publikationen veröffentlicht:

M. G. Friedrich, F. Gieß, R. Naumann, W. Knoll, K. Ataka, J. Heberle, J. Hrabakova, D. H. Murgida, and P. Hildebrandt. Active site structure and redox processes of cytochrome *c* oxidase immobilised in a novel biomimetic lipid membrane on an electrode. *Chemical Communications* (**21**): 2376-2377 (2004)

J. Hrabakova, K. Ataka, J. Heberle, P. Hildebrandt and D. H. Murgida. Long distance electron transfer in cytochrome *c* oxidase immobilised on electrodes. A surface enhanced resonance Raman spectroscopic study. *Physical Chemistry Chemical Physics* (**8**): 759-766 (2006)

H. Yue, D. Khoshtariya, D. H. Waldeck, J. Grochol, P. Hildebrandt and D. H. Murgida. On the electron transfer mechanism between cytochrome *c* and metal electrodes at short distances. *Journal of Physical Chemistry B* **110** (**40**) 19906-19913 (2006)

Selbständigkeitserklärung

Hiermit versichere ich an Eides statt, die vorliegende Arbeit selbständig ohne fremde Hilfe verfasst zu haben und nur die angegebene Quellen und Hilfsmittel verwendet zu haben.

Jana Grochol

Berlin, den 6. März 2007

Acknowledgement

The work summarized in this thesis was carried out at the Max-Volmer-Laboratorium of the Technical University in Berlin between 2003 and 2007.

I would especially like to thank Prof. Dr. Peter Hildebrandt for giving me the opportunity to complete my PhD in one of the famous SERR scientific groups. I am grateful to Dr. Daniel H. Murgida for his careful guidance and inspiration in all stages of my research work.

Special thanks go to present and former members of the Hildebrandt group for interesting discussions. Particularly I wish to thank the "Mensa" section for daily edifying distraction. Thanks Anja for the nice time we had sharing the office and the lab. I am grateful to Hendrik and David for making the computers work perfectly.

Finally, I would like to acknowledge the financial support from DFG (SFB 498, project A8).

Michalovi děkuji za podporu a trpělivost.

Lebenslauf

Persönliches:

Name: Jana Grochol geboren Hrabáková
Geburtsdatum: 30.05.1979
Geburtsort: Hořovice, Tschechische Republik
Nationalität: tschechisch
Familienstand: verheiratet

Ausbildung:

1990 - 1995	Gymnázium Hořovice, Tschechische Republik
1995 - 1998	Lycée Alphonse Daudet, Nimes, Frankreich
1998 - 2003	Studium der Physik an der Karlsuniversität in Prag
2002 - 2003	Diplomarbeit zum Thema: <i>Investigation of heavy metal ion interaction with important biomolecules</i> unter Betreuung von Prof. Dr. J. Štěpánek
2003 - 2007	Promotion an der Technischen Universität Berlin Dissertation zum Thema: <i>Raman spectroelectrochemical investigations of immobilized redox proteins</i> unter Betreuung von Prof. Dr. P. Hildebrandt